RICE UNIVERSITY

Probing nonlocal correlations with ultralong-range Rydberg molecules

By

Joseph D. Whalen

A THESIS SUBMITTED
IN PARTIAL FULFILLMENT OF THE
REQUIREMENTS FOR THE DEGREE

Doctor of Philosophy

APPROVED, THESIS COMMITTEE

Thomas Killian

Thomas Killian
Dean of the Weiss School of Natural Sciences
Professor of Physics and Astronomy

Barry Dunning

F. Barry Dunning
Sam and Helen Worden Professor of Physics
and Astronomy

Hanyu Zhu

Hanyu Zhu
Assistant Professor, Materials Science and
NanoEngineering, William Marsh Rice Chair

HOUSTON, TEXAS

June 2021

RICE UNIVERSITY

Probing nonlocal correlations with ultralong-range Rydberg molecules

by

Joseph D. Whalen

A Thesis Submitted
in Partial Fulfillment of the
Requirements for the Degree

Doctor of Philosophy

Approved, Thesis Committee:

Thomas C. Killian, Chair
Dean of the Weiss School of Natural Sciences
Professor of Physics and Astronomy

F. Barry Dunning
Sam and Helen Worden Professor of Physics and Astronomy

Hanyu Zhu
Assistant Professor, Materials Sceince and NanoEngineering, William Marsh Rice Chair

Houston, Texas

June, 2021

ABSTRACT

Probing nonlocal correlations with ultralong-range Rydberg molecules

by

Joseph D. Whalen

Ultracold atomic systems provide pristine environments for creating and manipulating strongly-interacting quantum systems. The flexibility and utility of ultracold atomic systems comes at the cost of isolation of the quantum system away from environmental perturbations inside of an ultra-high vacuum chamber. This isolation reduces the number of ways that these systems can be probed, in particular, there are relatively few ways to probe correlations in these systems at mesoscopic length scales. In this thesis we present a new technique for probing correlations in ultracold atomic gases using ultralong-range Rydberg molecules. We will present a description of the relevant experimental apparatus and techniques developed for laser cooling and trapping ultracold mixtures of Sr, and a brief theoretical discussion on the relationship between the pair correlation function $g^{(2)}(R)$ and the excitation rates of ultralong-range Rydberg molecules. We present two publications: the first on using ultralong-range Rydberg molecules to probe $g^{(2)}(R)$ in thermal gases, and the second on the creation of heteronuclear ultralong-range Rydberg molecules from a strongly interacting Bose mixture of ^{88}Sr and ^{84}Sr. Finally, we will present conclu-

sions and a brief outlook for the future experiments utilizing this method.

Acknowledgments

About five months ago I was sitting in a hospital bed with a broken pelvis and not much to do other than think about how lucky I am. Lucky, for one, to simply be alive after an inelastic collision with an F-350 (a problem I thought I had left behind in Physics 101), but more importantly how lucky I am to have an amazing support structure of friends, family, co-workers and loved ones that were ready to drop anything and come to my aid. When I arrived at Rice, still not really knowing what physics was, not knowing how to ground a power supply properly, having never really succeeded at aligning a laser my advisor Tom Killian put his metaphorical arm around me and helped me find my "ground zen" and the rest is history. Without his and Barry Dunning's guidance I would have never become the physicist that I am proud to call myself today. Tom's mentorship has also blessed me with an amazing set of colleagues that I had the pleasure of spending many late nights in the lab with. When I arrived at Rice our optics table was empty, and Francisco and Roger were working out how to use a giant trash can to bake our vacuum chamber, "what have I gotten myself into?" I asked myself. Without them, our experiment would never be in the place it is today. The sage wisdom of Brian and Jim who had the working version of the system that we sought to build was also crucial to our success in building a strontium BEC machine at break-neck pace. Now our apparatus is a flourishing, thriving beast of a machine, manned by some truly gifted physicists ready to guide it into the future: Soumya, Yi, Chuanyu and Brent. I am constantly amazed at their ability to take something that someone else built and run with it (and quickly!), and can't wait to see what comes next for them.

I would also like to thank all of the mentors and teachers that helped me get to where I am today. From Lincoln Carr and the other professors at the Colorado

School of Mines who helped me realized that physics is actually pretty cool, and that they pay you to go to graduate school, to the amazing teachers I had at RHAM High School that prepared me for life. From english class with Ms. B and Mr. Brooks to calculus with Ms. Erlandsen I still find myself using the skills that they taught me every day.

Outside of the lab Rice provided me with an amazing group of friends and an equally amazing place to make more. All of the people at Valhalla, where I spent many an hour and many a 65 cents on Lone Stars, really made life interesting. Never a dull moment when you put a bunch of graduate students in the same room with a dash of ethanol. I'd list every friend I made at Rice here, but I think I'd end up with a thesis that is about twice as long as it is now! You are all amazing, and I could have never made it through eight long years at Rice without you!

Finally, I'd like to thank all of my family and my amazing girlfriend Alison. Thanks to them putting up with my questions like "what does nocturnal mean?" as a child and my explanations about weird physics that I was really excited about as the adult child I am today. Thanks to my grandfather George Bean who taught me to think the way I do, and for our long talks about how to debug his FreeCell website. Thanks to my parents and brother who have given me unwavering support as I navigated my way through college and graduate school. Thanks to Alison for joining me in this crazy journey of life full of physics, cats named Sushi, and things with sushi on them, I love you.

Contents

Illustrations

Tables

To Poppy

Chapter 1

Introduction

This thesis is a presentation of work pertaining to the use of ultralong-range Rydberg molecules as probes of spatial correlations in quantum gases. In this document we present an introduction where we discuss the basics of Strontium, Rydberg atoms and molecules, and the connection between molecular excitation and the pair correlation function $g^{(2)}(R)$. In the second chapter we discuss the experimental apparatus used in this work, particularly pertaining to the laser cooling and trapping of strontium mixtures and Rydberg excitation. The third chapter discusses the factors that contribute to the observed excitation rate and lineshape of ultralong-range Rydberg molecules and its precise relationship to $g^{(2)}(R)$. We include two publications: the first regarding the measurement of $g^{(2)}(R)$ in a thermal gas of identical bosons, identical fermions and distinguishable fermions, and the second regarding the excitation of heteronuclear ultralong-range Rydberg molecules from a strongly interacting mixture of ^{84}Sr and ^{88}Sr. Finally, we present conclusions and a brief discussion of the future work to be performed on the Rydberg apparatus.

1.1 Strontium

Stronitum (Sr) is an alkaline earth atom with atomic number 38. The electronic ground state of Sr is a closed s shell with electronic state $5s^2\,{}^1S_0$. There are four stable isotopes of strontium: three bosons, ^{88}Sr, ^{86}Sr, and ^{84}Sr with no nuclear spin, and one fermion, ^{87}Sr, with nuclear spin $I = 9/2$. In contrast with atoms more commonly used in laser cooling experiments such as Rb and other alkali atoms, Sr has two valence electrons, which permits two spin configurations: singlet and triplet. These two spin configurations have independent series of states that are both useful in laser cooling, and the transitions relevant to this work are shown in the term diagram in Figure 1.1.

The two spin configurations of the valence shell are both useful in laser cooling. The broad transition to the $5s5p\,{}^1P_1$ state provides a strong cycling transition for initial laser cooling. The large photon recoil and fast scattering rate allow for efficient laser cooling to about 1 mK. Transitions to the $5s5p\,{}^3P_J$ manifold are dipole-forbidden, but a small amount of admixture with the singlet series allows for very narrow transitions [1]. The $5s^2\,{}^1S_0 \rightarrow 5s5p\,{}^3P_1$ transition can be used for laser cooling to temperatures as low as $1\,\mu$K due to its 7.5 kHz natural linewidth [2, 3], and has been used to study fundamental physics of Doppler cooling [4]. The ultra-narrow clock transition to the $5s5p\,{}^3P_0$ state has been used in some of the most accurate atomic clocks, achieving fractional uncertainties as low as 2×10^{-18} [5].

The electrons in the $5s^2\,{}^1S_0$ state form a singlet with no magnetic moment. Without a magnetic moment, magnetic trapping techniques are not available for Sr in the

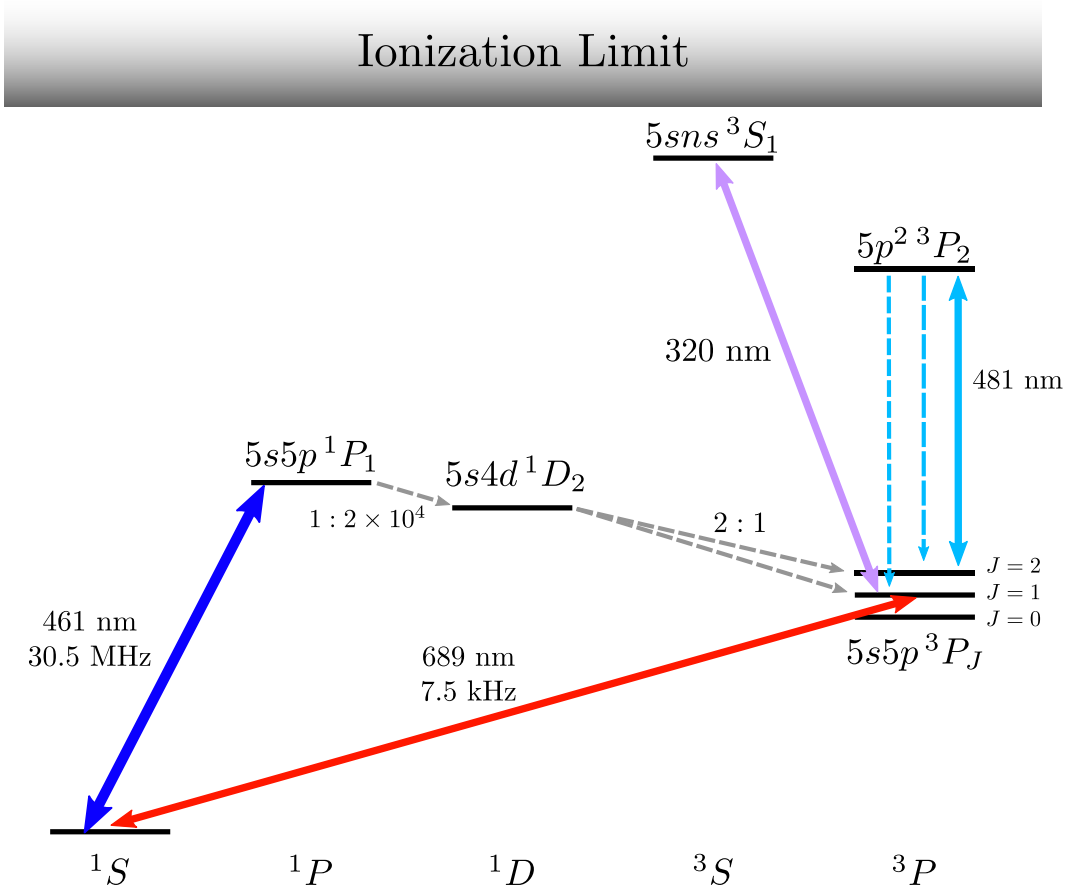

Figure 1.1 : An energy level diagram for Sr. We omit the hyperfine structure of ^{87}Sr here. The broad and narrow laser cooling transitions are indicated with red and blue arrows, and their linewidths are listed below their nominal wavelengths. Dashed gray arrows indicate the weak spontaneous decay path that populates the metastable $5s5p\,^3P_2$ state. One in 2×10^4 atoms decays from the $5s5p\,^1P_1$ state to the $5s4d\,^1D_2$ state, which decays to the $5s5p\,^3P_2$ and $5s5p\,^3P_1$ states with a branching ratio of 2:1. The Rydberg transition is shown in purple and the repumping transition is shown in light blue.

ground state, and optical dipole traps must be used [6]. The $I = 9/2$ ground state of ^{87}Sr has a magnetic moment, but it is too small ($\sim 10^{-3}\,\mu_B$) to be used effectively in magnetic trapping.

The absence of an unpaired electron spin leaves the ground state with no hyperfine structure. Without a magnetically sensitive ground state manifold there are no magnetic Feshbach resonances as found in alkali atoms [7], or atoms with open f- or d-shells such as Dy, Er and Cr [8, 9]. Magnetic Feshbach resonances are widely used in ultracold atom experiments to tune interatomic interactions by modifying the s-wave scattering length a. Despite the lack of magnetic Feshbach resonances, the ten binary combinations of stable Sr isotopes can act as a proxy for tunable interactions strengths ranging from nearly zero (^{88}Sr + ^{88}Sr) to very large and repulsive (^{84}Sr + ^{88}Sr); we will take advantage of this in the work presented here. The scattering lengths for various Sr mixtures are shown in Table 1.1.

Table 1.1 : The s-wave scattering length for all colliding pairs of stable Sr isotopes given in units of the Bohr radius $a_0 = 0.05$ nm [10, 11].

	^{84}Sr	^{86}Sr	^{87}Sr	^{88}Sr
^{84}Sr	124	21	-56	1800
^{86}Sr		810.6	164	98
^{87}Sr			97	44
^{88}Sr				-3

The work in this thesis makes use of ultracold gases of various combinations of Sr

isotopes that have different particle statistics. We use ^{84}Sr as an approximation of a non-interacting gas of thermal bosons, and can also use it to create Bose-Einstein condensates (BECs). We use the ten-fold degenerate ground state of ^{87}Sr to approximate a gas of distinguishable particles. We can also create spin polarized ^{87}Sr samples and use ^{84}Sr to sympathetically cool them to create a cold gas of indistinguishable fermions in a single internal state. We also prepare strongly interacting mixtures of ^{84}Sr + ^{88}Sr and produce heteronuclear Rydberg molecules.

1.2 Strontium Rydberg Atoms

A Rydberg atom is an atom that has been excited to an electronic state with a high principal quantum number $n \gtrsim 20$. The binding energy of the Rydberg electron is small compared to the ground state, approximately $-1/2n^2$ in atomic units. This weakly bound state results in a relatively slow-moving electron in a large orbit with radius $2n^2$ atomic units. The Rydberg electron wavefunction is approximately hydrogenic because it spends much of its orbit far away from the positively charged ionic core. For Rydberg states of lower angular momentum, ℓ, the microscopic details of the interaction with the ionic core give rise to a phase shift that manifests itself, to first order, as a modification to the principal quantum number $n^* = n - \delta_\ell$. The hydrogenic character of Rydberg states allows their properties to be parameterized quite accurately by only the principal quantum number, n, and the quantum defect, δ_ℓ, resulting in universal scaling properties for Rydberg series of any species. Table 1.2 lists some common scaling laws for Rydberg atoms and typical values for the

Table 1.2 : List of Rydberg scaling laws and typical values for the $5s38s\,^3S_1$ state of Sr.

Property	n scaling	Sr $5s38s\,^3S_1$
Binding Energy	n^{-2}	1200 cm^{-1}
Radiative Lifetime	n^3	21 μs [14]
Rydberg Radius $\langle r \rangle$	n^2	2200 a_0
Ionization Field	n^{-4}	225 V/cm
Polarizability	n^7	7 MHz / (V/cm)^2 [15]
$\nu = 0$ Binding Energy	n^{-6}	9.8 MHz [14]

$5s38s\,^3S_1$ state of Sr with quantum defect $\delta = 3.37$. In this work we focus on the $5sns\,^3S_1$ series. A full table of quantum defects for Sr is given in [12], and the most recent measured values for $5sns\,^3S_1$ and $5snd\,^3D_J$ states are presented in [13].

Rydberg atoms have been a subject of interest in atomic physics since the late 19th century. A seminal study of the interactions between Rydberg atoms and ground-state atoms was performed in 1934 Amaldi and Segrè, who observed broadening of Rydberg lines in the presence of various gases [16, 17] due to collisions between the low-energy Rydberg electron and the background gas atoms. These observations led Fermi to develop the well-known theory of the Fermi-pseudopotential [18] parameterized by the s-wave scattering length that is ubiquitous in modern atomic physics.

With the development of laser cooling and trapping in the late 20th century

[19] access to ultracold quantum gases became widespread, and interest in exciting Rydberg states in ultracold atomic gases followed. The strong dipole-dipole interactions between Rydberg atoms gives rise to the so-called Rydberg blockade where the presence of one Rydberg atom shifts the energy of a second excitation within the "blockade radius" out of resonance with the excitation laser. When many atoms are within the blockade radius Rydberg excitation creates a many-body superposition of ground-state atoms and a single Rydberg atom. The Rydberg blockade has also been used to induce strong interactions between photons to create optical transistors [20], implement quantum gates [21], and can potentially be used to increase the performance of optical atomic clocks [22].

Rydberg series are a universal feature of atomic systems. For alkali atoms the Rydberg series very closely resembles hydrogen with a single ionization channel, while atoms with additional valence electrons such as Sr have multiple ionization channels due to the possible configurations of the remaining valence electron(s). The Rydberg series of different channels can perturb each other when terms of each series have similar energy. Calculation of the Rydberg series for multi-electron atoms can be accomplished using multichannel quantum defect theory [23], but experimentally the interference of these channels results in an n-dependent quantum defect. In Sr, these interferences only occur at lower principal quantum numbers [13, 24] and the quantum defects are nearly constant, particularly for the $^3S_1$ series used in this work.

1.3 Ultralong-range Rydberg Molecules

The excited electron of a Rydberg atom spends much of its orbit far away from the parent nucleus. In a sufficiently dense environment the Rydberg electron may encounter a ground-state atom in the background medium and scatter off of it. The effect of this interaction was first observed in 1934 by Segrè and Amaldi [17] as a blue-shift of Rydberg lines in Na in the presence of hydrogen and later explained by Fermi [18]. The theory of collisions between neutral atoms and Rydberg electrons was extended by Omont [25] in a paper where he notes the periodic revival of interest in the broadening of Rydberg lines and accurately predicts that the advent of tunable lasers would (again) rekindle interest in the subject. The work of Fermi and Omont shows that the interaction of the Rydberg electron and a neutral atom gives rise to a potential that follows the oscillatory shape of the Rydberg wavefunction. In 2000 Greene, Dickenson and Sadeghpour observed that when this interaction is attractive the shallow, long-range potential supports a manifold of molecular states with binding energies on the order of MHz–GHz and bond lengths of $\sim n^2$ atomic units that could be stably formed in ultracold gases. These new bound states were thus called ultralong-range Rydberg molecules (RMs).

The first RMs were observed in 2009 by Bendkowsky et al. by exciting a spherically symmetric ns Rydberg atom in a cold cloud of Rb [26]. Following the initial observation RMs have been observed in Cs [27], Sr [15] and K [28]. Beyond spherically symmetric s states, excitation to degenerate Rydberg manifolds of high angular momentum, or to s states in Cs which has a near-integral quantum defect, produces

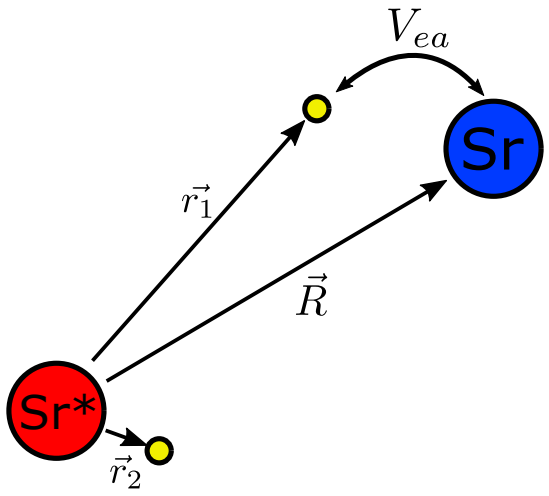

Figure 1.2 : A cartoon diagram of an excited Rydberg atom (red) in the vicinity of a ground state Sr atom (blue). The origin of the coordinates are fixed to the excited atom, $\vec{R}$ is the distance between the two nuclei, $\vec{r_1}$ and $\vec{r_2}$ are the coordinates for the two valence electrons, and V_{ea} is the interaction of the excited electron and the neutral perturber.

so-called trilobite molecules [27] with very large permanent electric dipole moments. In Rb, the presence of a p-wave shape resonance in the electron-neutral scattering can also admix higher angular momentum states allowing excitation to pendular butterfly states which also posses very large permanent dipole moments [29]. Most recently, observations of heteronuclear RMs comprised of different isotopes of Sr [30] and mixtures of Cs and K [28] have been reported.

To obtain the RM potentials, we consider the Rydberg-neutral system in the Born-Oppenheimer approximation in a frame with the Rydberg core fixed at the

origin. The system Hamiltonian (see Figure 1.2),

$$H = H_a(\vec{R}) + H_e(\vec{r}_1, \vec{r}_2) + V_{ea}(\vec{R}, \vec{r}_1, \vec{r}_2)\,, \tag{1.1}$$

has three parts describing the kinetic energy of the neutral perturber at $\vec{R}$ (H_a), the electronic motion of the two active valence electrons at $\vec{r}_1$ and $\vec{r}_2$ (H_e) and the interaction of the Rydberg electron and the perturber atom (V_{ea}). When V_{ea} is treated perturbatively the eigenstates of the bare Hamiltonian $H_a + H_e$ are simply the electronic eigenstates of the Rydberg atom and the relative motion of the two nuclei. For strontium, the e-Sr interaction is approximated by the pseudopotential with the semiclassical electron momentum $\hbar k(\vec{r_i}) = \sqrt{2m_e(e^2/(4\pi\epsilon_0 r_i) - E_n)}$

$$V_{ea}(\vec{R}, \vec{r}_1, \vec{r}_2) = \sum_{i=1}^{2} \frac{2\pi\hbar^2 A_s[k(\vec{r_i})]}{m_e}\delta(\vec{r_i} - \vec{R}) + \frac{6\pi\hbar^2 A_p^3}{m_e}\overleftarrow{\nabla}\delta(\vec{r_i} - \vec{R})\vec{\nabla}. \tag{1.2}$$

The strength of the s- and p-wave interactions are parameterized by the scattering lengths $A_s(0) = -13.3\,a_0$ and $A_p = 9.7\,a_0$, respectively, resulting in an attractive potential. At large distances from the ionic core the momentum dependence of the scattering length can be neglected. In alkali atoms, the p-wave scattering has a large effect on the RM potential [31], and the Hamiltonian also includes spin-orbit and hyperfine structure effects which are not present in Sr [32, 33].

The $5sns\,^3S_1$ states used in this work are well separated from other angular momentum states because of the quantum defect due to the interaction of the Rydberg electron with the ionic core. Therefore the RM potential curve can be calculated using first order perturbation theory integrating over the electronic degrees of freedom. The $5sns\,^3S_1$ state is well approximated by an appropriately symmetrized

combination of the $5s$ and ns orbitals [15]

$$\Psi(\vec{r_1},\vec{r_2}) \simeq \frac{1}{\sqrt{2}}(\phi_{5s}(\vec{r_1})\psi_{ns}(\vec{r_2}) - \psi_{ns}(\vec{r_1})\phi_{5s}(\vec{r_2})) \tag{1.3}$$

at large internuclear separation $R \gtrsim 100\, a_0$ the $5s$ orbital vanishes, yielding the RM potential curve

$$V(\vec{R}) = \frac{2\pi\hbar^2 A_s[k(\vec{R})]}{m_e}\left|\psi_{ns}(\vec{R})\right|^2 + \frac{6\pi\hbar^2 A_p^3}{m_e}\left|\vec{\nabla}\psi_{ns}(\vec{R})\right|^2. \tag{1.4}$$

Having integrated out the electronic degrees of freedom, the effective Hamiltonian for the atomic motion, $H_a + V(\vec{R})$, can be solved using this potential curve to obtain the spectrum of vibrational bound states labeled with quantum number ν. As shown in Figure 1.3, RMs appear as a series of spectral resonances detuned from the bare atomic energy by their binding energy. The positions and relative strengths of these lines can be used to extract information about the the e-Sr potential [15].

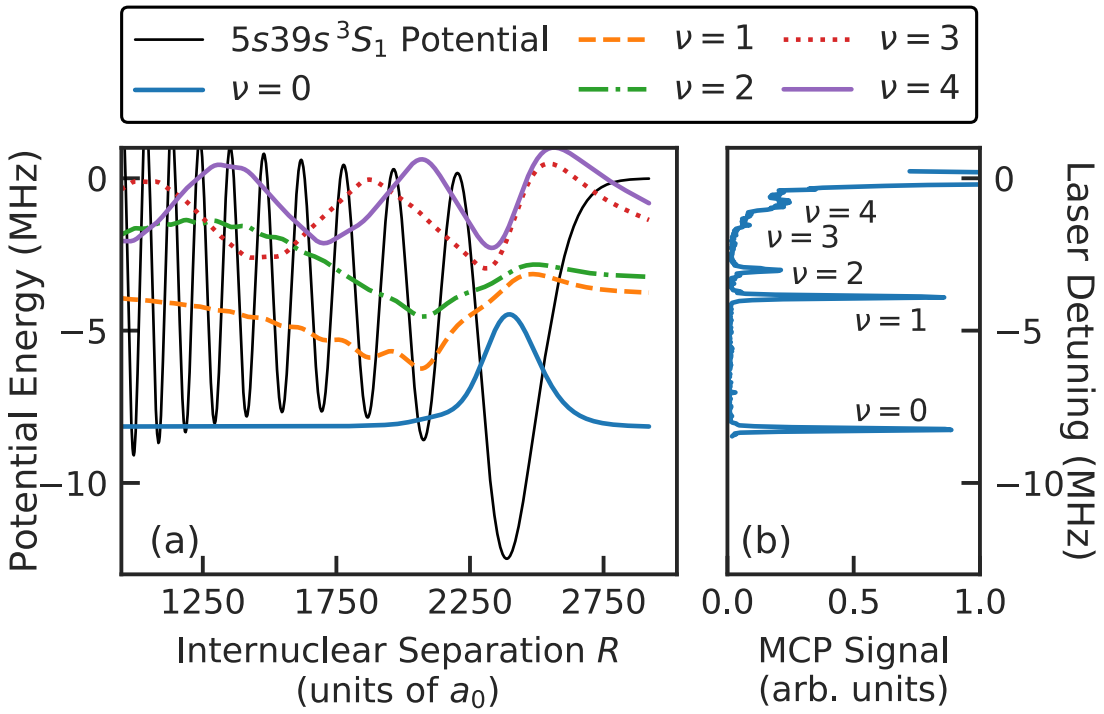

Figure 1.3 : a) The Rydberg Molecule potential for the $5s39s\,^3S_1$ state is shown in black, and the vibrational eigenstates, ν, are shown offset by their binding energy. b) The corresponding detector signal observed when scanning the Rydberg excitation laser to the red of the $5s39s\,^3S_1$ atomic line. This figure appears in [30].

Though most of the discussion above concerns two-body RM states, it is possible to form large oligomers via the same e-Sr scattering. We have signatures of up to five-body bound states in our lab, as shown in Figure 1.4. Qualitatively a higher-order state is formed simply by adding another perturber atom nearby the excited Rydberg atom, and the corresponding binding energy is simply the sum of the individual dimer binding energies. Corrections to the oligomer binding energies

due to perturber-perturber interaction have been predicted [34], but have yet to be observed experimentally.

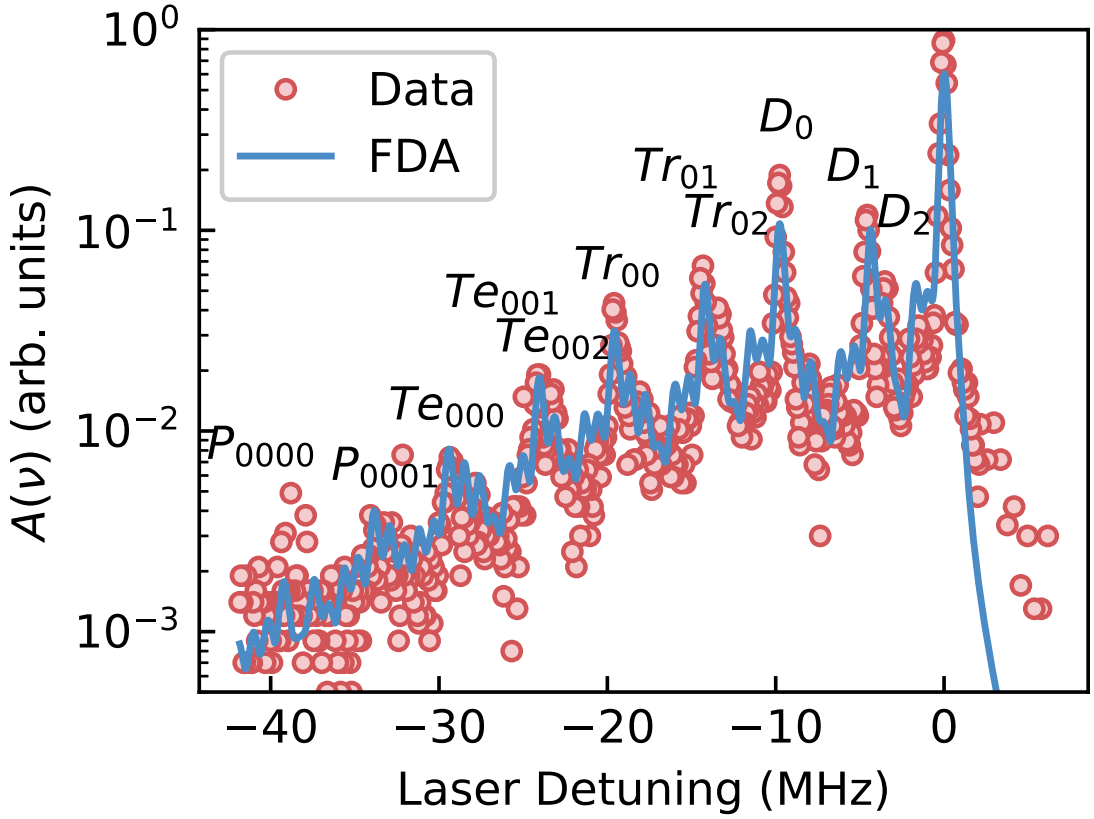

Figure 1.4 : The $5s38s\,^3S_1$ spectrum, $A(\nu)$, in a BEC of ^{84}Sr shown on a log scale. The experimental data is shown by the circles and the solid line shows a calculation of the spectrum using a functional determinant approach (FDA). Selected RM resonances are labeled D (dimer), Tr (trimer), Te (tetramer) and P (pentamer); vibrational quantum numbers are indicated by the subscripts. This figure appears in [35]

.

1.4 Rydberg molecules as probes of correlations

A typical atomic physics experiment probes a dilute cloud of atoms or molecules using an external field, typically a laser beam or microwave field. The response of the system to the applied field is directly related to the energy spectrum of the underlying Hamiltonian that describes the quantum system under consideration. These techniques are useful for studying the dynamics of a system with relatively few degrees of freedom, and have been instrumental in our understanding of atomic and molecular spectra. As we move from single-particle to many-body physics, however, the energy spectrum does not tell the whole story.

Many-body systems typically have large numbers of degrees of freedom, which leads to an exponentially large Hilbert space resulting in a very dense and complex excitation spectrum. However, many-body states may also express themselves through spatial correlations. In ultracold atomic systems these correlations can arise simply from Bose or Fermi quantum statistics [36–40], from magnetic ordering [41, 42], or from myriad other many-body effects [7, 43]. Ultracold atomic systems provide superior purity and tunability that allows for engineering of many-body states that map to models of condensed-matter physics, so methods for measuring these correlations are of general interest.

The purity and flexibility of ultracold atomic systems comes at the expense of isolating of the system in an ultra-high vacuum chamber, which leaves experimentalists with relatively few options to probe spatial correlations *in situ*. A few methods have been used to probe *in situ* spatial correlations to great effect: measurements

of three-body loss rates and inelastic losses probe correlations at $R \sim 0$ [37, 44], and recent developments in quantum gas microscopy allows for single-site resolved imaging of many-body systems, which directly measures many-body correlations on the order of the optical lattice wavelength (see Figure 1.5) [45, 46].

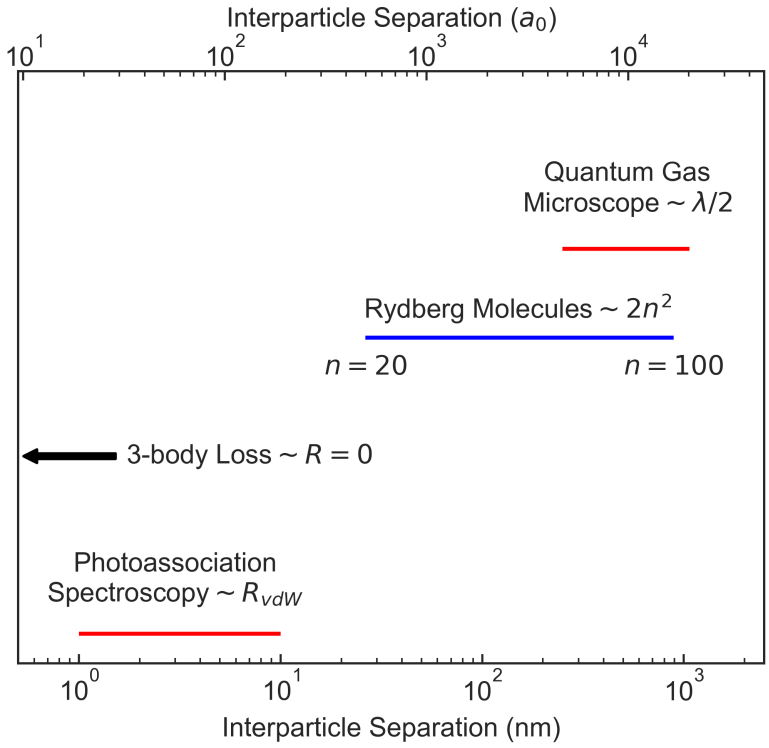

Figure 1.5 : A pictorial representation of the length scales probed by typical methods available to ultracold atomic physics experiments.

Photoassociation spectroscopy of low-lying energy levels has been used to map the ground-state potential of colliding atom pairs [47–51]. This method probes the scattering wavefunction at very short range, $R \lesssim 100\, a_0$. As shown in Figure 1.5

there is a relatively large gap in the length scales that can be probed using traditional techniques. To this end, we propose using the photoassociation of ultralong-range Rydberg molecules to fill this gap and probe the nonlocal pair correlation function $g^{(2)}(R)$ on this intermediate length scale.

As discussed in the previous section, a RM is comprised of a highly excited Rydberg atom and a nearby neutral perturber. In particular, the ground state of the RM potential is a highly localized wavepacket (Figure 5.1). Semiclassically the formation of such a highly localized dimer requires its constituents to be separated by $R_n \sim 2(n-\delta_\ell)^2$ at the time of photoexcitation. Therefore, the molecular excitation rate will be proportional to the relative probability of finding two particles at $R \sim R_n$, which is quantified by the pair-correlation function $g^{(2)}(R_n)$. Rydberg molecule dimers have bond lengths ranging from $400 - 10^4\, a_0$, corresponding to $n = 20 - 75$ for $5sns\,{}^3S_1$ RMs.

The pair correlation function is defined generally as an expectation value of field operators $\hat{\Psi}$ evaluated at positions $\mathbf{r}$ and $\mathbf{r}'$,

$$g^{(2)}(\mathbf{r},\mathbf{r}') = \frac{\langle \hat{\Psi}^\dagger(\mathbf{r})\hat{\Psi}^\dagger(\mathbf{r}')\hat{\Psi}(\mathbf{r}')\hat{\Psi}(\mathbf{r})\rangle}{\langle \hat{\Psi}^\dagger(\mathbf{r})\hat{\Psi}(\mathbf{r})\rangle\langle \hat{\Psi}^\dagger(\mathbf{r}')\hat{\Psi}(\mathbf{r}')\rangle}, \tag{1.5}$$

where $\hat{\Psi}^\dagger(\mathbf{r})$ and $\hat{\Psi}(\mathbf{r})$ are the creation and annihilation operators for a particle at position $\mathbf{r}$ respectively. The expectation value can be taken over a single many body state or considered as a thermal average. If the system has appropriate symmetry, the coordinates can be transformed to only consider the separation $R = |\mathbf{r}-\mathbf{r}'|$. The definition of $g^{(2)}(R)$ above is very general, but in the context of this thesis we will be considering correlations in the density of thermal gases of strontium.

Even in a system as simple as a thermal gas of identical bosons or fermions the quantum nature of matter creates correlations. Due to the spin-statistics theorem, the many-body wavefunction of a gas of idential bosons (fermions) must have even (odd) parity under exchange of particle labels [52]. The implications of this principle are readily observed in a system of two particles. The two-particle wavefunction for two identical particles is given by a combination of single-particle wavefunctions ψ_1 and ψ_2,

$$\Psi(x,y) = \psi_1(x)\psi_2(y) + \epsilon\psi_1(y)\psi_2(x) \tag{1.6}$$

where ϵ takes a value of $+1$ for bosons and -1 for fermions. It is clear that this wavefunction satisfies the spin statistics theorem under the exchange of particle labels ($\Psi(x,y) = \epsilon\Psi(y,x)$), and that, for the fermionic case, the wavefunction is zero for $x = y$. This zero in the fermion wavefunction is the well-known Pauli exclusion principle, which states that two identical fermions cannot be in the same quantum state.

This simple example can be extended to a many-body picture using second quantization, and it can be found that for a non-interacting thermal gas the pair-correlation function $g^{(2)}(R)$ can be written as

$$g^{(2)}(R) = 1 + \epsilon\exp(-2\pi R^2/\lambda_{dB}^2) \tag{1.7}$$

where ϵ is $+1$ for bosons and -1 for fermions, and $\lambda_{dB} = h/\sqrt{2\pi m k_B T}$ is the thermal de Broglie wavelength. The details of this derivation can be found in [36] and are also derived in Appendix A.

In this thesis we will study all of the factors that make up the RM excitation

rate, and determine how to extract $g^{(2)}(R)$ from the measured molecular spectra. We will also discuss the creation of heteronuclear and rotating RMs, as well as the effect of interactions on the spectrum and the implications of measuring $g^{(2)}(R)$ in these systems.

Chapter 2

Experimental Apparatus

2.1 Laser cooling and trapping of Sr

To create ultracold samples of Sr we employ standard techniques of laser cooling. The methods of laser cooling and trapping of single isotopes of Sr have been covered in detail in previous theses from our group [53, 54] and elsewhere [10]. In this section we will briefly discuss the standard laser cooling process and expand on the details of trapping ultracold Sr mixtures in subsequent sections.

A strontium atomic beam is emitted from an oven containing a solid strontium sample of natural isotopic abundance heated to 425°C. The beam is collimated using two-dimensional optical molasses operating on the $5s^2\,{}^1S_0 \rightarrow 5s5p\,{}^1P_1$ cycling transition. The hot atoms travel down a Zeeman slower where they are decelerated and captured in a broadband magneto-optical trap (MOT) operating on the $5s^2\,{}^1S_0 \rightarrow 5s5p\,{}^1P_1$ cycling transition at 461 nm that cools the atoms to about 1 mK. Atoms are lost from the broadband MOT via a weak spontaneous decay channel (branching ratio $1 : 2\times10^4$ [55]) to the metastable $5s5p\,{}^3P_2$ state via the $5s4d\,{}^1D_2$ state. The $5s5p\,{}^3P_2$ state is metastable and dark to the 461 nm light of the broadband MOT. Atoms in low-field-seeking states remain magnetically trapped around the zero of the quadrupole field of the MOT [56] with a $1/e$ lifetime of about 15

seconds. After the desired broadband MOT loading time, the atoms in the magnetic trap are retrieved using the $5s5p\,^3P_2 \rightarrow 5p^2\,^3P_2$ repumping transition at 481 nm. The $5p^2\,^3P_2$ state decays via dipole allowed transitions to the $5s5p\,^3P_1$ and $5s5p\,^3P_2$ states with a branching ratio of about $1:3$ [57]. The atoms in the $5s5p\,^3P_1$ state decay to the ground state, rapidly depleting the metastable population.

Repumped atoms are further cooled in a narrow-line MOT operating on the $5s^2\,^1S_0 \rightarrow 5s5p\,^3P_1$ intercombination line. The linewidth of the intercombination transition is 7.5 kHz, which results in a sample with temperature between 1 and 2 μK. The details of the narrow line cooling methods used here have been discussed at length elsewhere [2, 10, 58]. At the end of the narrow-band MOT sequence the atoms are loaded into an optical dipole trap (ODT) operating at 1064 nm. The dipole trap is comprised of two light sheets crossing at 90 degrees and an optional dimple beam that is mutually perpendicular to both sheets. The resulting trap is a disk that matches the dimensions of the narrow-band MOT, allowing for efficient loading into the ODT. Once atoms are loaded into the ODT we can perform evaporative cooling [59] to the desired final temperature, typically a few-hundred nanokelvin, before performing Rydberg excitation experiments.

2.2 Creation of ultracold Sr mixtures

2.2.1 Broadband MOT and imaging

The operation of the broadband MOT for a mixture of Sr isotopes is very straight forward. The relatively large linewidth of the $5s^2\,^1S_0 \rightarrow 5s5p\,^1P_1$ cycling transition

compared to the isotope shifts precludes simultaneous operation of broadband MOTs. Instead, we load the magnetic trap sequentially.

The MOT and Zeeman slower light are generated by injection locking two separate laser diodes using an extended cavity diode laser (ECDL). The ECDL is locked to the $5s^2\,{}^1S_0 \rightarrow 5s5p\,{}^1P_1$ transition using saturated absorption spectroscopy on a thermal vapor of Sr in a heated cell. The ECDL frequency can be shifted by applying a magnetic field to the vapor and shifting the frequency of the probed transition. We are able to shift the laser over the range of isotopes, about 300 MHz, without the ECDL mode-hopping or going multi-mode.

We choose the isotopes to be loaded using the experimental control program and adjust the loading time of each isotope to achieve the desired proportion of each isotope. After loading the trap we can also choose which isotope to image. The imagining light is derived from the same injection-locked diode that produces the MOT light [53]. There is minimal cross-talk in the absorption imaging the target isotope due to off-resonant absorption of the other isotope in the system, but we typically blow away the secondary isotope using a resonant 689 nm laser beam tuned to the $5s^2\,{}^1S_0 \rightarrow 5s5p\,{}^3P_1$ transition to remove any undesired background.

2.2.2 Simultaneous repumping of multiple isotopes

Once the desired combination of isotopes is magnetically trapped they must be retrieved from the metastable state to be further cooled in the narrow-band MOT. We employ a 481 nm diode laser (Toptical DL-100) to drive the $5s5p\,{}^3P_2 \rightarrow 5p^2\,{}^3P_2$ repumping transition. Repumping is critical for ^{84}Sr and ^{87}Sr due to their relatively

low natural abundance [60]. The repumping laser is shared between experiments in our lab, so in the past we locked the laser to a Te_2 reference using a side-of-fringe technique to roughly center the laser, and then applied a modulation to the laser current to broaden the spectrum to cover all isotopes. This method is susceptible to drifts in the lock point and does not efficiently allocate laser power across the spectrum. Once we started working with mixtures of the less abundant isotopes we found it necessary to improve our repumping scheme.

First we improved the method of controlling the repumping laser frequency. We stabilize the repumping laser using a scanning Fabry-Perót interfereometer to reference the 481 nm laser to the stable 689 nm ECDL, which is locked to a ultralow-expansion (ULE) cavity. This method is similar to other systems in [61] and [62]. Briefly, we use a home-built Fabry-Perót cavity with mirrors coated for high reflectivity at both 689 nm and 481 nm. The mirrors are 12.7 mm diameter concave-concave BK7 substrates from Lambda with radius of curvature of 50 mm on both sides and coatings from Blue Ridge Optics. One side of the substrate is coated with an anti-reflective coating for 461 nm, 481 nm, 633 nm and 689 nm. The second side is coated for 99.8% reflectivity of 481 nm and 689 nm, giving a finesse of about 1500. The free spectral range of the cavity is 1.5 GHz. The cavity length is scanned using a triangle waveform from a function generator to drive a piezoelectric stack on one of the mirrors. We monitor the transmission of each wavelength and digitize it using a DAQ from National Instruments (USB-6001). We measure the positions of the 481 nm and 689 nm fringes and apply PID feedback to the 481 nm laser to maintain a desired separation between two transmission peaks. We can apply an external volt-

age or manually set the set-point of the lock to scan the frequency of the repumper. A screenshot of the laser control program is shown in Figure 2.1.

With this improved stabilization method we can now more efficiently allocate the laser spectrum. The ideal method for repumping a single isotope is to run the laser on the $5s5p\,^3P_2 \rightarrow 5p^2\,^3P_2$ resonance. Unfortunately, that necessarily excludes efficient repumping of any other isotope that might be present. As stated before, when working with a mixture of ^{84}Sr and ^{87}Sr repumping both isotopes efficiently is crucial. The hyperfine structure of the ^{87}Sr repumping transition further complicates the scheme. To repump both isotopes we use an electro-optic modulator (EOM) to apply sidebands to the carrier light of the 481 nm laser. A schematic of the repumper laser system is shown in Figure 2.2.

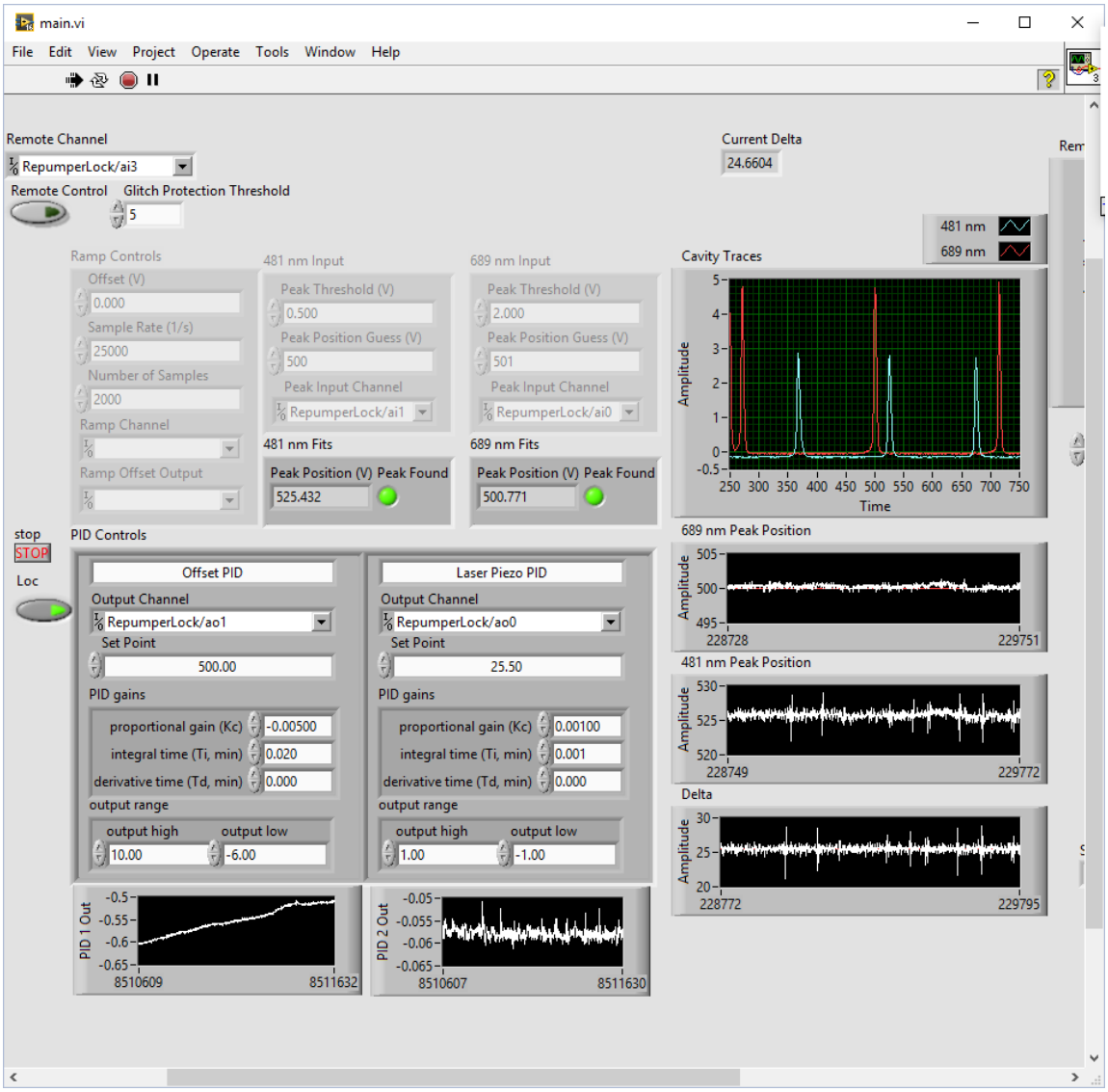

Figure 2.1 : A screenshot of the repumper control VI. The software identifies the relative position of the central 689 nm peak (red trace) and the 481 nm peak (blue trace) and uses a software-based PID control loop to hold the separation of the peaks constant by feeding back to the laser piezo. A second PID loop is used to control the DC offset of the ramp that scans the Fabry-Perót cavity to avoid drifts out of the software's peak detection window.

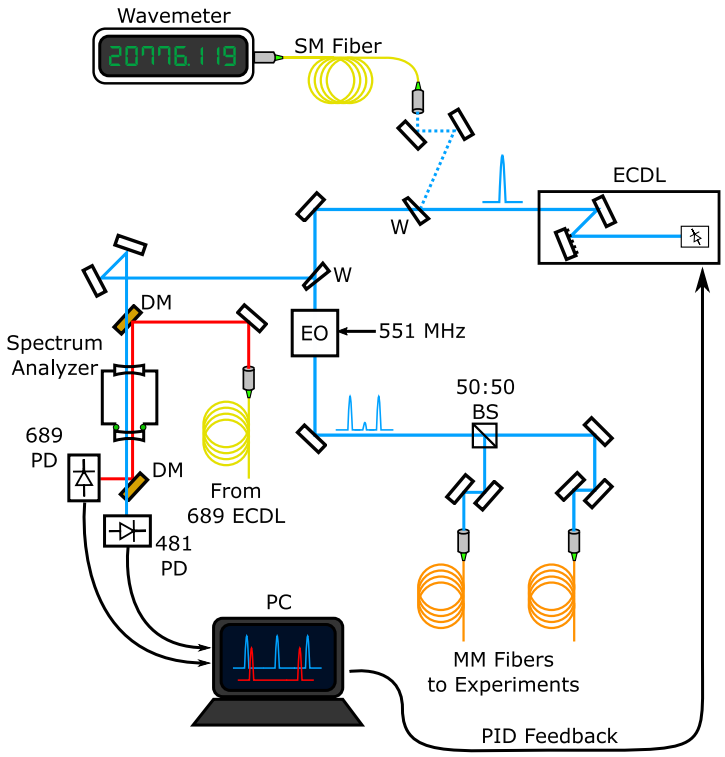

Figure 2.2 : A schematic of the repumper laser system. An ECDL produces about 8 mW of 481 nm light, a small portion of which is picked off by a wedge (W) and is coupled into a wavemeter with a single-mode (SM) fiber. A second wedge is used to bring a beam to an optical spectrum analyzer after passing through a dichroic mirror (DM). The dichroic mirror is used to reflect 689 nm light from the main 689 nm ECDL into the spectrum analyzer. The spectrum analyzer is driven with a triangle wave from a function generator, and the transmission of each wavelength is measured by two photodiodes (PD); the PD signals are used to stabilize the laser (see text). An electro-optic modulator (EO) applies sidebands to the laser light to hit both ^{84}Sr and ^{87}Sr and is split by a 50/50 beam splitter (BS) to send light to the neutral and Rydberg experiments through multi-mode (MM) fibers.

To determine the correct sideband frequencies for the EOM we first had to perform spectroscopy on the repumping transition for all isotopes. We used the new

locking scheme to scan the repumping laser over the $5s5p\,^3P_2 \rightarrow 5p^2\,^3P_2$ transition for each isotope, monitoring the atom number after applying a repumping pulse and recapturing the atoms in the broadband MOT before imaging. The resulting spectra are shown in Figure 2.4 and Figure 2.5. For each recorded frequency measurement we recorded the wavelength of the laser measured on a wavemeter to determine the conversion between cavity set point and laser frequency. We can then fit the measured spectral lines and extract the line center, an example spectrum for ^{84}Sr is shown in Figure 2.3.

As shown in Figure 2.4 the repumping spectrum for ^{87}Sr is much more complex than for the bosons. The spectrum is dominated by the hyperfine structure of the $5s5p\,^3P_2$ level of ^{87}Sr which has $F = 5/2 \cdots 13/2$ due to the combination of the nuclear spin $I = 9/2$ and the orbital angular momentum of the electrons $J = 2$. The upper state also has the same hyperfine structure, but the splitting is much smaller because the electrons are farther from the nucleus in the doubly-excited $5p^2$ state. The hyperfine structure of the upper state can be seen superposed on the $F = 9/2$ feature of the repumper spectrum in Figure 2.4. We can roughly extract the line centers of each hyperfine component and determine the center of mass line center for ^{87}Sr, but the uncertainty in the fit is much larger than that of the bosons (see Figure 2.3) due to the more complex structure of the fermionic spectrum.

With the line centers in hand we can devise a repumping scheme that targets the least abundant isotopes, ^{84}Sr and ^{87}Sr. The relative abundances of ^{86}Sr and ^{88}Sr are large enough that we can repump far from resonance and still achieve high loading rates. To precisely hit multiple isotopes we make use of an EOM (Qubig EO-565M2-

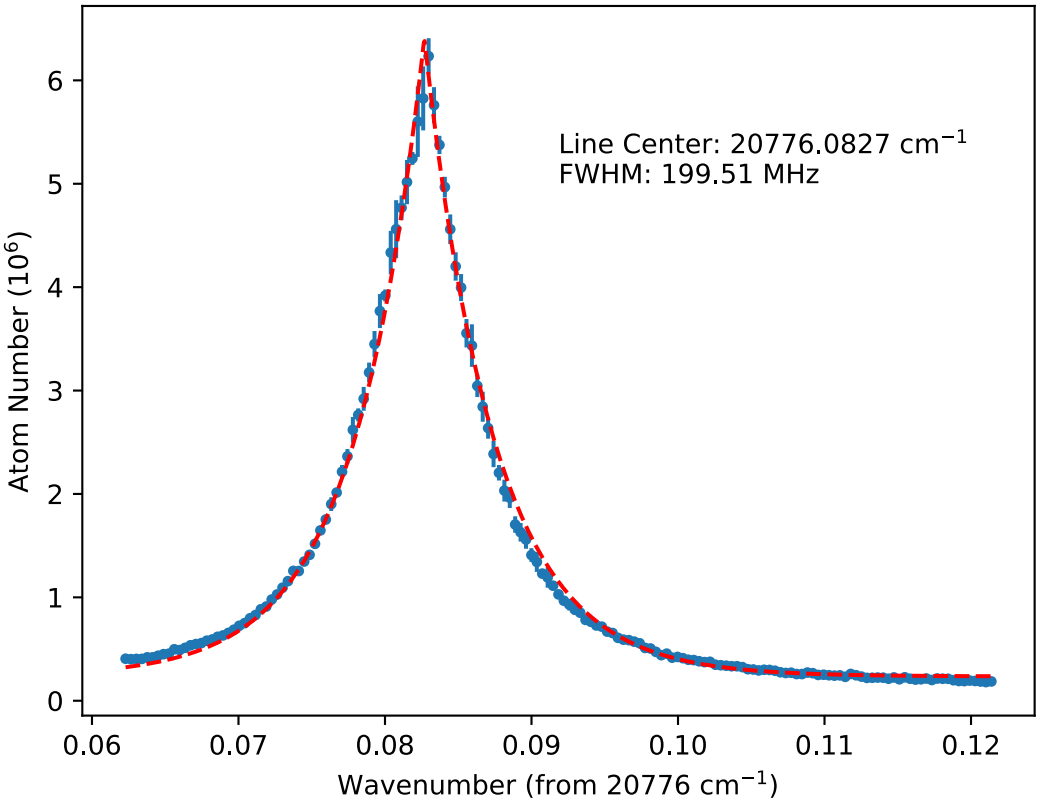

Figure 2.3 : An example fit for the ^{84}Sr repumping spectrum. The spectrum is fitted to a cusp lineshape to extract a line center. The x-axis detuning is calibrated using the readings from a wavemeter.

VIS) to apply sidebands to the 481 nm laser. We center the carrier +520 MHz from the ^{88}Sr resonance and apply a modulation of 550 MHz at a modulation depth of roughly π to maximize the power in the second order sidebands.

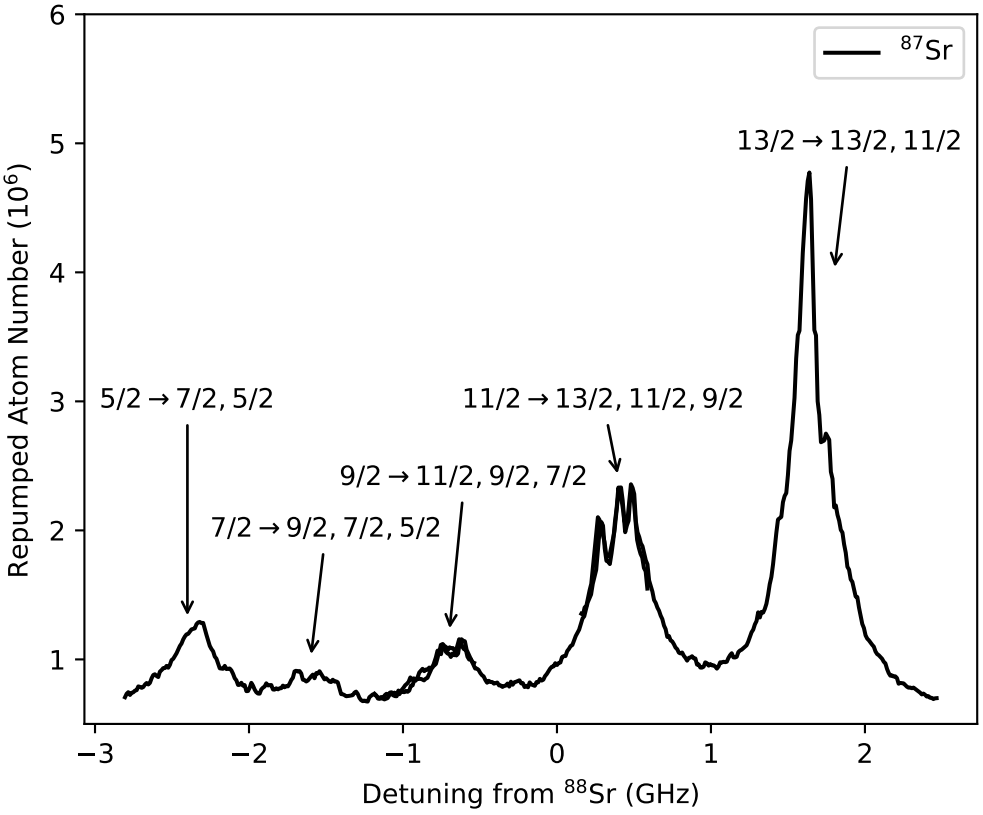

Figure 2.4 : The $5s5p\,^3P_2 \rightarrow 5p^2\,^3P_2$ spectrum for ^{87}Sr. The labels indicate the lower F to upper F transitions in each spectral feature. The structure of the spectrum is dominated by the hyperfind structure of the lower state, with smaller features within each line due to the hyperfine structure of the upper state.

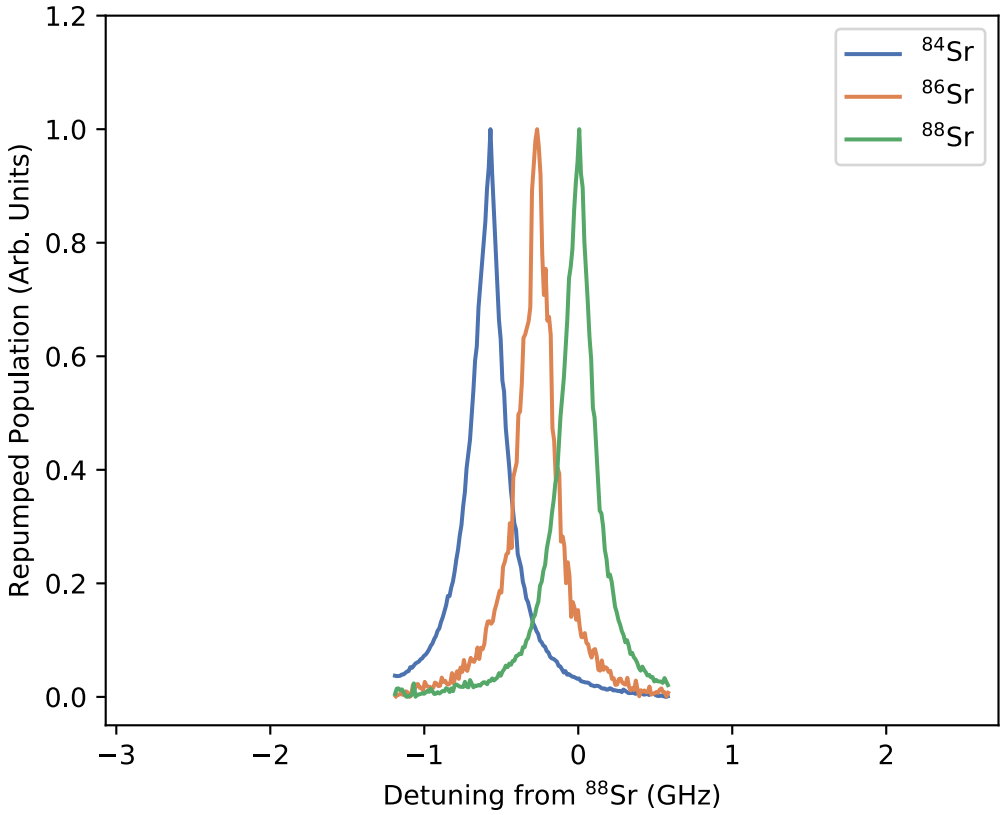

Figure 2.5 : The $5s5p\,^3P_2 \rightarrow 5p^2\,^3P_2$ spectrum for the bosonic isotopes of Sr. The spectra for the bosons are much simpler than that of ^{87}Sr due to the lack of hyperfine structure.

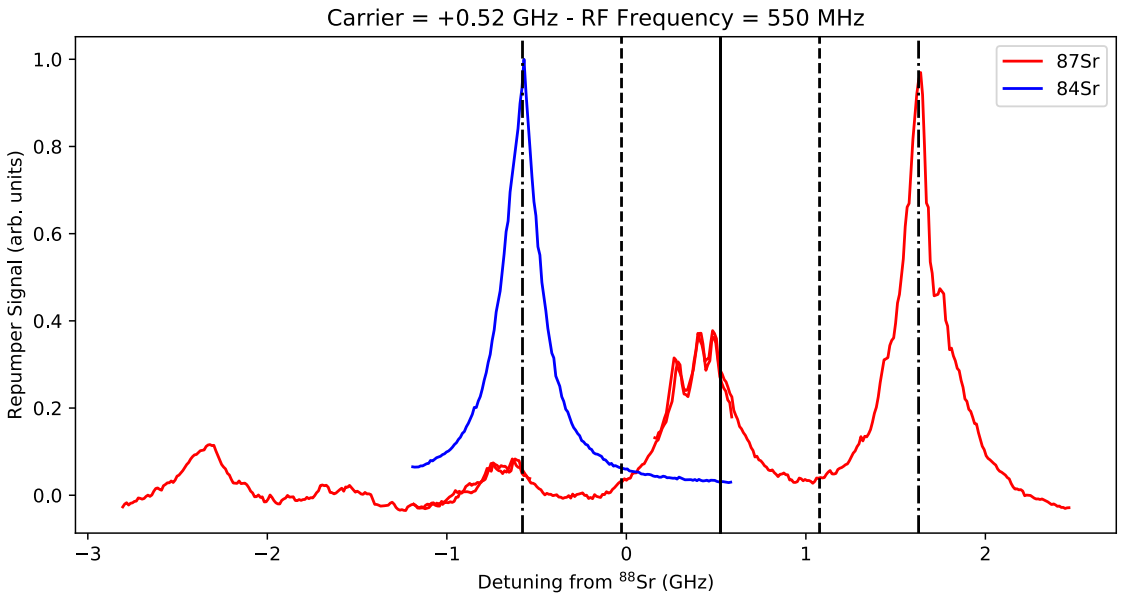

Figure 2.6 : The repumping spectrum for ^{84}Sr and ^{87}Sr with the carrier (solid line), first-order (dashed) and second-order (dot-dashed) sidebands indicated. The modulation frequency chosen here is 550 MHz.

2.2.3 Narrow-line cooling of a mixture

After the atoms are repumped from the magnetic trap using the scheme described in the previous section, they are further cooled to a final temperature between 1 and 2 μK using a narrow-line MOT operating on the $5s^2\,{}^1S_0 \rightarrow 5s5p\,{}^3P_1$ intercombination transition. Laser cooling on a narrow transition has been discussed at length in other publications, so we will only discuss the specifics of our experimental setup.

Unlike the initial broadband MOT, the narrow-line MOTs for each isotope can be run simultaneously due to the narrow linewidth of the intercombination transition (7.5 kHz) compared to the size of the isotope shift (about 100 MHz). To accomplish simultaneous cooling of binary isotope combinations we apply two or three diode lasers injection-locked by the main 689 nm oscillator, which is referenced to a high-finesse ULE cavity. The injection beam used for each diode laser is either -82 MHz or -1323 MHz detuned from the ^{88}Sr intercombination line, and is derived from a fiber for each diode allowing for the injection light to be changed with only minor realignment.

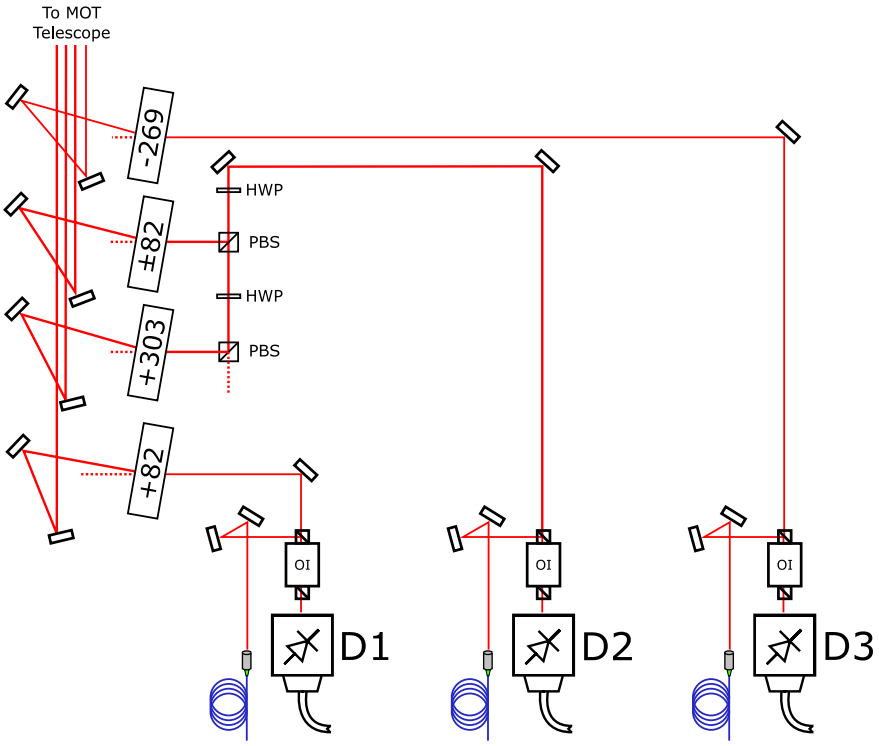

Figure 2.7 : The 689 nm laser system. Laser diodes D1, D2 and D3 are injection locked using stable 689 nm light from the ECDL locked to the ULE cavity via polarization-maintaining optical fibers. The light from the fibers is injected through the rejected port of the optical isolator (OI) after each diode. The frequency of the injection light can be changed without realignment of the injection lock. The MOT light is generated using AOMs to control the frequency and power of the light, power monitor optics are not shown for simplicity. A series of half-wave plates (HWP) and polarizing beam splitters (PBS) allows for the selection of the shift frequency of D2. The diffracted beams are aligned to co-propagate (separation is not to scale) and are sent to the beam-shaping optics for the narrow-line MOT (see [54] for more details).

The frequency and intensity of the MOT light for each isotope is controlled using by an AOM tuned to the appropriate isotope's intercombination line. The RF drive

Table 2.1 : The injection lock frequencies and AOM frequencies for various binary combinations of Sr isotopes. Injection frequencies are given in MHz relative to the ^{88}Sr $5s^2\,{}^1S_0 \rightarrow 5s5p\,{}^3P_1$ intercombination line. The lower table shows the nominal AOM frequencies (in MHz) used for each laser, the sign of the frequency indicates the diffraction order used.

Combination	D1 Injection Freq.	D2 Injection Freq.	D3 Injection Freq.
^{84}Sr + ^{88}Sr	-	−82	−82
^{84}Sr + ^{87}Sr	−1323	−82	−82

	D1 AOM	D2 AOM	D3 AOM
^{84}Sr + ^{88}Sr	-	+82	−269
^{84}Sr + ^{87}Sr	+82	+303	−269

for each AOM is generated by a voltage-controlled oscillator set by the experimental LabVIEW^{TM} program. All binary combinations of isotopes can be produced, but some are more useful than others. To save power, the beams are not combined using beam splitters or other optics, and are instead roughly co-propagating into the MOT beam generating optics (see Figure 2.7). The injection-lock frequencies and nominal AOM detuning for each binary isotope combination used in this work are listed in Table 2.1.

After the magnetic trap is loaded from the broadband MOT the 461 nm light is extinguished. After 50 ms the magnetic field gradient is switched from ∼40 G/cm to ∼4 G/cm, and the 689 nm MOT light and the 481 nm repumper are turned on. After 150 ms of capture the repumper is turned off and the MOT laser intensities

are reduced and brought very close to atomic resonance over a period of 600 ms further cooling the atoms to around 2μK and holding them against gravity. The optical dipole trap is turned on during the last 100 ms of the narrow-line MOT stage and the atoms are transferred with about 80% efficiency while maintaining their low temperature.

2.3 Optical Dipole Trap

After the narrow-line MOT the atoms have reached a temperature of around $2\,\mu$K and are loaded into an optical dipole trap formed by 1064 nm laser beams derived from a 50 W multimode fiber amplifier from IPG (YLR-50-1064-LP). The high-power, red-detuned laser light creates a potential that is attractive for Sr atoms in the $5s^2\,{}^1S_0$ state. Focusing the light down to a small spot creates a potential gradient and therefore a trapping force that is strong enough to hold the atoms against gravity.

The ODT system consists of three separate traps: Two perpendicular light sheets that cross at 90 degrees in the horizontal plane, and a dimple beam that propagates along gravity through the center of the intersection of the sheet traps. The light from the fiber amplifier is split and diffracted through an AOM for each trap, and each diffracted order is coupled into a high-power polarization-maintaining optical fiber from OZ Optics. The output of each fiber is collimated and passed through a series of beam-shaping lenses to produce the desired trap geometry at the atoms. Each beam passes through the chamber and is collected in a beam dump. A portion of the dumped light is sampled and monitored with a photodiode to actively control the trap

power. The power of the traps can be dynamically changed for evaporative cooling using our experimental software that controls a National Instruments waveform card. A schematic of the ODT laser system is shown in Figure 2.8. The details of the first sheet trap and the dimple trap have been covered in other work from our group [54], and we will only cover the addition of the second sheet trap here.

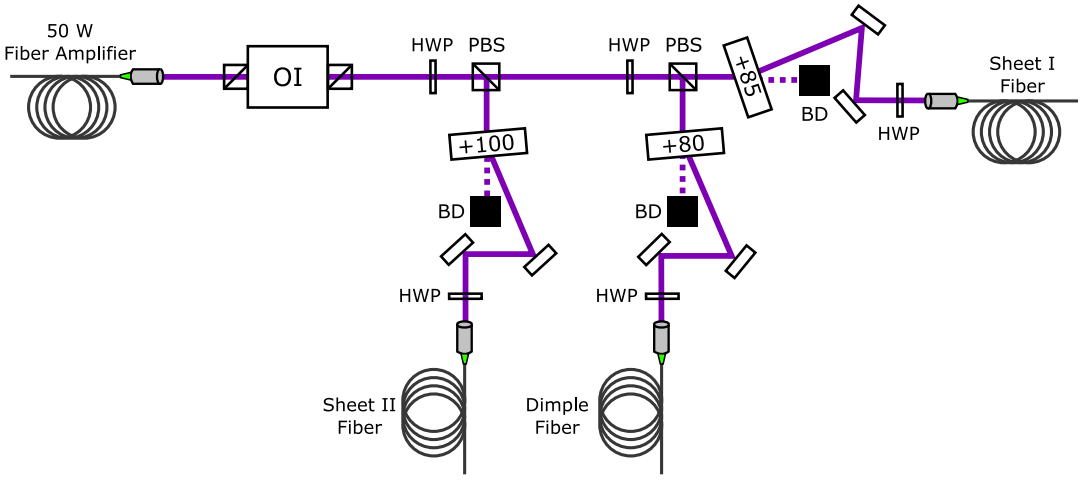

Figure 2.8 : A schematic of the input of the ODT laser system. 50 W of 1064 nm light from a multimode fiber amplifier passes through an optical isolator (OI). The initial 50 W is split using a series of $\lambda/2$ plates (HWP) and polarizing beam splitters (PBS). Each split beam is diffracted by an AOM with frequency indicated in the figure, and the zeroth order is sent to a beam dump (BD). Each of the diffracted beams is sent through another HWP to align the polarization to the axes of each trap fiber, which is then sent to the chamber.

The addition of a second sheet allows for the creation of higher density samples due to the additional longitudinal confinement provided by the mutual intersection

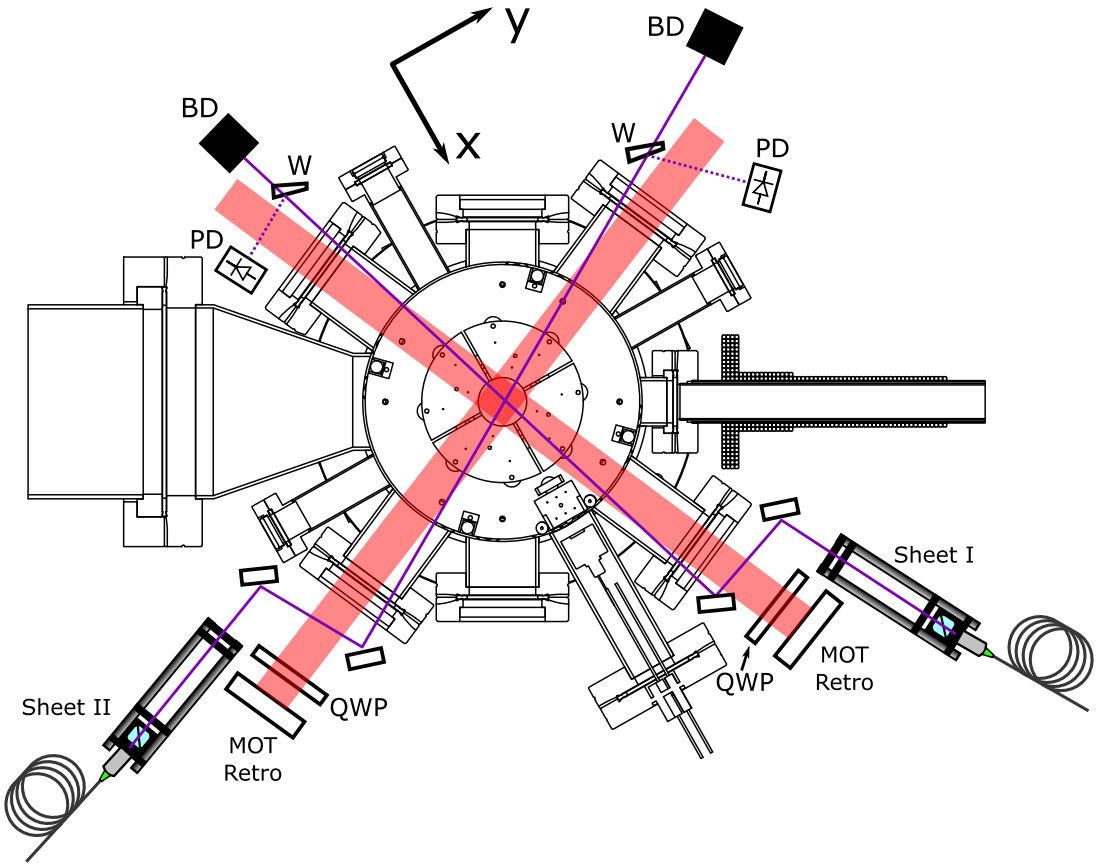

Figure 2.9 : A schematic of the output of the optical dipole trap system. The two sheet beams are launched from polarization-maintaining fibers and are shaped by a series of cylindrical lenses that create a tightly focused beam waist at the center of the chamber. The ODT beams (purple) are aligned to hit the single frequency narrow-line MOT (red beams). After passing through the chamber the ODT beams are sampled by a wedge (W) and monitored with a photodiode (PD) for power control. The majority of the power is transmitted through the wedge and collected with a beam dump (BD).

of two sheet beams, and to better match the shape of the single-frequency narrow-line MOT for better loading. The second sheet is aligned to be perpendicular to the original sheet (see Figure 2.9), and has $1/e^2$ radii of 27 μm in the vertical direction and 120 μm in the horizontal direction. A beam profile can be found in Appendix C.

The final beam is generated using a series of lenses in an optical cage system. A maximum of 6 W of 1064 nm light is emitted from a fiber collimator from OZ Optics and passes through a half waveplate and a cube to fix the polarization of the trap to be along the z-axis. The beam is shaped by three cylindrical lenses. The horizontal waist is generated by a single 400 mm lens and the vertical waist is formed using a telescope made with a -50 mm lens and 150 mm lens. The Rayleigh range of the tight axis is small, about 2 mm, so we place the optical cage assembly on a translation stage for fine tuning of the waist position onto the atoms. Once the beam is aligned, the assembly is locked to the in place using an optical post. A mechanical drawing of the optical cage, beam profile, bill of materials and drawings of home-built components are found in Appendix C.

2.4 Rydberg excitation and detection

2.4.1 Rydberg laser system

All of the experiments discussed in this thesis rely on the creation of Rydberg atoms and molecules. The properties of these exotic atomic states have been discussed in the introduction, but here we will discuss the specifics of the experimental setup

that is used to create them. Rydberg excitation is accomplished using a two-photon excitation comprised of a fixed 689 nm photon detuned from the $5s5p\,^3P_1$ state and a 320 nm photon that is tuned to the appropriate energy of the target $5sns\,^3S_1$ Rydberg state.

The 689 nm photons are derived from the injection-locked diode lasers that are used to produce the narrow-band MOT. The detuning is set by an AOM driven by a synthesizer to ensure high frequency accuracy. The 320 nm photon is derived from a frequency doubled 640 nm laser system. The 640 nm photons are created using an optical parametric oscillator (OPO) in combination with a sum-frequency generation stage (SFG). The OPO is pumped by 8.5 W of 1064 nm light from a fiber amplifier (YAR-15K-1064-LP-SF, IPG Photonics) which is seeded by a tunable fiber laser seed (Rock, NP Photonics) and sent into a bowtie cavity with a periodically polled nonlinear crystal inside. The pump photon is converted into a signal photon around 1.5 μm and an idler photon at about 3 μm. The signal light is resonant with the OPO cavity, and the wavelength is coarsely determined by the position of the nonlinear crystal in the pump beam. The idler photons are dumped. The cavity is comprised of a solid brass spacer and has no active stabilization, so the temperature of the cavity spacer is stabilized to within 0.1°C to prevent slow thermal drifts in the output wavelength. The wavelength of the signal light can be tuned in steps of about 15 GHz by adjusting the angle of an intracavity etalon. The remaining pump light is then combined with the circulating signal light via sum-frequency generation to create around 1 W of 640 nm light. The final wavelength of the 640 nm light is set by changing the wavelength of the pump light by changing the temperature

(3 GHz/°C) of the 1064 nm seed and can be actively stabilized by modulating a PZT crystal in the fiber seed (30 MHz/V).

The UV laser system requires a narrow linewidth and long-term stability as well as wide tunability to cover the full range of wavelengths that are accessible with the OPO module. We employ a high-finesse Fabry-Perót cavity (Stable Laser Systems) made from a ultralow-expansion (ULE) glass spacer with coatings for both 689 nm and 640 nm and a free spectral range of 1.5 GHz. A small portion of the OPO output passes through an AOM and is coupled into a fiber EOM from Jenoptik, which is driven at a frequency around 1 GHz by a synthesizer from Valon (Valon 5009). We control the power of the light at the cavity by feeding back to the strength of the RF drive on the AOM. The modulation depth is set to maximize power in the first order sidebands produced by the EOM. The output of the fiber EOM is passed through a free-space EOM driven resonantly at 20 MHz to generate a PDH error signal which is fed to a DigiLock servo from Toptica. The lock employs two paths: a fast path which modulates the AOM drive frequency, and a slower path which feeds back to the PZT of the seed laser driving the pump of the OPO. The fast path does not contribute to narrowing of the laser and only serves to aid in the lock acquisition. The final linewidth of the UV is estimated to be on the order of 100 kHz based on linewidths observed in our Rydberg spectroscopy. A schematic of the UV laser system is show in Figure 2.10.

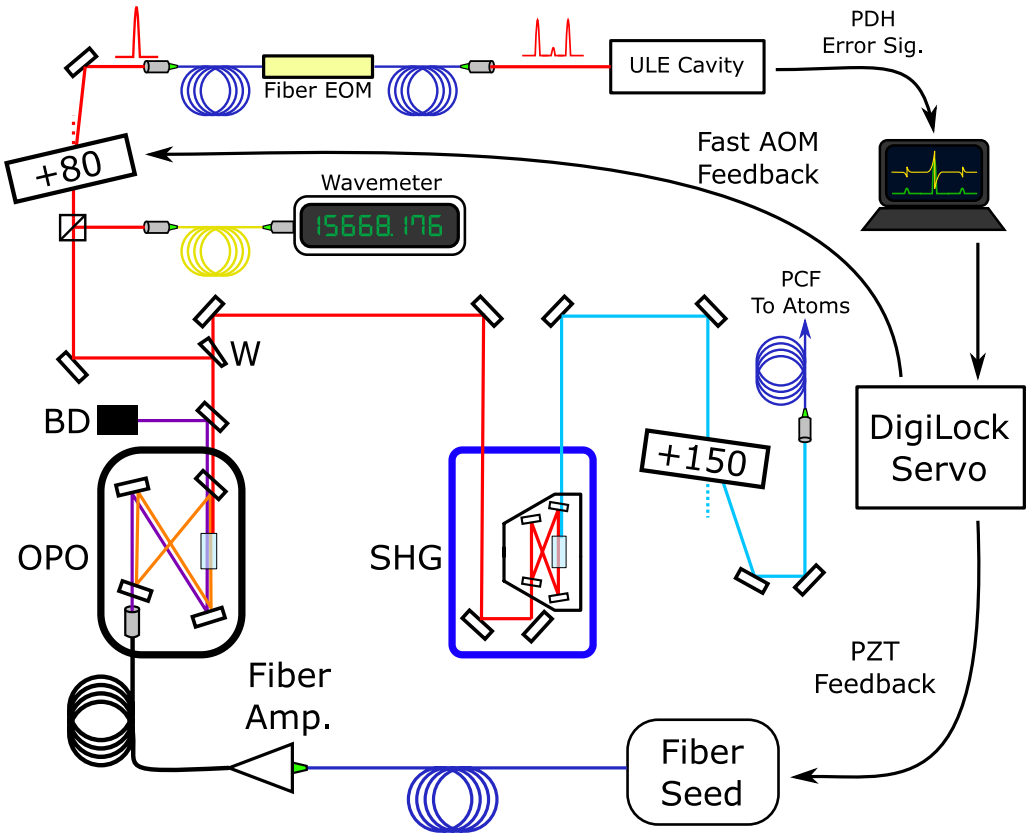

Figure 2.10 : A schematic of the UV laser system. Light from the fiber seed is coupled into a fiber amplifier that injects 8.5 W of 1064 nm light (purple) into the OPO cavity. The signal light (orange) is resonant with the cavity and is combined with the pump light to produce 640 nm light (red). A portion of the 640 nm light is coupled into a fiber EOM and sent to a ULE cavity for stabilization (see text), and the rest is coupled into a doubling cavity to produce 320 nm light (blue). The UV light is diffracted by an AOM and coupled into a photonic crystal fiber that launches the light into the chamber.

The output of the doubling cavity is sent through an AOM driven at 150 MHz for fast switching, and the diffracted order is coupled into a photonic crystal fiber

for delivery onto the atoms. Before entering the chamber, the UV light from the fiber passes through a high quality polarizer that yields a very purely horizontally-polarized UV beam that is sent to the atoms.

The frequency of the UV light is scanned by scanning the drive frequency of the 640 nm fiber EOM. The cavity resonance is fixed (modulo one free spectral range), so a change in the RF drive frequency corresponds to an equal change in the laser frequency. The direction of the laser frequency change depends on the sideband that is used for locking. If the -1 order is used to lock, a change of +100 kHz in the RF drive corresponds to a change of +200 kHz in the 320 nm frequency. If the +1 order is used, the UV laser frequency would shift -200 kHz for a change of +100 kHz in the drive frequency. Given the symmetric nature of the sidebands produced by the fiber EOM we can scan the 640 nm light in sections of ~ 750 MHz with small gaps in the achievable wavelengths where the two sidebands cross at $f_{EOM} = FSR/2$. While this issue is, in principle, a limit on which wavelengths we can reach, it has never prevented us from exciting a target Rydberg line.

The intrinsic stability of the ULE cavity spacer allows us to stabilize the Rydberg laser to the $\sim 100\,\mathrm{kHz}$ level over short time scales. The stability of the ULE spacer comes from setting the temperature of the cavity around the zero-crossing of the coefficient of thermal expansion of the ULE glass. Even near this zero, there is still residual creep of the spacer that causes the cavity to change its length very slowly. We can measure the drift of the cavity length by comparing the frequency of the 689 nm light to the $5s5p\,^3P_1$ of ^{88}Sr. We measure the $5s5p\,^3P_1$ line using saturated absorption spectroscopy in a hot vapor and record an error signal by sweeping the probe light

frequency over atomic resonance. The cavity is so stable that no additional feedback is required to keep the laser near the narrow atomic spectral feature. We can measure the position of the atomic line for many hours and can derive a drift rate of the cavity resonance as shown in Figure 2.11. The 640 nm laser and the 689 nm laser are both locked to the same cavity of length L, and therefore satisfy the same resonance condition $n\lambda_{689} = n'\lambda_{640} = L$ for integer n and n'. The frequency drift of a single laser due to a small change in the cavity spacer length is

$$\frac{df}{dt} = -\frac{c}{\lambda}\frac{1}{L}\frac{dL}{dt} \tag{2.1}$$

and by making use of the shared resonance condition the 640 nm laser drift can be derived from the measured drift of the 689 nm light using

$$\frac{df_{640}}{dt} = \frac{\lambda_{689}}{\lambda_{640}}\frac{df_{689}}{dt}. \tag{2.2}$$

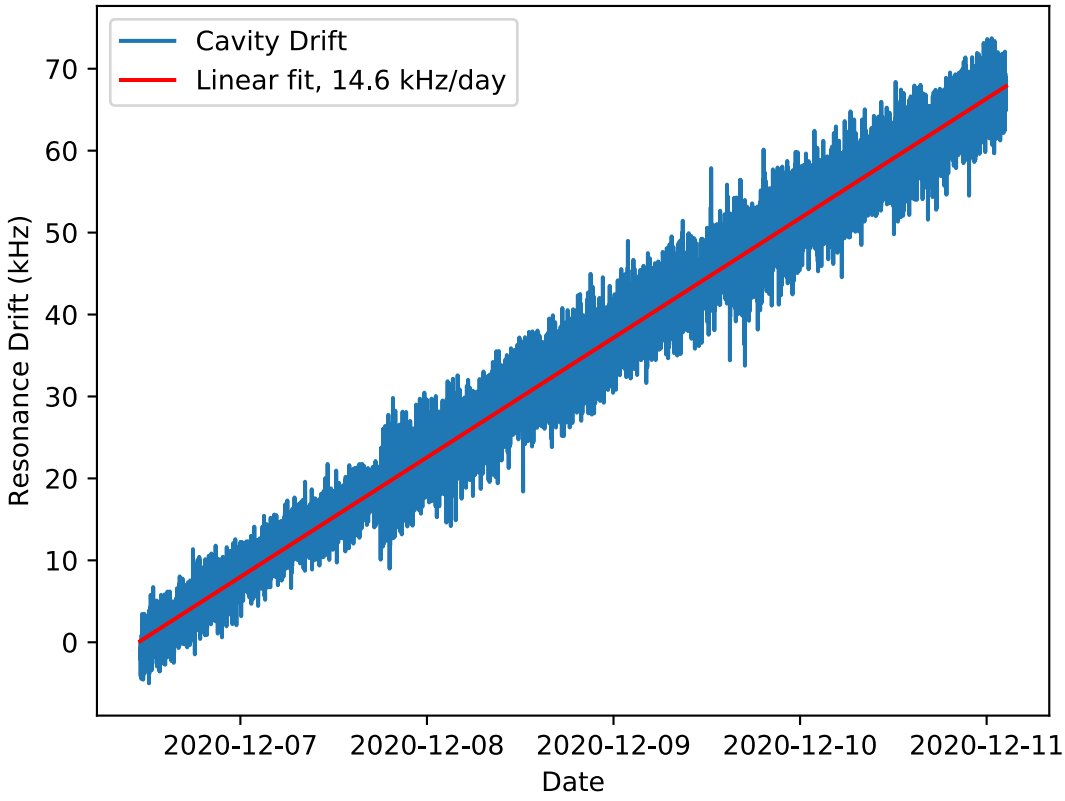

Figure 2.11 : Typical measured drift rate of the ULE cavity resonance at 689 nm determined by repeatedly measuring the position of the $5s5p\,^3P_1$ line in ^{88}Sr (see text). A linear fit to the data determines a drift rate of 14.6 kHz/day in the cavity resonance, corresponding to a change in length of 1 nm/year of the cavity spacer.

2.4.2 Electric field and charged particle detection

In order to detect the presence of Rydberg atoms in our chamber we apply directed electric field pulses to ionize them and count the resulting free electrons. The electric field pulses are generated by applying voltages to the eight electric field plates inside of our vacuum chamber. After Rydberg atoms are ionized the liberated electrons

are guided by the field toward a microchannel plate (MCP) detector where they are amplified into current pulses that are counted using a multichannel scaler (MCS). The adiabatic ionization threshold for a Rydberg state of low angular momentum ($L < 2$) is approximately $F = 1/16(n - \delta)^4$ in atomic units [63]. The atomic unit of electric field is $E_h/(a_0 e) = 5 \times 10^9\,\mathrm{V/cm}$ where E_h is the hartree (27.2 eV), a_0 is the Bohr radius (0.05 nm) and e is the charge of the electron ($6.02 \times 10^{-19}\,\mathrm{C}$) [64]. To generate electric field pulses we designed a high voltage system outlined in this section.

The pulse generation system we use is very simple. A block diagram is shown in Figure 2.12. A source of high voltage is derived from a high voltage power supply and is stored using a capacitor bank. A commercial high voltage switch is controlled with a TTL signal to switch the load between high voltage and ground. The rise time of the ramp is, in principle, limited only by the capacitance of the load and any resistance in the switch and cables connecting the output of the switch to the electric-field plates, but we add a variable resistance, R, between the switch and the load to slow down the ramp. We do this for two reasons. First, a square pulse at very high voltage would produce a very wide range of harmonics that would get picked up on all of the electronics in the lab. Slowing the ramp down low-pass filters this square pulse and reduces pickup around the lab, though some is still present. Second, there is valuable information to be gained from the distribution of electron arrival times at the MCP. Our pulse counter has a temporal resolution of 100ns, so to obtain useful information we would want the ramp to be relatively slow compared to 100ns to have good time (and therefore voltage) resolution in this distribution.

In principle this could be mitigated by removing the divider all together but it's preferable to be able to keep an eye on the ramps during the experiment. In practice, we typically operate with pulse rates of about 4 kHz with a duty cycle of 10% and do not observe any droop even with ramp amplitudes as high as 2.5 kV. All of the electronics for ramp generation are mounted on a 19-inch rack with the pulse-generation circuits in a custom built enclosure shown in Figure 2.13.

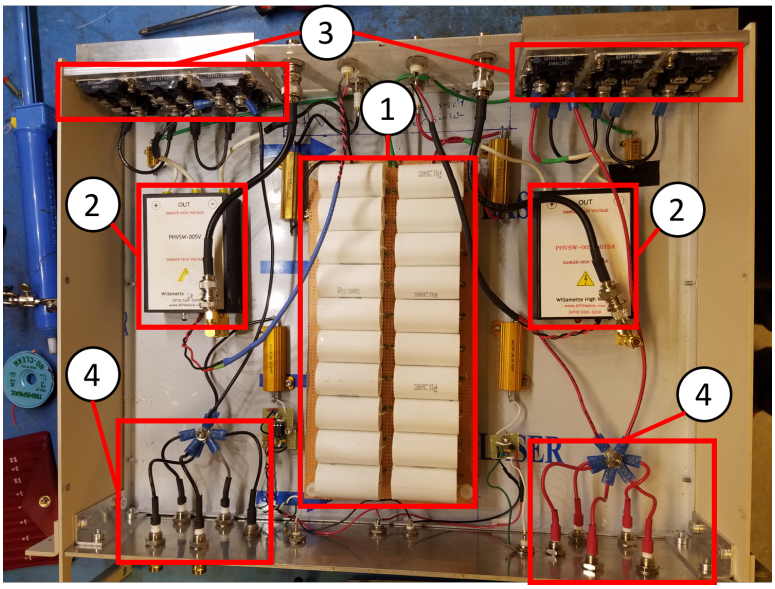

Figure 2.13 : The completed pulse box with components labeled (see text for details). 1) Capacitor bank, 2) high voltage switches, 3) the variable resistance, 4) the output to the plates.

The two polarities are powered by Glassman FC high-voltage power supplies that can supply ±6 kV at 20 mA. Each power supply is attached to a capacitor bank (labeled 1 in Figure 2.13) made of ten 0.15 μF capacitors connected in parallel.

The capacitors have a voltage limit of 3 kV and are connected to ground by a 1 MΩ resistor to ensure discharge when the supply is turned off or disconnected. The capacitors are mounted to a protoboard and soldered together. The two banks share the same ground in the center, and the outside terminals are at high voltage. The ground is connected to the earth ground by the case. The protoboard is raised off of the bottom of the box by nylon standoffs and attached with nylon 1/4"-20 screws.

Each bank is connected to a high voltage switch (Willamette High Voltage PHVSW-005V). These switches have a push-pull topology and are controlled by a TTL signal. A block diagram of the switch can be found in Appendix D. The switches are make-before-break, meaning the two terminals are shorted together for a brief time after the TTL signal changes. To prevent showing the capacitor bank ground we attach a 3 kΩ resistor between the grounded terminal and the case ground (visible in the top right of Figure 2.13. This therefore limits the speed at which the ramps will return to zero, and should be taken into consideration when deciding on experimental timings.

The output of each switch is connected through a variable resistance created by various parallel or series combinations of the resistors indicated by (3) in Figure 2.13. The network is a 2 x 3 array of 200W chassis mount resistors. The top row is three 10 kΩ resistors and the bottom row is three 1 kΩ resistors. This gives a range of possible R values from 30 kΩ to 330 Ω, or 2 decades of RC time constant. In the current setup we run with just one 10 kΩ for each ramp. The resistors are mounted to a modified heatsink (Heatsink-USA I006) with #8-32 screws and thermal paste. A picture and the dimensions of the resistors are given in Appendix D. The modifications made to the heatsinks are available in Appendix D.

The output of each resistor network is connected to five MHV bulkhead connectors and to a voltage divider made by a 100 kΩ and 100 Ω resistor, indicated by (4) in Figure 2.13. The connections are made by securing ring terminals to a nylon standoff tapped with #8-32 threads using a metal #8-32 hex screw. This helps keep points of high voltage away from the case to prevent arcing and shorting. Four of the five MHV bulkheads is connected to the vacuum chamber by a 5 foot RG-58 cable terminated with a male MHV connector on the box end and a Kings 10 kV connector on the chamber end. Each cable was carefully assembled to be the same length and therefore have the same capacitance. The length was chosen to minimize the capacitance of the cables while maintaining access to the breadboard under the table. The capacitance of each cable is 125 pF, giving a load capacitance of 500 pF for each ramp setup. We assume that the capacitance of the plates is negligible. The fifth terminal can be used to directly monitor the plate ramp using a fast high voltage scope probe such as the Tektronix 6015A. The ramp voltage can also be monitored on a normal oscilloscope using a voltage divider as shown in Figure 2.13.

Inside the vacuum chamber are 8 copper electrodes (the choice of copper is important here because the oxide that may form is also conductive, unlike that of steel) arranged in two layers of four 90 degree slices as shown in Figure 2.14. Our experiment typically runs in one of two modes. The first mode is running at low principal quantum number, roughly $n \lesssim 120$, where the stray electric fields in the chamber are small enough that they do not affect the Rydberg excitation. In this configuration Rydberg atoms are ionized by applying a negative pulse to the four plates farthest from the MCP, and a symmetric but positive pulse to the four plates closest to the

MCP. This creates a large electric field that is capable of ionizing $5s25s$ states of strontium. The maximum attainable field is limited by a short in the chamber that occurs at high voltages ($\sim$ 2.5 kV), we think that the system should be able to go up to a differential voltage of 10 kV between the positive and negative plates. When we are creating Rydberg states with $n \gtrsim 120$ we do not need large electric fields, and small stray fields can begin to interfere with Rydberg excitation. To mitigate these effects we only apply a pulsed field to the back plates, while applying small DC voltages ($\pm$10V) to each of the front plates. We have performed experiments on Rydberg atoms with principal quantum number as high as $n = 150$ using this system [65].

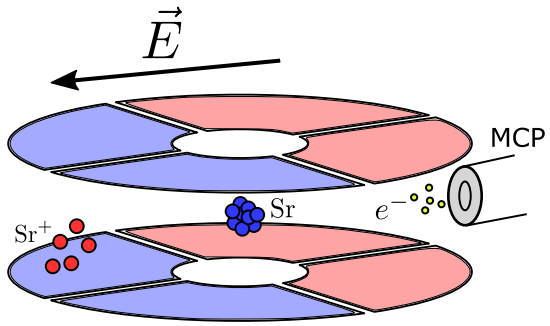

Figure 2.14 : A schematic diagram showing the configuration of the electric field plates and MCP detector. Negative (blue) and positive (red) voltages are applied to the electric field plates in the configuration shown producing an electric field that ionizes any Rydberg atoms and guides the liberated electrons to the microchannel plate (MCP) detector. Sr^+ ions are also produced, but are not detected.

Once the electrons are liberated from their parent nucleus they are sent onto our microchannel plate detector. We use a photonis MINITOF model MCP. Once the

MCP pulses are generated we send them into an SRS SR-445 preamplifier which has a 50 Ω input impedance and a gain of 5. We then take the output of the preamp and feed it into a small RF amplifier (Minicircuits ZFL-500LN) which AC couples the signal and provides additional amplification. From there, the signals are sent over a BNC cable to the multi-channel scaler counter in our computer.

The scaler we use is a MCA-3 from Fastcomtec GmbH. It provides 100 ns timing resolution which gives us the ability to resolve different Rydberg states by their time-of-flight signature as shown in [14, 65, 66].

2.5 Spin polarization

For experiments that require samples of fermionic ^{87}Sr, it is useful to be able to control the distribution of the population of the ten m_F levels in the $I = 9/2$ $5s^2\,{}^1S_0$ ground state. After the narrow-line MOT phase, the m_F populations are approximately equally populated, and optical pumping can be used to move population around. For the experiments relevant to this work we desire either an unpolarized sample where each m_F level is populated equally, or a spin-polarized sample where, ideally, all of the atoms in the sample are in the $m_F = 9/2$ state.

To this end, we have set up a laser system that uses circularly polarized 689 nm light to optically pump atoms into the $m_F = 9/2$ state using the $5s^2\,{}^1S_0 \rightarrow 5s5p\,{}^3P_1$ intercombination transition. The pumping light is tuned to the $F = 9/2$ hyperfine manifold of the $5s5p\,{}^3P_1$ state, and the population of each m_F state can be probed using the $F = 11/2$ $5s5p\,{}^3P_1$ transition. We generate the pumping light

using a 689 nm laser diode that is injection locked at a frequency 82 MHz red detuned from the $5s^2\,{}^1S_0 \rightarrow 5s5p\,{}^3P_1$ transition of ^{88}Sr. The light is shifted to the $F = 9/2 \rightarrow F = 9/2$ intercombination transition using a 303 MHz AOM and coupled into a fiber. The output is collimated to a 4 mm diameter beam [54] and combined with the $F = 9/2 \rightarrow F = 11/2$ spectroscopy beam and passes through a quarter-wave plate before entering the chamber along the quantization axis set by a bias magnetic field. A schematic of the laser system is shown in Figure 2.15 and the relevant energy levels are shown in Figure 2.16.

To perform the optical pumping process we apply a 7.6 G bias magnetic field which induces a Zeeman splitting in the $F = 9/2$ $5s5p\,{}^3P_1$ manifold of $\sim$ 650 kHz between adjacent m_F levels. The magnetic moment of the ground state is negligible, so the ground state is approximately unshifted at our level of resolution. With this splitting we can address each m_F level individually, and we apply a series of σ^+ polarized laser pulses red-detuned about 50 kHz from each $m_F \rightarrow m_F + 1$ transition. The red-detuning of the pulses is chosen to avoid heating of the sample. The frequency of each pulse is determined by the RF frequency driving the AOM that controls the beam before the fiber. We drive the AOM using a Novatech 409-B synthesizer that can store a table of ten frequencies and step through the table using a TTL pulse from the experimental control program. After the optical pumping is complete, we typically reduce the magnetic field to about 1 G to maintain a quantization axis. The spin polarization is maintained

To verify the fidelity of the optical pumping process we can measure the populations of each m_F level spectroscopically. This can be done using various methods

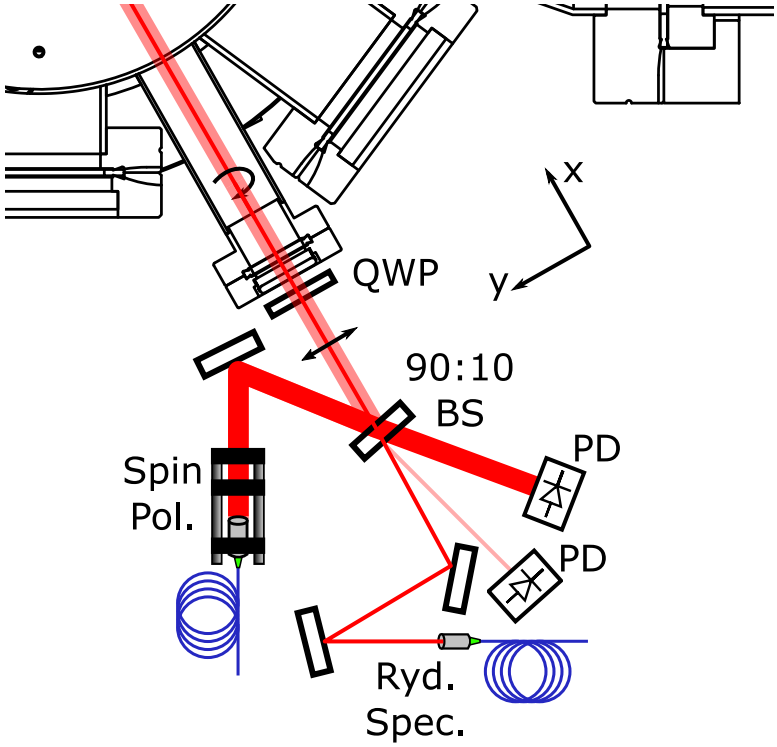

Figure 2.15 : A schematic of the spin polarization laser system. The large spin-polarization beam is emitted from a fiber collimmator and passes through a high quality polarizer. The smaller Rydberg spectroscopy beam comes from another collimator. The beams are combined using a 90/10 T/R beam splitter, which sends a smaller portion of the spin polarization beam into the chamber and transmits the spectroscopy beam. The reflected (transmitted) beams are used to monitor the power in the spectroscopy (spin polarization) beams using photodiodes (PD). Once combined, the two beams pass through a $\lambda/4$ plate (QWP) and are circularly polarized before entering the vacuum chamber through a mini viewport.

including shelving spectroscopy or an optical Stern-Gerlach method [67]. These methods rely on imaging the atom cloud to count the populations in the various m_F levels. In our system the minimum number of atoms that can be reliably counted

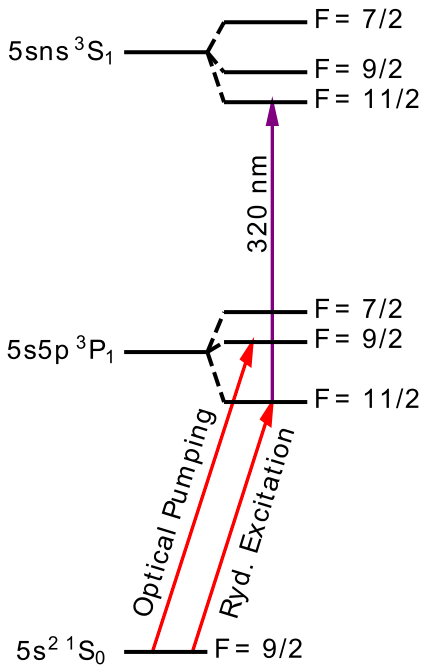

Figure 2.16 : The relevant hyperfine structure of ^{87}Sr. The optical pumping laser drives the $F = 9/2 \rightarrow F = 9/2$, and the two-photon Rydberg excitation drives $F = 9/2 \rightarrow F = 11/2 \rightarrow F = 11/2$ to the $5sns\,^3S_1$ Rydberg state.

with absorption imaging techniques is between $5 - 10 \times 10^3$, which would lead to significant uncertainty in the real populations of states that have been optically pumped. To avoid this, we can use a Zeeman-split Rydberg line to determine the relative populations of the m_F levels using the high sensitivity and dynamic range of the charged particle detection system. Two-photon excitation spectra are shown in Figure 2.18 for polarized and unpolarized samples excited using two linearly polarized photons. We can fit the spectrum to extract the relative populations of each m_F level from the amplitudes of each Zeeman peak.

To extract the population of each m_F level from the spectra in Figure 2.18 we must determine the relative excitation rate for each transition from lower m_F state to upper m_F state. The two-photon transition rate is given by the square of the two-photon Rabi frequency, Ω,

$$\Omega = \frac{\Omega_{g,i}\Omega_{i,r}}{4\Delta}. \tag{2.4}$$

Where $\Omega_{g,i}$ and $\Omega_{i,r}$ are the single-photon Rabi frequencies for the $5s^2\,{}^1S_0 \rightarrow 5s5p\,{}^3P_1$ and $5s5p\,{}^3P_1 \rightarrow 5sns\,{}^3S_1$ transitions respectively, and Δ is the detuning of the 689 nm photon from the $5s5p\,{}^3P_1$ state. The single photon Rabi frequency is proportional to the product of the square root of the laser intensity and the dipole matrix element corresponding to the transition, i.e.

$$\Omega_{i,j} \propto \sqrt{I}\langle F_i\, m_{F,i}|er_q|F_j\, m_{F,j}\rangle \tag{2.5}$$

The matrix elements can be expressed using the Wigner-Eckart theorem [52]

$$\langle F_i\, m_{F,i}|er_q|F_j\, m_{F,j}\rangle = (-1)^{F_i - m_{F,i}} \begin{pmatrix} F_i & 1 & F_j \\ -m_{F,i} & q & m_{F,j} \end{pmatrix} \langle F_i||e\mathbf{r}||F_j\rangle \tag{2.6}$$

Where the bracketed quantity is a Wigner $3j$-symbol and the double-barred matrix element is a reduced matrix element that does not depend on the projection of F and is therefore the same for all initial and final m states. The projection of $\mathbf{r}$ is given by $q = +1, 0, -1$ for σ^+, π, σ^- laser polarizations defined with respect to the quantization axis defined by the bias magnetic field. When obtaining spectra we keep the laser intensities and intermediate detuning constant. Therefore, the relative transition rate, $\mathcal{A}^{(q,p)}_{m_F}$, for a given initial m_F and laser polarizations p and q is given

by a product of $3j$-symbols, i.e.,

$$\mathcal{A}_{m_F}^{(q,p)} \sim \begin{pmatrix} 9/2 & 1 & 11/2 \\ m_F & q & -(m_F+q) \end{pmatrix}^2 \begin{pmatrix} 11/2 & 1 & 11/2 \\ (m_F+q) & p & -(m_F+q+p) \end{pmatrix}^2 \tag{2.7}$$

with polarizations q and p of the 689 nm and 320 nm photons respectively. Relevant values of $\mathcal{A}_{m_F}^{(q,p)}$ are shown in Figure 2.17. The total observed spectrum in a bias field B with laser polarizations q and p is given by

$$\mathcal{S}(\omega) = \sum_{m_F=-9/2}^{9/2} x_{m_F} \mathcal{A}_{m_F}^{(q,p)} \, \delta(\hbar\omega + \hbar\omega_{689} - E_n - \mu_B g_F B(m_F+q+p)) \tag{2.8}$$

where ω is the frequency of the 320 nm photon that is scanned, ω_{689} is the fixed frequency of the 689 photon, x_{m_F} is the fraction of population in each magnetic sublevel, and $\mu_B g_F B(m_F+q+p)$ is the Zeeman shift of the upper state from the bare Rydberg state energy E_n. The g-factor of the Rydberg state is 4/11, which corresponds to a splitting of 500 kHz between adjacent magnetic sublevels in a field of 1 G, and we neglect the Zeeman shift of the intermediate state since it is small compared to the size of the two-photon detuning.

Using Equation 2.8 we can take a Rydberg spectrum in a polarized or unpolarized sample and extract the relative populations of each initial m_F level. As shown in Figure 2.17 for combinations of circular and linear polarized excitation beams there is a bias toward one half of m_F levels that would make our sensitivity to populations in the other m_F levels very low. These combinations are useful for exciting to Rydberg states because any off-resonant scattering of the σ^+ light only serves to preserve the spin-polarization of the sample, but are not very good for probing the fidelity of the spin polarization. To probe the quality of the spin polarization of the sample we use the $\pi + \pi$ combination of excitation beams.

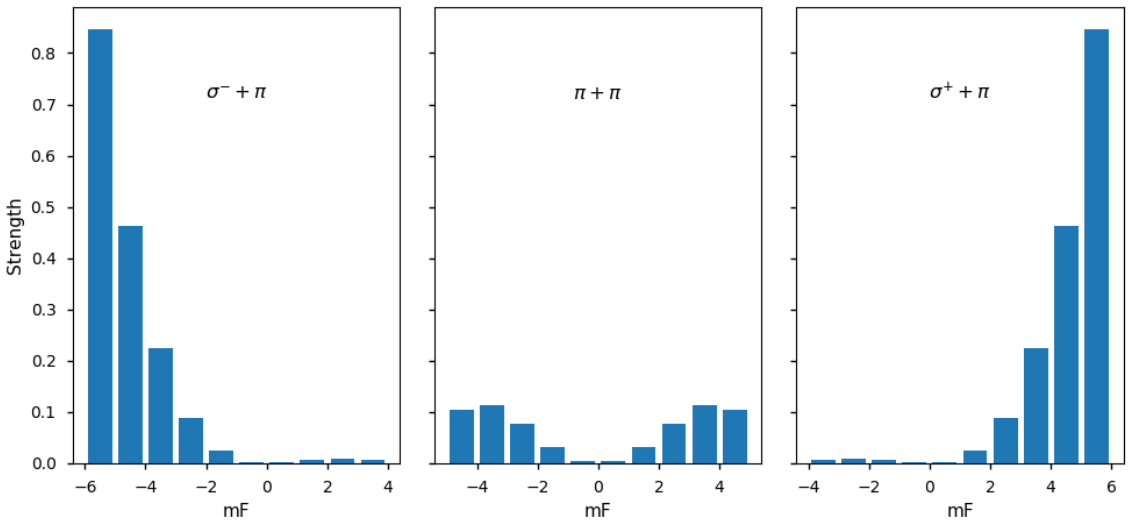

Figure 2.17 : $\mathcal{A}_{m_F}^{(q,p)}$ for various combinations of 689 nm and 320 nm polarizations. For equal populations of the initial m_F levels the spectrum reflects the Typically Rydberg excitation of ^{87}Sr is performed using $\sigma^+ + \pi$, and the fidelity of the spin-polarization of the sample is probed using $\pi + \pi$.

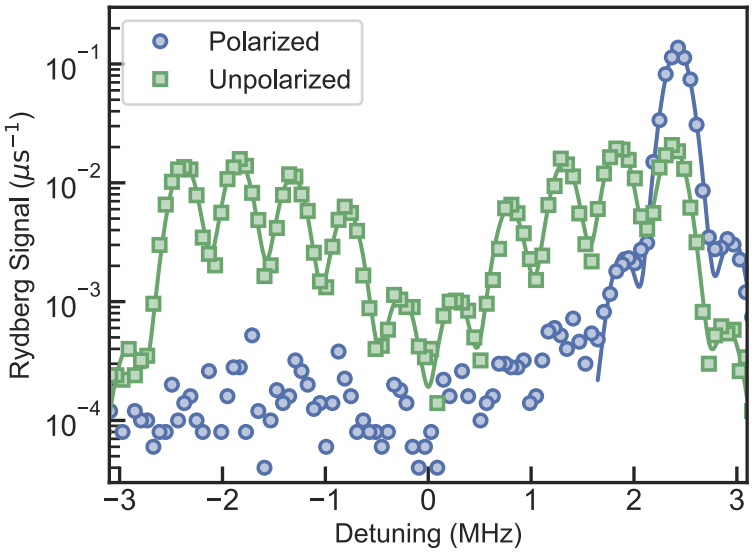

Figure 2.18 : Spectra for excitation to the atomic $5s34s\,^3S_1$ state for spin-polarized (cirles) and unpolarized (squares) gases of ^{87}Sr in a magnetic field of 1 G using $\pi+\pi$ polarized excitation beams. The spectra are fitted to Equation 2.8 to extract the populations in each m_F level.

We measure the fidelity of the spin-polarization procedure by trapping a sample of ^{87}Sr and performing the pulse sequence described above. Following the polarization pulses we apply a $\pi+\pi$ polarized excitation pulse in a magnetic field of about 1 G (the same field that is kept on during typical experiments) and scan the energy of the UV photon to obtain a spectrum as shown in Figure 2.18. From these spectra we can extract the populations x_{m_F} by fitting to Equation 2.8. These values are shown in Figure 2.19 and give a lower bound of 90% spin-polarization fidelity.

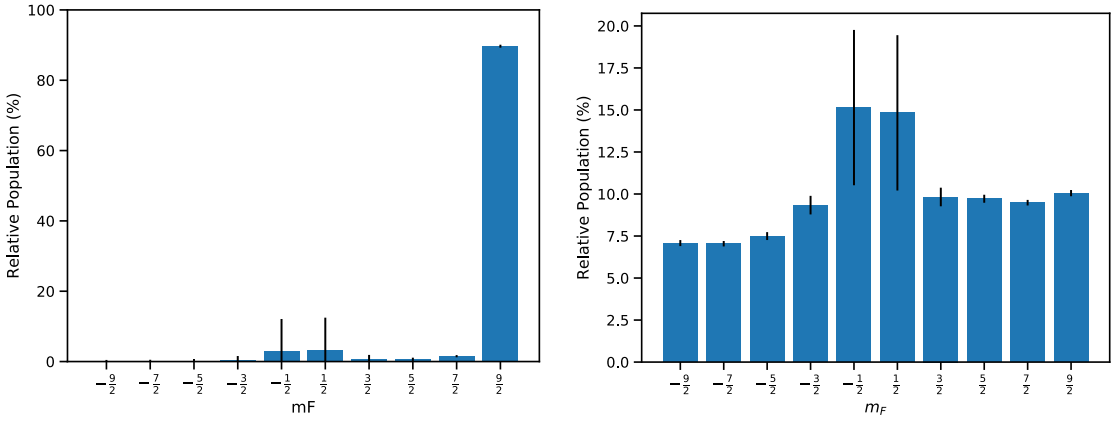

Figure 2.19 : Extracted m_F populations from fitting spectra shown in Figure 2.18 to Equation 2.8. Left: Populations in the polarized case. Right: populations in the unpolarized case. The error bars indicate the uncertainty in the fit for each population.

Chapter 3

Rydberg Molecule Excitation Spectrum

In the introduction we motivated the connection between the pair-correlation function, $g^{(2)}(R)$, and the excitation of RM's in the $\nu = 0$ vibrational state. The highly localized wave packet in the outermost well requires that two particles be separated by roughly $R_n \sim 2(n - \delta_\ell)^2$ and therefore the molecular excitation rate depends on the relative probability of finding two particles at that separation. In this chapter we will derive the connection between $g^{(2)}(R)$ and RM's in more detail, and discuss the other factors that must be taken into account to extract $g^{(2)}(R)$ from the RM spectra measured in our experiment.

The per-atom excitation rate of RM's can be considered using Fermi's golden rule,

$$\Gamma_{i\to f} \propto |\langle i|\hat{T}|f\rangle|^2 \delta(E_i - E_f). \tag{3.1}$$

The initial ($|i\rangle$) and final ($|f\rangle$) states under consideration have both spatial and electronic components. The transition operator, $\hat{T}$, is the two-photon transition operator. The initial state is comprised of a colliding pair of atoms, both in the ground electronic state, with relative momentum $\vec{k}$. The final state is a rotating RM state with angular momentum Λ and projection M_Λ with one atom in the Rydberg state and one remaining in the ground state. Therefore the transition rate for a given

initial and final state is given by

$$\Gamma_{\vec{k}\to n,\Lambda,M_\Lambda}(\omega) \propto \Omega_n^2 |\mathcal{F}_{n,\Lambda,M_\Lambda}(\vec{k})|^2 \delta(\hbar\omega + E_{\vec{k}} - E_{n,\Lambda}) \tag{3.2}$$

Where Ω_n is the two-photon Rabi frequency defined in Section 2.5, $\mathcal{F}_{n,\Lambda,M_\Lambda}(\vec{k}) = \langle \vec{k}|n,\Lambda,M_\Lambda\rangle$ is the Franck-Condon (FC) overlap between the initial and final spatial wavefunctions, and ω is the laser detuning from the $\nu = 0$ RM resonance. The initial and final energies are $E_i = \hbar\omega + E_{\vec{k}} = \hbar\omega + \hbar^2k^2/2\mu$ and $E_f = E_{n,\Lambda} = \hbar^2\Lambda(\Lambda+1)/(\mu R_n^2)$.

3.1 Derivation of the Rydberg molecule lineshape

To calculate the total rate we must sum over final states $|\Lambda, M_\Lambda\rangle$ and average over initial states $|\vec{k}\rangle$. The total lineshape of the Rydberg molecule line is given by a sum of contributions from each final rotational state $|\Lambda, M_\Lambda\rangle$ averaged over relative momentum wavevector $\vec{k}$ [68],

$$f_n(\omega) = C_n \sum_{\Lambda} \sum_{M=-\Lambda}^{\Lambda} \left(\frac{\hbar^2}{2\pi\mu k_B T}\right)^{3/2} \int d^3k\, e^{-\frac{\hbar^2k^2}{(2\mu k_B T)}} |\mathcal{F}_{n,\Lambda,M}(\vec{k})|^2 \mathcal{L}_{n,\Lambda}(\vec{k},\omega). \tag{3.3}$$

Where C_n contains the two-photon Rabi frequency and other calibration factors that are independent of isotope and n. The delta function in Equation 3.2 is replaced by a lineshape function, $\mathcal{L}_{n,\Lambda}$, with unit integral, which is a Lorentzian,

$$\mathcal{L}_{n,\Lambda}(\vec{k},\omega) = \frac{1}{\pi} \frac{\Gamma/2}{(\hbar\omega + \hbar^2k^2/(2\mu) - E_{n,\Lambda})^2/\hbar^2 + \Gamma^2/4}, \tag{3.4}$$

with full-width at half-maximum Γ that is largely determined by the 320 nm laser linewidth, about 100 kHz. The lineshape function is centered at $E_{n,\Lambda} = \hbar^2\Lambda(\Lambda+1)/\mu R_n^2$.

$\mathcal{F}_{n,\Lambda,M}(\vec{k})$ is the Franck-Condon overlap between the initial scattering state and the final molecular wavefunction. The full form of the Franck-Condon factor is

$$\mathcal{F}_{n,\Lambda,M}(\vec{k}) = \langle \vec{k}|n,\Lambda,M_\Lambda\rangle = \int d^3R\, \mathcal{R}_n(R) Y_\Lambda^M(\hat{R}) \chi_{\vec{k}}(\vec{R}). \tag{3.5}$$

For a RM in the $\nu = 0$ vibrational state (see Figure 1.3) the radial part of the molecular wavefunction, $\mathcal{R}_n(R)$, can be approximated as a gaussian centered at $R_n = 1.8(n-\delta_\ell)^2$ with width σ,

$$\mathcal{R}_n(R) = \frac{(4\pi\sigma^2)^{1/4}}{R} \frac{e^{-(R-R_n)^2/(2\sigma^2)}}{\sqrt{2\pi}\sigma} \approx \frac{(4\pi\sigma^2)^{1/4}}{R}\delta(R-R_n). \tag{3.6}$$

In the limit of $\sigma \ll R_n$, which is the case for a RM in the range of n under consideration here, we can approximate the gaussian as a delta-function. Inserting this into the Franck-Condon factor gives

$$\mathcal{F}_{n,\Lambda,M}(\vec{k}) = \int_{\Omega_R} d\Omega_R \int_0^\infty dR\, R(4\pi\sigma^2)^{1/4}\delta(R-R_n) Y_\Lambda^M(\hat{R})\chi_{\vec{k}}(\vec{R}) \tag{3.7}$$

Now consider $\chi_{\vec{k}}(\vec{R})$, which is generally given as the superposition of an incoming plane wave and a scattered spherical wave modulated by the angle-dependent scattering amplitude $f(\theta)$ with appropriate parity under particle exchange

$$\chi_{\vec{k}}^{\pm}(\vec{R}) = \frac{1}{\sqrt{2}}\left(e^{i\vec{k}\cdot\vec{R}} \pm e^{-i\vec{k}\cdot\vec{R}}\right) + \frac{f(\theta)\pm f(\pi-\theta)}{\sqrt{2}}\frac{e^{ikR}}{R}. \tag{3.8}$$

The angle θ in the scattering amplitude is the angle between $\vec{k}$ and $\vec{R}$. $\chi_{\vec{k}}^{\pm}(\vec{R})$ can be expanded in partial waves as

$$\chi_{\vec{k}}^{\pm}(\vec{R}) = \sqrt{2}\sum_\ell \sum_{m=-\ell}^{m} \mathcal{P}_\ell^{\pm}\left[4\pi Y_\ell^m(\hat{k})^* Y_\ell^m(\hat{R}) i^\ell j_\ell(kR) + \delta_{m,0} f_\ell Y_\ell^0(\theta)\frac{e^{ikR}}{R}\right], \tag{3.9}$$

where $\mathcal{P}_\ell^\pm = \frac{1}{2}\left(1 \pm (-1)^\ell\right)$ and the scattering amplitude has been decomposed into spherical harmonics with $m = 0$ because of its lack of dependence on the azimuthal angle, i.e. $f(\theta) = \sum_\ell f_\ell Y_\ell^0(\theta)$. In the s-wave limit (and neglecting phase shifts of higher partial waves) only the $\ell = 0$ channel contributes leaving $f(\theta) = f_0 Y_0^0(\theta) = e^{i\delta}\sin(\delta)/k$, where $\delta = -ka$ is the momentum dependent scattering phase shift, and all other $f_{\ell>0} = 0$. Now we can put all of the pieces together and write $\chi_{\vec{k}}^\pm(\vec{R})$ in terms of spherical coordinates

$$\chi_{\vec{k}}^\pm(\vec{R}) = \sqrt{2}\sum_\ell \sum_{m=-\ell}^{m} \mathcal{P}_\ell^\pm \left[4\pi Y_\ell^m(\hat{k})^* Y_\ell^m(\hat{R}) i^\ell j_\ell(kR) + \delta_{m,0}\delta_{\ell,0}\frac{e^{ikR+i\delta}\sin(\delta)}{kR}\right], \tag{3.10}$$

With both components of the integrand determined we can now consider the integral for $\mathcal{F}_{n,\Lambda,M}(\vec{k})$ in two parts, a radial portion and an angular portion.

$$\mathcal{F}_{n,\Lambda,M}^\pm(\vec{k}) = \sqrt{2}\sum_{\ell,m}\int_0^\infty dR \int_{\Omega_R} d\Omega_R$$
$$R(4\pi\sigma^2)^{1/4}\delta(R-R_n)Y_\Lambda^M(\hat{R})^*\mathcal{P}_\ell^\pm\left(4\pi Y_\ell^m(\hat{k})^* Y_\ell^m(\hat{R}) i^\ell j_\ell(kR) + \frac{e^{ikR+i\delta}\sin(\delta)}{kR}\delta_{\ell,0}\delta_{m,0}\right) \tag{3.11}$$

We can now make use of the orthonormality of the spherical harmonics

$$\int_{\Omega_q} d\Omega_q\, Y_{\ell'}^{m'}(\hat{q})^* Y_\ell^m(\hat{q}) = \delta_{\ell,\ell'}\delta_{m,m'}$$

and integrate over R

$$\mathcal{F}_{n,\Lambda,M}^\pm(\vec{k}) = R_n(4\pi\sigma^2)^{1/4}\sqrt{2}\mathcal{P}_\Lambda^\pm\left(4\pi Y_\Lambda^M(\hat{k})^* i^\Lambda j_\Lambda(kR_n) + \sqrt{4\pi}\frac{e^{ikR_n+i\delta}\sin(\delta)}{kR_n}\delta_{\Lambda,0}\right) \tag{3.12}$$

Plugging in $\mathcal{F}_{n,\Lambda,M}(\vec{k})$ into Equation 3.3 gives

$$f_n(\omega) = C_n \sum_{\pm} \frac{1}{2}\mathcal{D}_{\pm} 4R_n^2 \sigma\sqrt{\pi}\frac{\lambda_{dB}^3}{2\sqrt{2}\pi^3}\int_{\Omega_k} d\Omega_k \int_0^\infty dk k^2\, e^{-\lambda_{dB}^2 k^2/(2\pi)} \ldots$$
$$16\pi^2\left[\mathcal{P}_0^{\pm}\left(2j_0(kR_n)\frac{\cos(kR_n+\delta)\sin(\delta)}{kR_n} + \frac{\sin^2(\delta)}{k^2R_n^2}\right)\mathcal{L}_{n,0}(\vec{k},\omega) + \ldots\right.$$
$$\left.\sum_{\Lambda}\sum_{M=-\Lambda}^{\Lambda}\mathcal{P}_{\Lambda}^{\pm} j_{\Lambda}(kR_n)^2 |Y_{\Lambda}^M(\hat{k})|^2 \mathcal{L}_{n,\Lambda}(k,\omega)\right]. \quad (3.13)$$

Here we have introduced a sum over symmetric (+) and anti-symmetric (−) configurations and a weighting function $\mathcal{D}_{\pm}$. For identical bosons $\mathcal{D}_+ = 1$ and $\mathcal{D}_- = 0$; for fermions $\mathcal{D}_+ = 0$ and $\mathcal{D}_- = 1$; and for distinguishable particles $\mathcal{D}_+ = \mathcal{D}_- = 1$. The additional factor of $1/2$ prevents double counting. Performing the angular integration gives

$$f_n(\omega) = C_n \sum_{\pm} \frac{1}{2}\mathcal{D}_{\pm} 4R_n^2 \sigma\sqrt{\pi}\frac{\lambda_{dB}^3}{2\sqrt{2}\pi^3}\int_0^\infty dk\, k^2 e^{-\lambda_{dB}^2 k^2/(2\pi)} \ldots$$
$$16\pi^2\left[\mathcal{P}_0^{\pm}\left(2j_0(kR_n)\frac{\cos(kR_n+\delta)\sin(\delta)}{kR_n} + \frac{\sin^2(\delta)}{k^2R_n^2}\right)\mathcal{L}_{n,0}(\vec{k},\omega) + \ldots\right.$$
$$\left.\sum_{\Lambda}(2\Lambda+1)\mathcal{P}_{\Lambda}^{\pm} j_{\Lambda}(kR_n)^2 \mathcal{L}_{n,\Lambda}(\vec{k},\omega)\right] \quad (3.14)$$

This is the full expression of the spectrum, and to calculate the lineshape we need to use numerical integration methods. In Figure 3.1 we show the spectra for four species of RMs ($n = 30$): homonuclear ^{84}Sr, spin-polarized homonuclear ^{87}Sr, heteronuclear $^{84}\mathrm{Sr} + {}^{88}\mathrm{Sr}$ and homonuclear ^{86}Sr. We include the interactions parameterized by the scattering lengths given in Table 1.1.

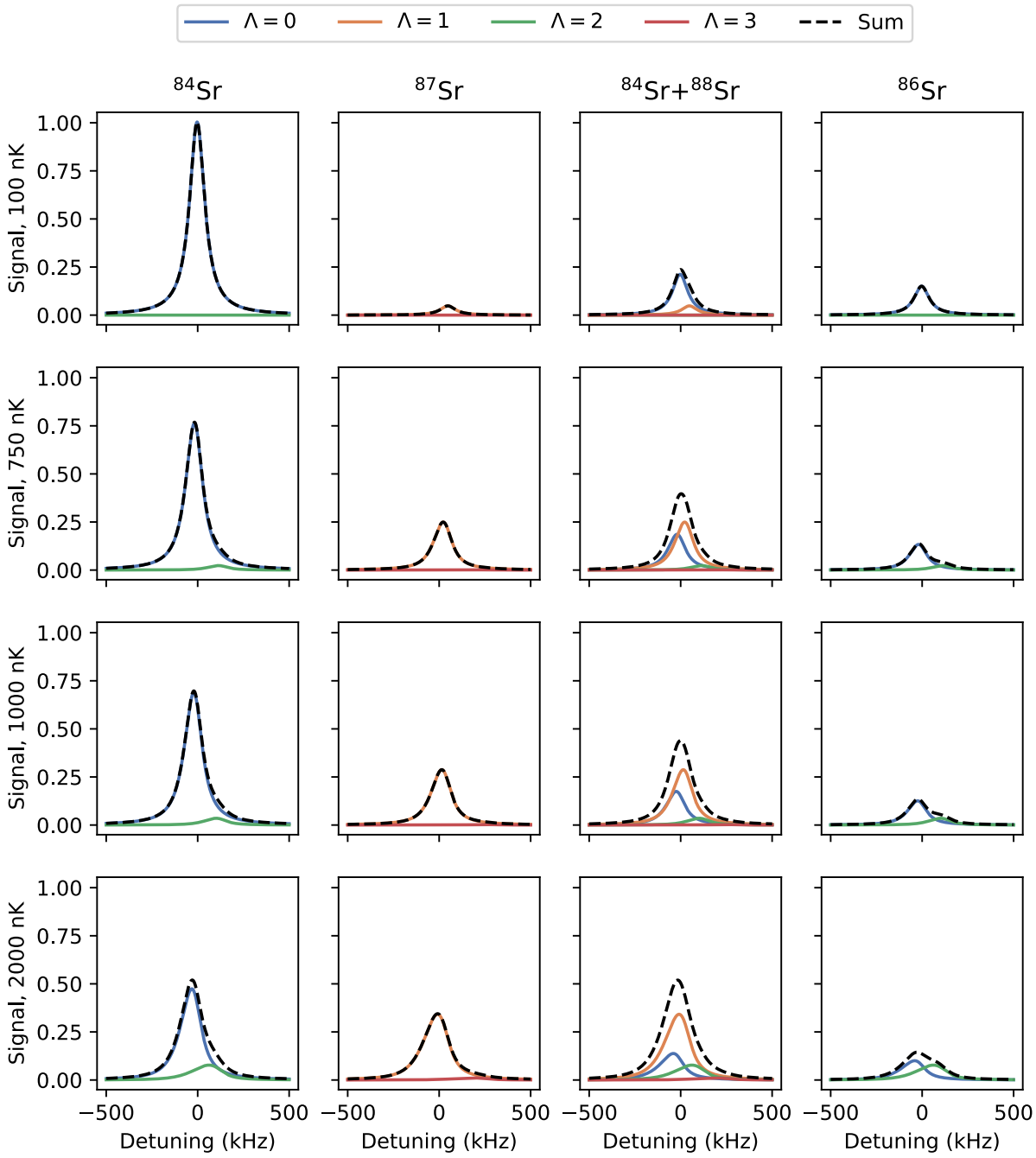

Figure 3.1 : Predicted $\nu = 0$ RM spectra for various isotopic combinations at temperatures ranging from 100 nK to 2 μK at $n = 30$. The contribution from each partial wave, Λ, is shown with colored lines and the total spectrum is shown with a dashed black line. A more detailed discussion of the spectra is found in the text.

There is a lot of information in Figure 3.1. First, consider the weakly interacting spectra in the first two columns. As temperature increases we observe a broadening toward red detuning and an increase in the contribution from higher Λ channels. We also observe an increase (decrease) in the signal amplitude for ^{84}Sr (^{87}Sr) as temperature decreases. This change with temperature is directly related to the effect of particle statistics, and will be discussed in the next section.

In the third and fourth columns of Figure 3.1 we calculated the RM spectrum for gases with stronger interactions. The contrast between ^{84}Sr and ^{86}Sr is very clear. Due to the larger s-wave scattering length of ^{86}Sr the $\Lambda = 0$ channel is strongly suppressed at this principal quantum number. At higher temperatures, the $\Lambda = 2$ channel is almost equally strong as the $\Lambda = 0$ channel, and leads to a bimodal lineshape in contrast with the relatively symmetric lineshape of ^{84}Sr.

The spectra for the strongly interacting heteronuclear mixture of ^{84}Sr and ^{88}Sr are also quite striking. The spectrum is dominated by the $\Lambda = 1$ channel at all but the lowest temperatures due to the extreme suppression of the $\Lambda = 0$ channel by the very large s-wave interactions. The lineshape remains apparently symmetric, however, in contrast with ^{86}Sr. This is due to the larger number of partial waves that are permitted to participate in the RM excitation because of the lack of symmetry under particle exchange. This explains the apparently symmetric lines observed in heteronuclear mixtures in Chapter 5.

3.2 Relationship of RM excitation to $g^{(2)}(R)$

We claimed earlier that the molecular excitation rate is directly related to $g^{(2)}(R)$. In the experiments presented in this thesis the interparticle interactions are weak, so we take the scattering phase shift $\delta = 0$ which simplifies Equation 3.14. To obtain

the total excitation strength from the spectrum we must integrate over frequency. Using the fact that $\mathcal{L}_{n,\Lambda}$ has unit integral and two sum rules for spherical Bessel functions [69] the excitation strength can be written as

$$\mathcal{S}_n = \int d\omega f_n(\omega) = C_n \sum_{\pm} \frac{1}{2}\mathcal{D}_{\pm} 4R_n^2 \sigma\sqrt{\pi} \frac{\lambda_{dB}^3}{2\sqrt{2}\pi^3} \int_0^\infty dk k^2 \, e^{-\lambda_{dB}^2 k^2/(2\pi)} 16\pi^2 \left(1 \pm \frac{\sin(2kR_n)}{2kR_n}\right), \tag{3.15}$$

and evaluating the integral over k yields

$$\mathcal{S}_n = C_n 4R_n^2 \sigma\sqrt{\pi} \sum_{\pm} \frac{1}{2}\mathcal{D}_{\pm} 4\pi(1 \pm e^{-2\pi R_n^2/\lambda_{dB}^2}) \equiv C_n 4R_n^2 \sigma\sqrt{\pi} \sum_{\pm} \frac{1}{2}\mathcal{D}_{\pm} 4\pi g_{\pm}^{(2)}(R_n). \tag{3.16}$$

Here we can see that $g_{\pm}^{(2)}(R)$ has been identified with the expression for $g^{(2)}(R)$ that was presented in the introduction of this thesis, and for distinguishable particles the R dependence of the pair correlation identically cancels. Explicitly, the integrated RM spectrum is a product of various n-dependent and experimental factors and the pair correlation function for a thermal gas. This connection is not unexpected. The RM state is highly localized, which creates a very specific final state in R. The excitation rate is a sum over final states and an average over initial states, and given the highly localized nature of the final state we are left with a thermal average over initial colliding states at R_n, which is essentially $g^{(2)}(R)$. Therefore, we can see that the molecular excitation rate is directly related to $g^{(2)}(R_n)$ as introduced in Section 1.4. We can again examine the contribution from each partial wave to $g^{(2)}(R)$, as shown in Figure 3.2.

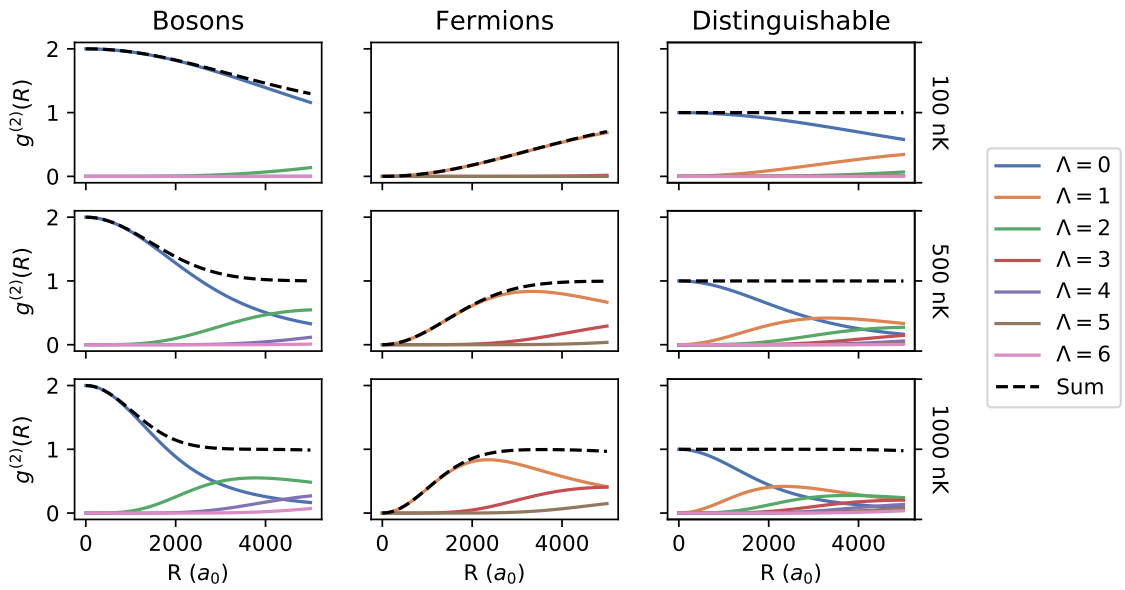

Figure 3.2 : The contribution of each partial wave Λ to $g^{(2)}(R)$ for bosons, fermions and distinguishable particles with mass similar to Sr at temperatures of 100 nK, 500 nK, and 1 μK.

3.3 Corrections due to density

In the previous section we derived the molecular excitation rate per atom pair using Fermi's golden rule.

In our experiment there are N atoms with temperature T in the optical dipole trap. The atoms have a density distribution $n(\vec{r})$ given by

$$n(\vec{r}) = n_0 \exp\left(\frac{-V(\vec{r})}{k_B T}\right). \tag{3.17}$$

The ODT is approximately harmonic, so we can rewrite the density in terms of the trap frequencies

$$n(r) = n_0 \exp\left(\frac{-m\bar{\omega}^2 r^2}{2k_B T}\right) \tag{3.18}$$

Using the fact that the total number N is equal to the integral of the density distribution over space we can define the peak density n_0 as N/V_{eff} where the effective volume V_{eff} is

$$V_{eff} = \left(\frac{2\pi k_B T}{m\bar{\omega}^2}\right)^{3/2}. \tag{3.19}$$

The local excitation rate for a homonuclear RM at position r is equal to the pair density, $n(r)^2$, times the per-pair rate, κ, derived in the previous section. To obtain the total molecular excitation rate we integrate over the trap:

$$\dot{N} \sim \kappa \int d^3r n(r)^2 = \kappa\, n_0^2 \left(\frac{\pi k_B T}{m\bar{\omega}^2}\right)^{3/2} \stackrel{\text{def}}{=} \kappa\, n_0^2 V_2. \tag{3.20}$$

When exciting heteronuclear RMs, the effective volume takes a different form. In general, the two species may have different temperatures, or largely different masses (consider a mixture of Li and Sr, for example) which would cause their density distributions to be different. In this case we follow the same prescription as above. The local excitation rate is given by

$$\dot{n}(r) \sim \kappa n_A(r) n_B(r), \tag{3.21}$$

and integrating over the trap yields

$$\dot{N} \sim \kappa n_0^{(A)} n_0^{(B)} \left(\frac{2\pi k_B T_A T_B}{(m_A T_B + m_B T_A)\bar{\omega}^2}\right) \stackrel{\text{def}}{=} \kappa n_0^{(A)} n_0^{(B)} V_{AB}. \tag{3.22}$$

The above discussion assumes that the number of atoms inside a given Rydberg orbital volume, V_R, is much smaller than 1. If more than one perturber is present in the Rydberg volume, the energy shift due to the interaction between the Rydberg electron and the neutral atoms forbids the creation of dimer. The probability of finding N atoms inside of the Rydberg volume V_R is given by Poisson statistics. For sufficiently high densities ($\sim 2 \times 10^{14}\,\mathrm{cm}^{-3}$ at $n = 38$) the probability of finding

two particles per Rydberg volume exceeds that of finding one, and would cause a suppression of dimer creation. The densities in our experiments are typically on the order of $10^{13}\,\mathrm{cm}^{-3}$, so we can safely ignore this effect, but the full expression for the excitation rate accounting for Poisson statistics is handled in Appendix B.

Chapter 4

Probing nonlocal spatial correlations in quantum gases with ultralong-range Rydberg molecules

In this chapter we present the work done in 2019 on probing the pair correlations function $g^{(2)}(R)$ in a cold gas of indistinguishable bosons, indistinguishable fermions, and a statistical mixture of ten species of particles. The experimental contributions in this work include the development of the laser cooling and trapping procedure for ^{84}Sr and ^{87}Sr mixtures. We also developed the spin-polarization procedure, and the techniques for measuring the spin-polarization fidelity using Rydberg spectroscopy. The pair correlation function was determined by using a ratio of excitation rates between the indistinguishable samples and an unpolarized gas of ^{87}Sr, which approximates a gas of classical particles. We derived the relationship between $g^{(2)}(R)$ and the excitation rate of RMs using Fermi's golden rule, and how to separate the corrections for the density distribution of the gas and other factors that do not relate to $g^{(2)}(R)$. Our theory collaborators provided a more rigorous theoretical calculation of the RM lineshape to directly show the relationship between the excitation rate and the pair correlation function, and the theoretical curves shown in Figure 4.3. The paper is reproduced in this chapter. I drafted the text and was lead author, our co-authors contributed to editing the manuscript.

In Section 4.1 we present the published journal article, which can be found at [70]. In Section 4.2 we provide a more detailed derivation of the relationship between the reduced matrix elements for comparing ^{84}Sr and unpolarized samples of ^{87}Sr.

4.1 Publication: Probing nonlocal spatial corelations in quantum gases with ultralong-range Rydberg molecules

Our understanding of quantum gases has been greatly enhanced by *in situ* measurements of spatial correlations, which can arise from Bose or Fermi quantum statistics [36–40] or the formation of more complex entangled states [43, 44, 71]. Quantum-gas microscopes resolve correlations on length scales on the order of, or larger than a wavelength of light, enabling studies of quantum magnetism [46] and the superfluid-to-Mott insulator transition [45]. Inelastic loss from spin flips and three-body recombination probe two- and three-body spatial correlations at very short range [37, 44]. Despite the tremendous progress in experimental techniques, *in situ* probes of spatial correlations between these length scales are still lacking. Many complex many-body phenomena take place at these intermediate scales, and such a probe would thus provide a new window onto physics such as the formation of halo dimers [72] and Efimov trimers [7] related to resonant atomic scattering states, long-range Cooper pairs in strongly interacting Fermi gases [73, 74], and strongly correlated 1D gases [44, 71].

Here we demonstrate photo-excitation of ultralong-range Rydberg-molecule (RM) dimers [15, 26, 75] in an ultracold gas as an *in situ* probe of nonlocal pair-correlations [36] at previously inaccessible length scales. At short range, we observe bunching in a thermal gas of spinless bosonic ^{84}Sr and Pauli exclusion, or anti-bunching, in a polarized gas of fermionic ^{87}Sr atoms, reflecting the effects of (anti-)symmetrization of the wave functions dictated by the spin statistics theorem. These correlations vanish at distances greater than the thermal de Broglie wavelength, which is $\sim 200\,\mathrm{nm}$ in these experiments. Bunching and anti-bunching have been observed before in quantum gases with destructive measurement schemes [37, 40, 76–79]. In contrast,

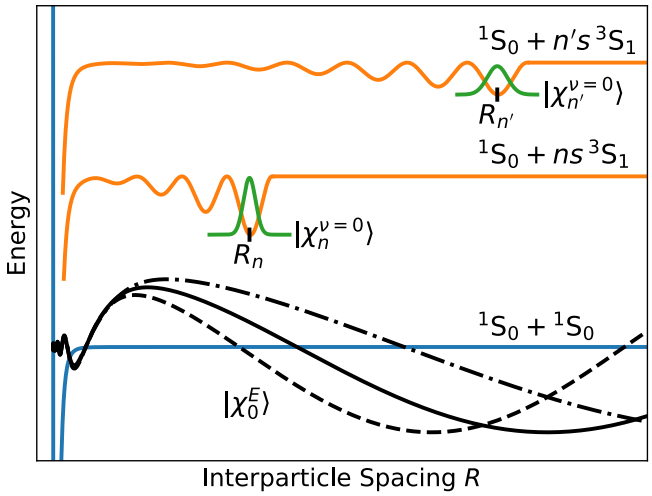

Figure 4.1 : Schematic of the excitation to a Rydberg molecular state $|\chi_n^{\nu=0}\rangle$ (green) in a Rydberg potential (orange) from the state of a pair of colliding atoms $|\chi_0^E\rangle$ (black). The wavefunction of the ground $\nu = 0$ molecular dimer state is highly localized in the outer lobe of the molecular potential at R_n, as shown for two different principal quantum numbers n and n'. Asymptotically far outside the short-range interatomic potential (blue), $|\chi_0^E\rangle$ describes a free particle state with wave vector $k = \sqrt{2\mu E/\hbar^2}$ for collision energy E and reduced mass μ. The experiment samples a thermal distribution of collision energies (represented by the different $|\chi_0^E\rangle$ curves), and the molecular excitation rate is proportional to the pair correlation function $g^{(2)}(R_n)$.

RM excitation can be nearly non-destructive [80]. It can also probe the temporal evolution of correlations since the molecular binding energy, and therefore the inverse excitation time scale, are much greater than the relevant many-body energy scales of quantum gases, such as the Fermi energy or chemical potential.

In an RM dimer, one ground-state atom is bound to a highly excited Rydberg atom. The binding potential results from scattering between the Rydberg electron and ground-state atom [18, 75], and it therefore follows the Rydberg-electron proba-

bility distribution. (See Fig. 4.1.) For Sr, the atom-electron interaction is attractive, leading to formation of RMs. The molecular potential is also attractive for Rydberg excitations in Rb and Cs quantum gases [26, 27, 81], which attests to the broad applicability of the probe we investigate in the present work.

To probe spatial correlations, we exploit the fact that the internuclear separation in the most deeply bound RM dimer state, $|\chi_n^{\nu=0}\rangle$, is highly localized in the potential minimum formed by the outer lobe of the Rydberg wavefunction located at a separation $R_n \approx 2(n-\delta)^2 a_0$ (Fig. 4.1). The quantum defect is $\delta = 3.37$ for the $5sns\,{}^3\mathrm{S}_1$ states used in this work, and $a_0 \approx 0.05\,\mathrm{nm}$ is the Bohr radius. In a simple semi-classical picture, the formation of a molecule requires the presence of atoms separated by approximately R_n. Thus the excitation rate serves as a measure of the relative probability of finding two particles with separation R_n in the initial gas, which can be quantified by the nonlocal pair-correlation function $g^{(2)}(R_n)$. For principal quantum number n between 20 and 75, R_n ranges from 400 to 10^4 a_0, providing an *in situ* probe of correlations at previously inaccessible length scales. This method is similar to the mapping of short-range ($\lesssim 100\,a_0$) atomic scattering states with photoassociative spectroscopy of low-lying energy levels [47–51]. The possibility of measuring non-local correlations with RMs was mentioned in [82], and short-range correlations were probed with RM excitation in [80].

In the present work, non-degenerate quantum gases of spin-polarized, fermionic ^{87}Sr ($I = 9/2$) and bosonic ^{84}Sr ($I = 0$) are used to measure the effects of quantum statistics on the excitation rate of RMs and thus on the pair correlation function. As a reference, we employ an unpolarized sample of ^{87}Sr, which provides a good approximation to a gas of uncorrelated particles because of its tenfold-degenerate ground state. Accordingly, the excitation rates of RMs in ^{84}Sr and spin-polarized ^{87}Sr are compared to those of unpolarized ^{87}Sr to extract $g^{(2)}(R)$. A preliminary

discussion of the fermion data was presented in [83].

Atoms are laser cooled, loaded into an optical dipole trap (ODT) formed using 1064 nm light, and evaporatively cooled as described in [83]. Experiments with ^{87}Sr are performed with ^{84}Sr present in the trap for sympathetic cooling.

For measurements involving spin-polarized ^{87}Sr, a bias magnetic field of 7.6 G is applied after loading the ODT, which produces a Zeeman splitting of ~ 650 kHz between adjacent magnetic sublevels in the $5s5p\,^3\mathrm{P}_1$ $F = 9/2$ manifold. Before evaporative cooling, population is transferred into the $m_F = 9/2$ ground state by applying a series of σ^+ polarized 689 nm laser pulses approximately 50 kHz red-detuned from each $m_F \to m_F + 1$ transition. Once this optical pumping is complete, the field is lowered to ~ 1 G to maintain the quantization axis. Experiments with unpolarized samples are performed in zero magnetic field. For all ^{87}Sr experiments, once the final temperature is reached, any remaining ^{84}Sr atoms are removed by scattering light resonant with the $5s^2\,^1\mathrm{S}_0 \to 5s5p\,^3\mathrm{P}_1$ transition. The isotope shift between ^{87}Sr and ^{84}Sr ensures that no significant heating of the ^{87}Sr atoms occurs.

A two-photon transition is employed to create Rydberg atoms or molecules. The first photon, at 689 nm, has a fixed blue-detuning of 14 MHz from the $5s5p\,^3\mathrm{P}_1$ level ($F = 11/2$ for ^{87}Sr). The energy of the second photon, at 320 nm, is scanned to obtain spectra for excitation to $5sns\,^3\mathrm{S}_1$ levels ($F = 11/2$ for ^{87}Sr) (Figs. 4.2 and 4.3). The excitation lasers are applied for 10 μs, after which an electric field is applied to ionize Rydberg excitations. Product electrons are counted using a microchannel plate detector. Typically, 1000 laser pulses at a single frequency are applied to each sample. Excitation rates are kept much less than one per laser shot to avoid Rydberg blockade effects (blockade radius $R_B = (C_6/2h\gamma)^{1/6} \sim 3.5\,\mu$m at $n = 39$ for linewidth $\gamma = 300\,$kHz and $C_6 = 7 \times 10^{-61}\,\mathrm{Jm}^6$ [12]).

To quantitatively measure the pair-correlation function $g^{(2)}(R)$, the molecular

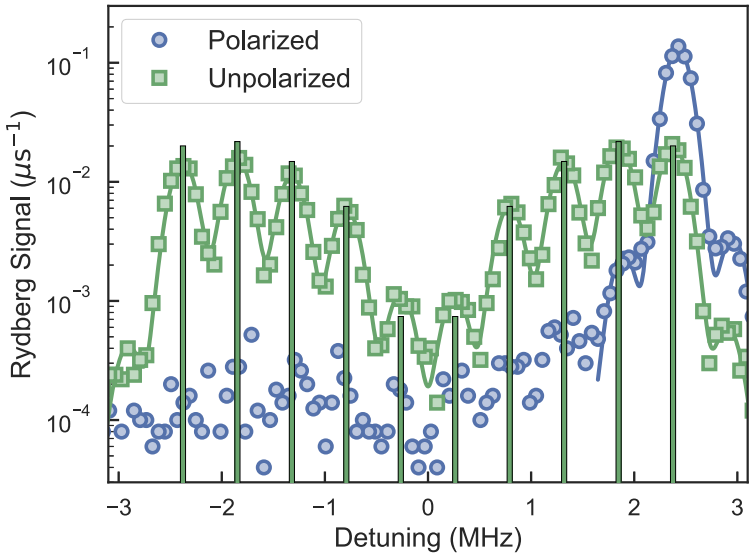

Figure 4.2 : Spectra for excitation to the $n = 34$ atomic Rydberg state for spin-polarized (circles) and unpolarized (squares) gases of ^{87}Sr. A 1 G magnetic field causes the observed Zeeman splitting. The vertical bars indicate the square of the product of Clebsch-Gordan coefficients associated with each transition, and differences with the measured peak heights point to small deviations from an equal distribution of m_F levels in the ground state. Curves show fits used to extract the population in each m_F level. The small features on the extreme right and extreme left of the plot arise due to imperfect polarization of the first photon, and are included in the model for completeness.

excitation rate in a single-component gas is normalized with respect to the rate in an unpolarized 87 Sr gas. This allows us to cancel experimental factors and, most importantly, n-dependent contributions to the excitation rate that are unrelated to spatial correlations. Maintaining similar sample densities and temperatures increases the accuracy of this procedure. To this end, we approximately match the final trap potential, excitation laser intensity, atom number ($N \sim 2 \times 10^5$), peak density ($\rho \sim 3 \times 10^{13}\,\mathrm{cm}^{-3}$), and sample temperature. The latter quantities are inferred from

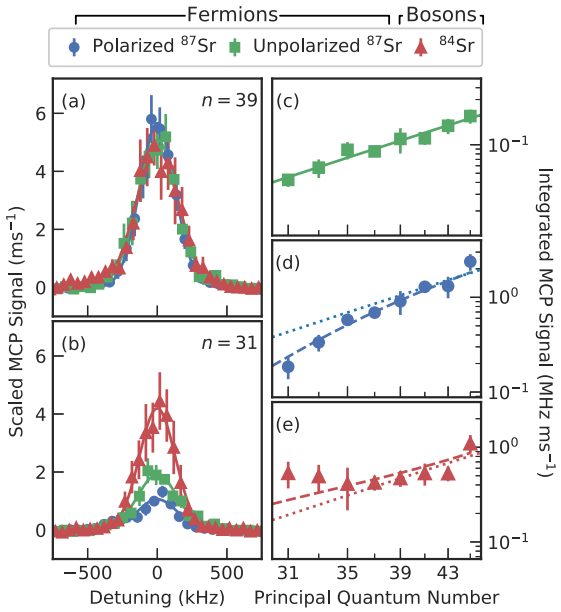

Figure 4.3 : Raw data showing the effects of quantum statistics on the excitation of RMs. (a,b) Spectra for excitation to the $|\chi_n^{\nu=0}\rangle$ dimer ground state for a spin-polarized ^{87}Sr Fermi gas (blue, circles), for an unpolarized ^{87}Sr Fermi gas (green, squares) and a spinless ^{84}Sr Bose gas (red, triangles). The spectra for the polarized Fermi gas and the spinless Bose gas are scaled such that all spectra match at $n = 39$ to highlight the effects of quantum statistics at low n (see text). (c-e) Integral of the RM dimer spectra versus principal quantum number for (c) unpolarized ^{87}Sr, (d) polarized ^{87}Sr, and (e) ^{84}Sr. In (c), a fit (solid green line) shows that the integral for the unpolarized ^{87}Sr gas varies as $(n-\delta)^{\alpha}$, with $\alpha = 3.5(3)$, reflecting variation in the n-dependent Franck-Condon factors and electronic matrix element, with some contribution from faster natural decay at lower n. (d,e) The dotted lines are translations of the $(n-\delta)^{\alpha}$ curve, and dashed lines are theory predictions accounting for quantum statistics and the n-dependent structure of Rydberg molecular wavefunctions.

time-of-flight absorption imaging on the $5s^2\,{}^1\mathrm{S}_0 \rightarrow 5s5p\,{}^1\mathrm{P}_1$ transition at 461 nm and knowledge of the trapping potential [84]. The final trap oscillation frequencies and RMS cloud radii are approximately $(125, 125, 300)$ Hz and $(12, 12, 5)$ μm respectively,

with the tight axis along gravity.

The effectiveness of optical pumping is measured spectroscopically through excitation of the $5sns\,^3\mathrm{S}_1$ $F = 11/2$ atomic Rydberg state in a 1 G magnetic field using two π-polarized photons ($\Delta m_F = 0$). The spectrum (Fig. 4.2) is fit to an appropriate lineshape model to determine the degree of polarization. For a polarized sample, at least 90% of the atoms occupy the $m_F = 9/2$ state. For the unpolarized Fermi gas, the populations in the ten different ground-state m_F levels are approximately equal ($\pm 25\%$). The differing heights of the Zeeman peaks in the spectrum for the unpolarized sample arise from the variation of transition strength from the ground state to final states with different magnetic quantum numbers as given by angular momentum coupling (Clebsch-Gordan coefficients).

To probe spatial correlations and measure $g^{(2)}(R)$, a polarization configuration different from the one used to probe polarization is used to create Rydberg molecules. The first photon is σ^+ polarized, and the second photon remains π polarized, which maximizes the transition strength for the spin-polarized sample.

The influence of quantum statistics on spatial correlations is readily apparent in the spectra for excitation to the $\nu = 0$ RM state at principal quantum numbers $31 \leq n \leq 45$ ($1400\,a_0 \leq R_n \leq 3200\,a_0$). Figures 4.3(a,b) show spectra for $n = 31, 39$. The spectra for the spin-polarized Fermi gas ($T = 860\,\mathrm{nK}$) and Bose gas ($T = 650\,\mathrm{nK}$) are scaled such that their integrals match the integral of the unpolarized data ($T = 860\,\mathrm{nK}$) at $n = 39$, where the effects of quantum statistics are small [Fig. 4.3(a)]. With decreasing quantum number [Fig. 4.3(b)], the suppression of the excitation rate in the spin-polarized Fermi gas arising from Pauli exclusion and the enhancement for the Bose gas due to bunching are evident.

Figure 4.3(c-e) includes the integral of the molecular signal measured for each principal quantum number for (c) unpolarized ^{87}Sr, (d) polarized ^{87}Sr, and (e) ^{84}Sr.

The integrals for the unpolarized Fermi gas can be fit well by an $(n-\delta)^{3.5}$ power law (solid green line). This agrees well with the approximate $(n-\delta)^{3.8}$ scaling predicted using numerical calculations of the overlap integral between scattering and molecular states and the $1/(n-\delta)^3$ scaling of the electronic dipole transition matrix element. In Fig. 4.3(d,e), the dotted lines vary as $(n-\delta)^{3.5}$ and are scaled to match the polarized ^{87}Sr and ^{84}Sr data at high quantum number. In the absence of effects of quantum statistics, the integrals for all samples should have the same n dependence but different overall amplitudes that reflect n-independent factors such as Clebsch-Gordan coefficients (Fig. 4.2), differences in detector efficiency arising from the magnetic field needed to preserve quantization for the spin-polarized sample, and small differences in laser intensity between the Bose and spin-polarized Fermi gas experiments. Deviations from the $(n-\delta)^{3.5}$ power law at low quantum number result from quantum statistics.

The excitation probability to the ground vibrational state ($\nu = 0$) of the RM for principal quantum number n is proportional to a Franck-Condon factor that accounts for a thermal average over collision energy ($\langle ... \rangle_E$) for initial two-particle states and all possible initial and final rotational states. This reduces to $\mathcal{F}_n = \sum_l (2l+1) \langle | \int dR R^2 \chi_n^{\nu=0}(R) \chi_0^{E,l}(R) |^2 \rangle_E$, where $\chi_n^{\nu=0}$ is the radial wavefunction for the RM, which is independent of l for the low-l states contributing to $\mathcal{F}_n$. $\chi_0^{E,l}$ is the wavefunction for the initial state with collisional energy E and rotational angular momentum quantum number l. To account for quantum statistics, the sum over l is understood to be restricted to initial states with allowed exchange symmetry. This yields the theory curves in Figs. 4.3(d-e) (dashed lines), which are in reasonable agreement with the data.

$\chi_n^{\nu=0}$ is well-localized at R_n on the scale of the initial collisional state. In particular, the wave function for $n < 50$ is localized within a single potential well (Fig.

4.1). This allows $\mathcal{F}_n$ to be approximated as

$$\mathcal{F}_n \simeq \left| \int dR R^2 \chi_n^{\nu=0}(R) \right|^2 g^{(2)}(R_n) \equiv \mathcal{O}_n \, g^{(2)}(R_n) \tag{4.1}$$

where $g^{(2)}(R_n)$ is the pair correlation function for separation R_n, and $\mathcal{O}_n$ is an effective Franck-Condon factor. This derivation can be generalized to the case of an initial state of a many-body Fermi or Bose gas at arbitrary density and temperature and with multiple internal spin states initially populated.

When experimental factors are taken into account, the integrated signal becomes

$$\mathcal{S}_n \simeq \alpha I_1 I_2 \mathcal{N} \beta_n C \mathcal{O}_n g^{(2)}(R_n), \tag{4.2}$$

which is proportional to the detector efficiency α, the two-photon-excitation laser intensities I_1 and I_2, the volume integral of the square of the density distribution $\mathcal{N} \equiv \int d^3r \rho(\mathbf{r})^2$, a factor β_n proportional to the square of the reduced two-photon electronic-transition matrix element, a factor C expressible in terms of Clebsch-Gordan coefficients, $\mathcal{O}_n$, and $g^{(2)}(R_n)$.

For non-degenerate gases of noninteracting particles, $g^{(2)}(R)$ should be given by

$$g^{(2)}(R) = 1 + \epsilon \, \mathrm{e}^{-2\pi R^2/\lambda_{\mathrm{dB}}^2}, \tag{4.3}$$

where $\lambda_{\mathrm{dB}} = h/\sqrt{2\pi m k_B T}$ is the thermal de Broglie wavelength, and ϵ equals $+/-1$ for indistinguishable thermal bosons/fermions in identical internal states and 0 for classical statistics [36, 85]. Trap and phase-space-density-dependent corrections to Eq. (4.3) will vary with separation R and are always less than $z/10$ [36], where $z \approx \rho \lambda_{\mathrm{dB}}^3$ is the fugacity. The highest peak fugacity of any of the samples used in these experiments is $z = 0.4$, and corrections are small. Eq. (4.3) neglects interactions between ground-state particles, which modify spatial correlations at length scales

less than the scattering length or the range of the ground-state atom-atom molecular potential, which are much smaller than R_n probed in this experiment.

Equation (4.2) is used to experimentally determine $g^{(2)}(R_n)$ for indistinguishable particles in identical internal states by normalizing the integrated signals for the bosons and spin-polarized fermions to the integrated signal for the unpolarized fermions. This cancels common factors β_n and $\mathcal{O}_n$. For the unpolarized Fermi gas, we assume $g^{(2)}(R) = 1 - 0.1\mathrm{e}^{-2\pi R^2/\lambda_{\mathrm{dB}}^2}$, which is the generalization of Eq. (4.3) for equal populations in the ten ground spin-states. The remaining factors that vary between different experimental runs and different isotopes and sample polarizations, are either measured or calculated independently. The Clebsch-Gordan factor for the unpolarized gas (C_{unpol}) is calculated assuming equal populations in all ground spin states, yielding $C_{\mathrm{pol}}/C_{\mathrm{unpol}} = 5.05$, where C_{pol} describes bosons and polarized fermions. Temperatures and densities of each sample and the unpolarized gas used for normalization match within 10% in all cases. For the Bose gas, $T/T_{\mathrm{c}} \approx 1.5$ where T_{c} is the critical temperature for Bose-Einstein condensation. For the polarized Fermi gases, $T/T_{\mathrm{F}} \approx 1.0$, where T_{F} is the Fermi temperature. For the unpolarized Fermi gases, $T/T_{\mathrm{F}} \approx 2$. Density distributions are calculated using the appropriate Bose or Fermi distributions.

At large separations, where the effect of quantum statistics should be negligible, this procedure yields $g^{(2)}(R) = 1.5$ rather than the expected value of 1. A systematic deviation of this size is consistent with uncertainties in relative populations of the initial internal spin states of the unpolarized Fermi gas and in trap geometry and resulting density profiles. Ratios are thus divided by an additional correction factor of 1.5 to obtain the values of $g^{(2)}(R_n)$ in Fig. 4.4.

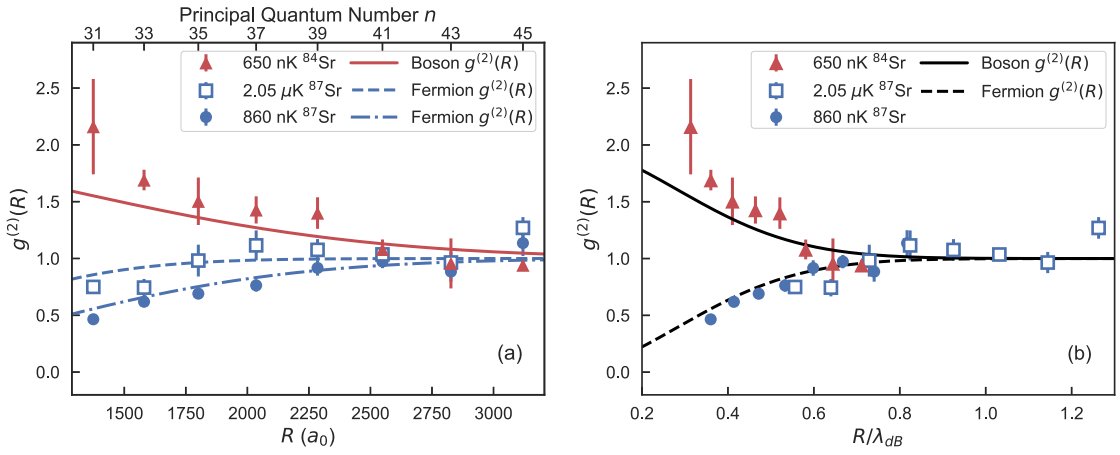

Figure 4.4 : Measured pair-correlation function for indistinguishable particles in identical internal states. (a) $g^{(2)}(R)$ for a Bose gas and Fermi gases at two different temperatures plotted against interparticle separation, R_n. Sample temperatures are indicated in the legend. (b) $g^{(2)}(R)$ for Fermi and Bose gases plotted against R_n scaled by the thermal de Broglie wavelength. The two sets of fermion measurements (blue symbols) fall onto a single curve and approach a constant value at large scaled distances. Error bars indicate statistical fluctuations from repeated measurements. Expected $g^{(2)}(R)$ (Eq. (4.3)) for bosons (solid) and fermions (dashed and dot-dashed) are shown by the lines.

At lower values of n the normalized integrated signals for the bosons and fermions clearly deviate from unity (Fig. 4.4(a)). The boson signal increases while the fermion signal decreases, which is consistent with bunching and anti-bunching respectively. The Fermi-gas experiment was performed at two different temperatures, and anti-bunching is less pronounced in the warmer sample reflecting the shorter thermal de Broglie wavelength. Figure 4.4 also shows that the results follow the expected behavior for $g^{(2)}(R)$ (Eq. (4.3)).

On a scaled, dimensionless axis (Fig. 4.4(b)), the two fermionic data sets fall on the same curve and approach a constant value for larger R/λ_{dB}. Effects of quantum

statistics - bunching for bosons and anti-bunching due to Pauli exclusion for fermions - are strikingly evident.

In summary, we have demonstrated that photoexcitation of the most deeply bound, $\nu = 0$ dimer RM state provides an *in situ* probe of pair-correlations in an ultracold gas that can be tuned over previously inaccessible length scales. These results suggest other interesting phenomena that can be studied with this diagnostic. For example, the pair-correlation function in a gas with a large s-wave scattering length, in the range of R_n probed in this experiment, should show strong deviations from the non-interacting result presented in Eq. (4.3). Stronger suppression/enhancement effects on higher-order correlations should be observable with trimers, tetramers, etc. Moreover, due to the fact that Rydberg molecule formation takes place on a time scale ($\sim 1\,\mu$s) much faster than the relevant many-body dynamics of quantum gases, RMs hold promise for *in situ* probing of the time evolution of ensemble averages of correlations during the non-equilibrium dynamics following quantum quenches or in driven many-body systems.

4.2 Derivation of C

In [70] we extracted $g^{(2)}(R)$ by taking ratios of integrated signals from spin-polarized ^{87}Sr or ^{84}Sr to unpolarized ^{87}Sr. As discussed in Section 2.5 the excitation rate of RMs is proportional to the square of the two-photon Rabi frequency, Ω,

$$\Omega = \frac{\Omega_{g,i}\Omega_{i,r}}{4\Delta}. \tag{4.4}$$

The single photon Rabi frequencies are related to matrix elements,

$$\Omega_{i,j} \sim \langle F_i m_{F,i}|er_q|F_j m_{F,j}\rangle, \tag{4.5}$$

which can be expressed by the Wigner-Eckart theorem

$$\langle F_i m_{F,i}|er_q|F_j m_{F,j}\rangle = (-1)^{F_j-1+m_{F,i}} \begin{pmatrix} F_j & 1 & F_i \\ m_{F,j} & q & -m_{F,i} \end{pmatrix} \langle F_i||e\mathbf{r}||F_j\rangle. \tag{4.6}$$

For the experiments in [70] we used a σ^+ polarized 689 nm beam and a π polarized 320 nm beam for all of the Rydberg excitations, so the angular factor of the total excitation rate is

$$C = \beta_n \sum_{m_F} N_{m_F} \begin{pmatrix} F_g & 1 & F_i \\ m_F & 1 & -(m_F+1) \end{pmatrix}^2 \begin{pmatrix} F_i & 1 & F_r \\ m_F+1 & 0 & -(m_F+1) \end{pmatrix}^2 \tag{4.7}$$

Where $\beta_n = |\langle F_r||e\mathbf{r}||F_i\rangle|^2|\langle F_i||e\mathbf{r}||F_g\rangle|^2/16\Delta^2$, and N_{m_F} is the number of atoms in each ground-state m_F level. In the fermion experiment $F_g = 9/2$, $F_i = 11/2$, and $F_r = 11/2$. We can assume that the unpolarized sample is made up of equal populations of each of the ten m_F levels, that the polarized sample only contains atoms in the $m_F = 9/2$ level, and that the total number of atoms is the same.

Therefore

$$C_{pol} = \beta_n \begin{pmatrix} 9/2 & 1 & 11/2 \\ 9/2 & 1 & -11/2 \end{pmatrix}^2 \begin{pmatrix} 11/2 & 1 & 11/2 \\ 11/2 & 0 & -11/2 \end{pmatrix}^2 \tag{4.8}$$

$$C_{unpol} = \beta_n \sum_{m_F=-9/2}^{9/2} 0.1 \times \begin{pmatrix} 9/2 & 1 & 11/2 \\ m_F & 1 & -(m_F+1) \end{pmatrix}^2 \begin{pmatrix} 11/2 & 1 & 11/2 \\ m_F+1 & 0 & -(m_F+1) \end{pmatrix}^2, \tag{4.9}$$

which gives the value of $C_{pol}/C_{unpol} = 5.05$ as stated in [70].

The value of C_{pol}/C_{unpol} is simple to calculate since the reduced matrix element β_n simply cancels out. However, ^{84}Sr does not have hyperfine structure, and therefore we must decompose the ^{87}Sr matrix elements in terms of the uncoupled m_I, m_J basis. The state $|Fm_F\rangle$ can be written as

$$|Fm_F\rangle = \sum_{m_I,m_J} \langle m_I m_J | Fm_F\rangle |m_I m_J\rangle \tag{4.10}$$

where

$$\langle m_I m_J | Fm_F\rangle = (-1)^{J-I+m_F}\sqrt{2F+1} \begin{pmatrix} J & I & F \\ m_J & m_I & -m_F \end{pmatrix}. \tag{4.11}$$

Therefore we can expand a dipole matrix element as

$$\langle Fm_F|er_q|F'm'_F\rangle = (-1)^{J+J'-I-I'} \sum_{\substack{m_I,m_J \\ m'_I,m'_J}} (-1)^{m_F+m'_F}\sqrt{(2F+1)(2F'+1)} \times \begin{pmatrix} J & I & F \\ m_J & m_I & -m_F \end{pmatrix} \begin{pmatrix} J' & I' & F' \\ m'_J & m'_I & -m'_F \end{pmatrix} \langle Jm_J|er_q|J'm'_J\rangle \langle Im_I|I'm'_I\rangle. \tag{4.12}$$

Using the orthogonality relation

$$\langle Im_I|I'm'_I\rangle = \delta_{m_I,m'_I}\delta_{I,I'} \tag{4.13}$$

and applying the Wigner-Eckart theorem gives

$$\langle Fm_F|er_q|F'm'_F\rangle = (-1)^{J+2J'-2I-1}\sum_{m_J,m'_J,m_I}(-1)^{m_F+m'_F+m_J}\sqrt{(2F+1)(2F'+1)}\times$$
$$\begin{pmatrix} J & I & F \\ m_J & m_I & -m_F \end{pmatrix}\begin{pmatrix} J' & I & F' \\ m'_J & m_I & -m'_F \end{pmatrix}\begin{pmatrix} J' & 1 & J \\ m'_J & q & -m_J \end{pmatrix}\langle J||e\mathbf{r}||J'\rangle, \quad (4.14)$$

which finally gives the $|F, m_F\rangle$ matrix elements in terms of the reduced J matrix elements.

For bosons C is simply

$$C_{boson} = \alpha_n \begin{pmatrix} 0 & 1 & 1 \\ 0 & 1 & -1 \end{pmatrix}^2 \begin{pmatrix} 1 & 1 & 1 \\ 1 & 0 & -1 \end{pmatrix}^2 \quad (4.15)$$

where $\alpha_n = |\langle J_r||e\mathbf{r}||J_i\rangle|^2|\langle J_i||e\mathbf{r}||J_g\rangle|^2$, and we can rewrite C_{unpol} as

$$C_{unpol} = \alpha_n \sum_{m_F=-9/2}^{9/2} 0.1 \times \mathcal{X}(1,0,11/2,9/2,m_F,1)^2\mathcal{X}(1,1,11/2,11/2,m_F+1,0)^2. \quad (4.16)$$

Where we have defined $\mathcal{X}$ to simplify the notation (we omit $I = 9/2$ from the argument):

$$\mathcal{X}(J,J',F,F',m_F,q) =$$
$$\sum_{\substack{m_J+m_I=m_F \\ m'_J+m_I=m'_F}}(-1)^{m_J}\sqrt{(2F+1)(2F'+1)}\begin{pmatrix} J & I & F \\ m_J & m_I & -m_F \end{pmatrix}\begin{pmatrix} J' & I & F' \\ m'_J & m_I & -m'_F \end{pmatrix}\begin{pmatrix} J' & 1 & J \\ m'_J & q & -m_J \end{pmatrix} \quad (4.17)$$

The ratio can be evaluated numerically to find $C_{boson}/C_{unpol} = 5.05$, which is the same value as C_{pol}/C_{unpol}. This is not particularly surprising because when we are driving the spin-polarized sample we are always addressing a transition between two stretched states where $F = m_F = I + J$.

Chapter 5

Heteronuclear Rydberg molecules

In this chapter we present the work done in 2020 regarding heteronuclear RMs. The motivation of this work was a step toward studying a strongly interacting mixture with the methods from Chapter 4. The experimental contributions were the development of the laser cooling and trapping procedure for the strongly interacting mixture of ^{84}Sr and ^{88}Sr, as well as the Rydberg spectroscopy system for exciting either ^{84}Sr or ^{88}Sr to the $5sns\,^3S_1$ state with $n = 31 - 39$. We observe an isotope shift $\nu = 0$ molecular binding energy, and derived a simple scaling relationship with principal quantum number n that is reasonably accurate. We also derived the density scaling laws and calculated the effective volumes presented in Section 3.1. Our theory collaborators Yoshida and Burgdörfer provided theoretical calculation of the isotope shifts, and calculations of the RM potentials and wavefunctions. The published journal article can be found at [30]. The paper is reproduced in this chapter. I drafted the text and was lead author, our co-authors contributed to editing the manuscript.

5.1 Publication: Heteronuclear Rydberg molecules

Ultralong-range Rydberg molecules (RMs) are formed by the scattering between an excited Rydberg electron and at least one nearby neutral atom in a dense gas. Initially predicted theoretically [75], these molecules have been the subject of intense study following their initial observation in Rb [26] and subsequent observations in Cs [27] and Sr [15]. The internuclear potential inherits its shape from the Rydberg-electron probability distribution and supports bound states with bond lengths on the order of the radius of the Rydberg orbital $R_n \sim 2n^2$, ~ 100 nm at $n = 35$. Recent studies have focused on the large permanent electric dipole moments of so-called trilobite and butterfly RMs [27, 29], ultracold chemistry and the stability of RMs in dense cold gases [86, 87], and on methods to use RMs to study low energy atom-ion scattering [88] and probe the pair-correlation function of quantum gases [70].

In this work we demonstrate photo-excitation of heteronuclear RM dimers using a mixture of ^{88}Sr and ^{84}Sr. We observe an isotope shift in the binding energy between the ground vibrational state of ^{84}Sr + ^{84}Sr, ^{88}Sr + ^{84}Sr and ^{88}Sr + ^{88}Sr RMs, and measure the scaling of molecule production with ^{88}Sr and ^{84}Sr density. Spectroscopy of heteronuclear molecules provides a sensitive probe of RM potentials and can be used to measure the relative densities of constituent atomic species in a mixture, as proposed in theoretical work on bialkali heteronuclear RMs [82]. Excitation of heteronuclear RM dimers from varied and well-controlled atomic constituents will enable the study of spatial correlations and collisional wavefunctions in atomic mixtures [70]. The combination of ^{88}Sr and ^{84}Sr is particularly interesting in this context because the system possesses an extremely large scattering length, $a_{88-84} \sim 1800\, a_0$, where a_0 is the Bohr radius [89, 90].

The interaction of an excited Rydberg electron and a ground-state atom gives rise

to a potential similar to that shown in Figure 5.1. The potential experienced by a ground-state atom, at distance R from the Rydberg atom nucleus, can be described in the Born-Oppenheimer approximation by a modified Fermi pseudopotential [18, 25, 75],

$$V(R) = \frac{2\pi\hbar^2 A_s(k)}{m_e} |\psi_{ns}(R)|^2 + \frac{6\pi\hbar^2 A_p^3}{m_e} |\nabla\psi_{ns}(R)|^2 , \tag{5.1}$$

where $\psi_{ns}(R)$ is the Rydberg electron wavefunction, m_e is the electron mass, and $A_s(k)$ and A_p are s-wave and p-wave scattering lengths, respectively. For simplicity momentum (k) dependence of the scattering length is only included for the s-wave interaction. For strontium $A_s(0) = -13.3\, a_0$ and $A_p = 9.7\, a_0$ [15] giving rise to an attractive potential. (In alkali atoms such as Rb the p-wave interaction [31] and the hyperfine structure [32, 33] affect the RM potential. In the strontium isotopes used here, these effects are absent.) This attractive potential supports a manifold of vibrational states labeled by the quantum number ν that appear as resonances red detuned from the atomic Rydberg state as shown in Figure 5.1. The binding energies of these molecular states scale as n^{-6}. For each principal quantum number, the potential supports many bound states, but we focus on the highly localized $\nu = 0$ state for $n = 31 - 39$ here. The polarization potential between the background atom and ion core is negligible for these states.

In the present experiment we create $\nu = 0$ homonuclear RM dimers comprised of $^{88}\mathrm{Sr}^* + {}^{88}\mathrm{Sr}$ and $^{84}\mathrm{Sr}^* + {}^{84}\mathrm{Sr}$, and heteronuclear dimers of $^{88}\mathrm{Sr}^* + {}^{84}\mathrm{Sr}$, where the star indicates the atom in the Rydberg state. Homonuclear dimers are excited from ultracold samples of either pure ^{88}Sr or pure ^{84}Sr. The chosen isotope is laser cooled in a broadband magneto-optical trap (MOT) operating on the $5s^2\,{}^1S_0 \rightarrow 5s5p\,{}^1P_1$ cycling transition at 461 nm, from which a fraction of the atoms spontaneously decay into the metastable $5s5p\,{}^3P_2$ state and are magnetically trapped in the quadrupole field of the MOT [56]. The atoms are repumped to the ground state and further

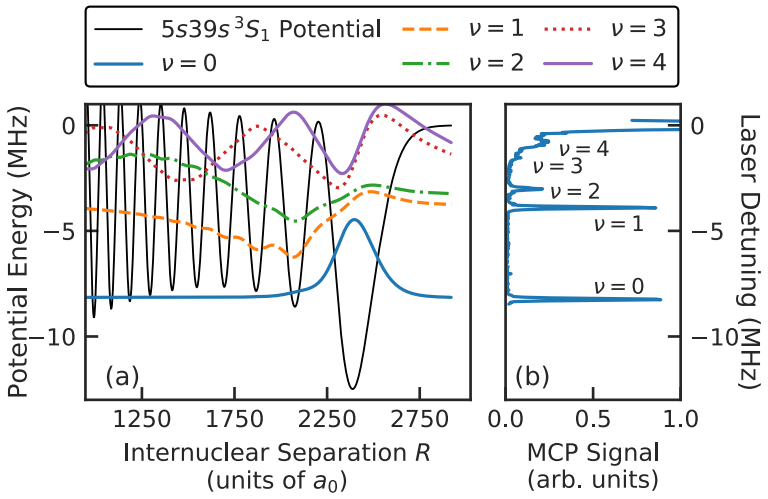

Figure 5.1 : a) The potential formed by the scattering between the $5s39s\,^3S_1$ Rydberg electron and a neutral Sr atom. The bound state wavefunctions are labeled by their vibrational quantum numbers ν and are offset by their binding energy. b) RM excitation spectrum observed when the excitation laser is detuned from atomic resonance (see text).

laser cooled using a narrow-band MOT operating on the $5s^2\,^1S_0 \rightarrow 5s5p\,^3P_1$ intercombination line at 689 nm and are then loaded into an optical dipole trap (ODT) formed by two perpendicular light sheets at 1064 nm as described elsewhere [83]. We reduce the intensity of the ODT beams over an interval of 500 ms to allow for evaporative cooling after which ^{84}Sr reaches a temperature of ~ 800 nK and a density of $9 \times 10^{12}\,\mathrm{cm}^{-3}$. The weak interactions between ^{88}Sr atoms (s-wave scattering length $a = -2\,a_0$ [90, 91]) make evaporative cooling less efficient, resulting in a final temperature of 1.1 μK and density of $6 \times 10^{12}\,\mathrm{cm}^{-3}$ for ^{88}Sr at the same trap depth.

To create heteronuclear RMs we prepare an ultracold mixture of ^{88}Sr and ^{84}Sr. The two isotopes are sequentially laser cooled in the broadband MOT and loaded

into the magnetic trap. From the magnetic trap the atoms are simultaneously repumped and cooled in a dual-isotope narrow-band MOT using laser light tuned to each isotope. The isotope shift of the $5s5p\,^3P_1$ intercombination line is sufficiently large that the ^{88}Sr and ^{84}Sr MOTs do not interfere with each other. From the narrow-line MOT, the mixture is loaded into the ODT and evaporatively cooled to the same trap depth as above. The sample temperature is set to $\sim$ 750 nK, and the large interspecies scattering length and resulting high collision rate ensures that the mixture is in thermal equilibrium. We can selectively measure the number and temperature of each isotope using absorption imaging on the $5s5p\,^1P_1$ line and find that the temperatures of the two isotopes are equal to within 10% at the end of the evaporation. During the evaporation stage there is rapid atom loss due to the large three-body recombination rate associated with the strong interspecies interactions, which limits the maximum attainable density. We work with a relatively low peak density of 5×10^{12} cm^{-3}, which yields samples with lifetimes on the order of a few hundred milliseconds. We can adjust the relative densities of the two isotopes by varying the load times of the broadband MOT. The ratio of ^{88}Sr to ^{84}Sr density is varied from 0.03 to 1 while maintaining approximately the same total number density and atom number $N \sim 3 \times 10^5$.

RMs are created in these ultracold samples using a two-photon excitation comprised of a fixed-wavelength 689 nm photon tuned near the $5s5p\,^3P_1$ level of the selected isotope and a 320 nm photon tuned to select the target Rydberg state. The target atom is excited to the $5sns\,^3S_1$ state with $n = 31 - 39$. For excitation of homonuclear ^{88}Sr (^{84}Sr) molecules, we apply a 689 nm photon detuned 15 MHz (80 MHz) from the $5s5p\,^3P_1$ state. To excite heteronuclear molecules we selectively excite ^{88}Sr to the $5sns\,^3S_1$ state in a background of ^{84}Sr using the same laser detunings used to create homonuclear ^{88}Sr molecules. The isotope shift of the $5sns\,^3S_1$ level

between ^{88}Sr and ^{84}Sr is 445 MHz over the range of principal quantum numbers considered in this work and ensures complete isotope selectivity of the atom that is excited electronically. The detuning of the 689 nm photon from the $5s5p\,^3P_1$ level of ^{84}Sr is sufficiently large that off-resonant scattering does not cause heating of the sample.

We generate spectra such as those shown in Figures 5.1 and 5.2 by scanning the energy of the 320 nm photon. We apply a 20 μs excitation pulse followed by an electric field ramp that ionizes any excited Rydberg atoms or molecules present in the sample. The liberated electrons are guided to a microchannel plate (MCP) detector where they are detected and counted. We repeat the excitation process 500 times per sample over 100 ms to build up statistics. The ODT beams are turned off during excitation to avoid AC stark shifts. To preclude the effects of Rydberg-Rydberg interactions we lower the power of the excitation lasers to ensure that fewer than one Rydberg atom is created per excitation pulse on average.

The first evidence for production of heteronuclear Rydberg molecules is provided by the presence of an isotope shift in the binding energy of the $\nu = 0$ dimer state. In Figure 5.2 we show normalized excitation spectra for $\nu = 0$ RM dimers in three different samples: a pure ^{88}Sr sample, excitation of a minority ^{88}Sr in a majority ^{84}Sr background, and a pure ^{84}Sr sample for principal quantum numbers between $n = 31 - 39$. Spectra are plotted versus the detuning from the atomic Rydberg line of the electronically excited isotope, shifted by the detuning corresponding to the $\nu = 0$ line for $^{88}\mathrm{Sr}^* + {}^{88}\mathrm{Sr}$. Resonances for molecules with lighter reduced mass are shifted closer to the atomic line as is expected.

The isotope shift increases with decreasing principal quantum number with a scaling that can be understood with a simple model that is valid for the range of quantum numbers studied here. The molecular potential is approximated as har-

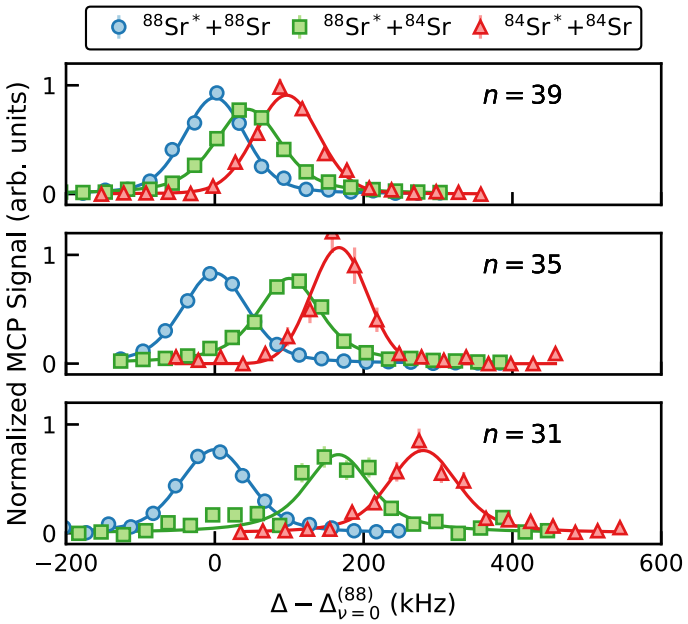

Figure 5.2 : Characteristic excitation spectra of $\nu = 0$ RMs in samples of pure ^{88}Sr (blue circles), minority ^{88}Sr excited in majority ^{84}Sr (green squares), and pure ^{84}Sr (red triangles) for principal quantum numbers $n = 31 - 39$. Each spectrum is plotted against the detuning, Δ, from the atomic Rydberg line of the excited isotope, shifted by the detuning for the $^{88}Sr^* + {}^{88}Sr$ $\nu = 0$ dimer state, $\Delta^{(88)}_{\nu=0}$. Resonances for molecules with smaller reduced mass are shifted closer to the atomic line as expected. All spectra are taken in the same trap and with similar total densities (see text). For the heteronuclear spectra the ratio of the ^{88}Sr and ^{84}Sr densities is ~ 0.1.

monic around $R = R_c$ at which the RM potential has a minimum value $V(R_c) = -d$, i.e.,

$$V(R) \simeq \frac{1}{2}\mu\omega^2(R - R_c)^2 - d \tag{5.2}$$

with μ the reduced mass of the dimer pair. Because the $\nu = 0$ state is highly localized in the most outer well (see Fig. 5.1), the binding energy can be approximated by $E_{\nu=0} = d - \hbar\omega/2$. Mass-dependent effects on the RM potential, such as variation of

the reduced mass of the electron and background atom are negligible on the level of our measurement accuracy. Effects beyond the Born-Oppenheimer approximation, such as the mass polarization energy between the Rydberg electron and the ground-state atom, are also negligible compared to the isotope shifts. Therefore the shift in the binding energy is related to the shift in the characteristic frequency ω, which varies as $\mu^{-1/2}$, where μ is the reduced mass of the dimer pair. To first order the relative shift in the harmonic potential's frequency is proportional to ω

$$\frac{\Delta\omega}{\omega} = -\frac{1}{2}\frac{\Delta\mu}{\mu}\,. \tag{5.3}$$

The expected scaling of ω and the isotope shift with n can be estimated within the harmonic approximation. The potential felt by the neutral atom follows the Rydberg electron probability density distribution for the $5sns\,{}^3S_1$ state and therefore has $N \simeq n$ nodes. The width, w, of the outer well scales as $w \sim R_n/N \sim 2n^2/n \sim n$, where R_n is the radius of the Rydberg orbital. The depth of the outer well scales as $d \sim n^{-6}$, the inverse of the volume of the electron orbital [26]. The potential parameters can thus be approximated through $\mu\omega^2 w^2 \sim d$, implying $\omega \sim \sqrt{d/w^2} \sim n^{-4}$. The isotope shift is proportional to ω as discussed above, and therefore should also scale as n^{-4}. Inclusion of anharmonic corrections [92] results in a somewhat more rapid decay with n, $n^{-\alpha}$, with $\alpha > 4$. Numerical calculations confirms such an approximate scaling. For the range of principal quantum numbers considered in this work the harmonic approximation yields an estimated isotope shift from a few hundred to a few tens of kHz which is close to the measured values. For quantum numbers $n \gtrsim 40$, the $\nu = 0$ vibrational state extends to adjacent wells of the potential to an increasing degree, and the harmonic approximation becomes poor.

Figure 5.3 shows the isotope shifts of spectral-line centers for $^{88}\mathrm{Sr}^* + {}^{84}\mathrm{Sr}$ and $^{84}\mathrm{Sr}^* + {}^{84}\mathrm{Sr}$ RMs with respect to $^{88}\mathrm{Sr}^* + {}^{88}\mathrm{Sr}$. Statistical uncertainties for exper-

imental data are smaller than the symbol size. The results agree reasonably well with the expected n^{-4} scaling. Figure 5.3 also shows theoretical predictions, which are calculated using the formalism of [68] to model RM excitation spectra. For this calculation, molecular energy levels are obtained by numerical diagonalization of the Hamiltonian matrix formed using the molecular potential (Eq. 5.1) with electron-atom scattering lengths from [15]. A thermal average over initial collision energies and sum over partial waves up to $\Lambda = 3$ is performed using Λ-dependent Frank-Condon factors. For $n = 31$, the RM rotational constant is $\sim 20\,\mathrm{kHz}$ and the spectral line can shift several tens of kHz from the position predicted in the absence of rotational effects. This shift is isotope dependent because heteronuclear RM dimers are excited from a pair of distinguishable bosons and states with both even and odd rotational quantum number can be excited, while only even values of Λ contribute in the homonuclear case. In addition, the very large scattering length a_{84-88} suppresses the Franck-Condon factors for s-waves for $^{88}\mathrm{Sr}^* + {}^{84}\mathrm{Sr}$. The quantitative agreement between isotope-shift values for experiment and theory is reasonable given the lower resolution of measurements used to determine parameters of the molecular potential [15].

The presence of the isotope shift discussed above is conclusive evidence of the creation of heteronuclear RMs. For future applications one key quantity of interest is the fidelity with which heteronuclear RMs can be produced. It is clear from Figure 5.2 that for lower quantum numbers ($n \lesssim 35$) and with a sufficiently narrow excitation-laser linewidth, one can excite heteronuclear molecules with almost perfect fidelity by taking advantage of the spectroscopic resolution of the isotope shift. However, when the involved electronic state, the combination of constituent isotopes, or the excitation laser system does not permit the required spectral selectivity, another method of determining excitation fidelity is required.

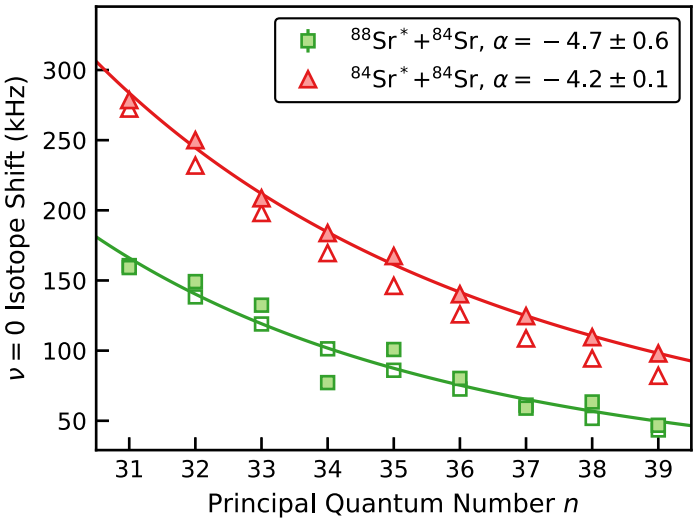

Figure 5.3 : The measured (filled symbols) and calculated (open symbols) isotope shifts for the $\nu = 0$ RM dimer in $^{88}Sr^* + ^{84}Sr$ and $^{84}Sr^* + ^{84}Sr$ compared to $^{88}Sr^* + ^{88}Sr$. The measured data are fitted to a power law $(n-\delta)^{\alpha}$ where $\delta = 3.371$ is the quantum defect of the $5sns\,^3S_1$ state. The fitted α are shown in the legend and agree reasonably with the expected n^{-4} scaling (see text).

As an example we consider the excitation of heteronuclear RMs at $n = 39$ where the isotope shift is 48 kHz, which is about half of the linewidth of the Rydberg excitation limited by the linewidth of the 320 nm laser system. If we assume that the distribution of atom positions is governed by Poissonian statistics and that the total number density, n, is much less than one per Rydberg-orbital volume, the RM excitation rate from the excitation of ^{88}Sr in a $^{88}Sr + ^{84}Sr$ mixture as a function of laser frequency ν is

$$R(\nu) = \int d^3r\, \kappa \left(n_{88}(r)^2 \mathcal{F}(\nu - \nu_0^{(88-88)}) + n_{88}(r) n_{84}(r) \mathcal{F}(\nu - \nu_0^{(88-84)}) \right) \qquad (5.4)$$

where $n_x(r)$ is the number density distribution for each isotope, $\mathcal{F}(\nu - \nu_0)$ is a

lineshape function with unit integral centered at laser frequency ν_0, and κ is a rate constant that is a function of isotope-independent quantities such as electronic matrix elements, laser power, and other experimental parameters that are held fixed here. The Bose-enhancement of the homonuclear RM excitation rate [70] is about 10% for $n = 39$ at these temperatures and is neglected in our analysis.

Frequency integration over the line shape gives the integrated rate, $\mathcal{S}$,

$$\mathcal{S} = \int d\nu\, R(\nu) = \kappa(n_{0,88}^2 + n_{0,88}n_{0,84})\, V. \tag{5.5}$$

For a harmonic trap the effective volume that arises from the integration of the spatial density distribution is

$$V = \left(\frac{\pi k_B T}{m\bar{\omega}^2}\right)^{3/2} \tag{5.6}$$

with geometric mean of the trap frequencies $\bar{\omega}$ and the spatial density distribution $n_x(r)$ is assumed to be a Gaussian with the peak density $n_{0,x}$ for each isotope. The effective volume is, in principle, isotope dependent, but when the effective volumes for each isotope are calculated we find that they are equal to within 10% over all of the densities considered and we assume these volumes as equal. We normalize the integrated rate $\mathcal{S}$ by $n_{0,88}^2 V$ to obtain a relation that is a function of the ratio of the two isotope densities.

$$\frac{\mathcal{S}}{V\, n_{0,88}^2} = \kappa\left(1 + \frac{n_{0,84}}{n_{0,88}}\right). \tag{5.7}$$

We obtain RM excitation spectra in $^{88}\mathrm{Sr} + {}^{84}\mathrm{Sr}$ mixtures where we vary the ratio of ^{88}Sr density to ^{84}Sr density from 0.03 to 1 as discussed above. We scan the laser detuning over a range that includes both the $^{88}\mathrm{Sr}^* + {}^{88}\mathrm{Sr}$ and $^{88}\mathrm{Sr}^* + {}^{84}\mathrm{Sr}$ lines and integrate the spectrum. The integrated spectra are normalized according to Equation 5.7 and fitted with a single constant, κ. As shown in Figure 5.4, the measured data

are well described by this scaling relation. For the lowest ^{88}Sr fraction, we have a heteronuclear production fidelity of about 30 to 1. This fidelity is only a lower bound, however, as we have integrated over the entire spectrum and neglected any spectral selectivity. We can easily improve the heteronuclear excitation fidelity if spectral resolution is utilized, even for $n = 39$.

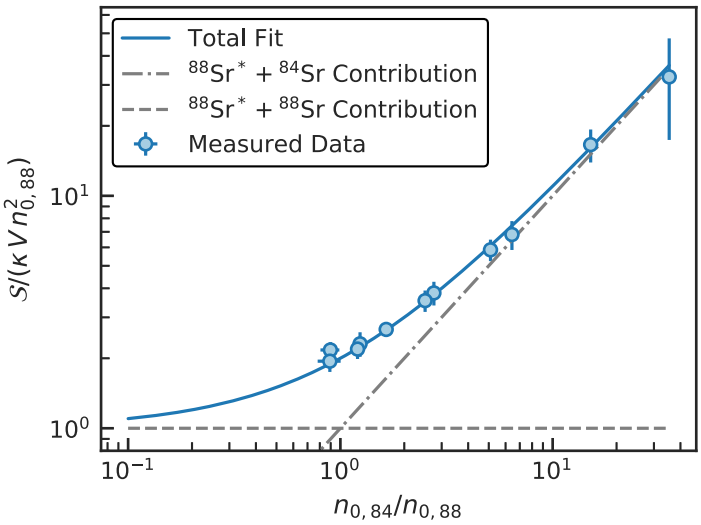

Figure 5.4 : The scaling of normalized Rydberg molecule signal with density. The blue points are integrated Rydberg molecule signals normalized by the density of ^{88}Sr and and fitted to the scaling relation given in Equation 5.7 with a single constant of proportionality (blue line). The grey dashed and dot-dashed lines represent the individual contributions to the signal from $^{88}\mathrm{Sr} + {}^{88}\mathrm{Sr}$ pairs and $^{88}\mathrm{Sr} + {}^{84}\mathrm{Sr}$ pairs respectively. It is clear that both terms are required to accurately explain the behavior of the molecular excitation rate.

In summary, we have observed the excitation of heteronuclear Rydberg molecules in a mixture of $^{88}\mathrm{Sr} + {}^{84}\mathrm{Sr}$. The presence of an isotope shift provides clear evidence of the creation of heteronuclear molecules, and the dependence of the integrated RM

spectrum on the relative densities is well described by a model incorporating heteronuclear and homonuclear production. When the isotope shift is large compared to the spectral linewidth, essentially pure samples of heteronuclear molecules can be created. In the limit of unresolved lines, we have demonstrated homonuclear impurity below 1 part in 30. Heteronuclear RMs present many new opportunities for studying quantum systems such as probing interparticle and interspecies pair correlation functions in multi-component many body systems [93, 94] using the methods of [70]. We can probe the scattering wavefunction of a strongly interacting mixture such as the $^{88}\mathrm{Sr} + {}^{84}\mathrm{Sr}$ combination used in this work. Such an *in situ* measurement of the pair-correlation function in the presence of strong interactions can be related to the Tan contact [95, 96], and the temporal resolution available with RM excitation could provide a probe of the dynamics of the contact after an interaction quench. This new variety of RMs opens paths to explore the sensitivity of the isotope shift to the mass polarization energy for Rydberg trimers or larger molecules, and RMs involving high L Rydberg states. In lighter atomic species, e.g. Li, the isotope shift is expected to be much larger than observed in this work [88]. Heteronuclear RMs could also enable studies of new types of Rydberg impurities in quantum gases [97]. Very recent work in bialkali mixtures of K and Cs have shown that heteronuclear RMs can be used to benchmark theoretical models of electron-atom scattering [28].

5.2 Estimation of the isotope shift

In the previous paper observation of an isotope shift in the binding energy of the $\nu = 0$ RM provided clear indication that heteronuclear RMs were being excited. To be sure that the observed shift was due to the mass difference we estimated the size of the isotope shift using a simple model. The $\nu = 0$ RM state is highly localized in the outer well of the RM potential, which can therefore be approximated as harmonic, i.e.

$$V(R) \approx \frac{1}{2}k(R - R_c)^2 + \mathcal{O}(R^4) \tag{5.8}$$

where R_c is the location of the potential minimum and k is the "spring constant" of the potential, which is related to the characteristic frequency $\omega = \sqrt{k/\mu}$ (μ is the reduced mass). The value of k can be estimated using a numerical derivative of the potential curves provided by Shuhei Yoshida, $k = 2V''(R_c)$. A picture of this procedure can be found in Figure 5.5.

The observed shift is in the binding energy of the $\nu = 0$ level, which is measured relative to the atomic line. Under the harmonic approximation the binding energy is

$$E_b = V_{min} + \hbar\omega/2. \tag{5.9}$$

V_{min} is the minimum of the RM potential, which is independent of isotope. We can therefore estimate the binding energy shift as

$$E_b^{(84-88)} - E_b^{(88-88)} = \hbar\omega_{84-88}/2 - \hbar\omega_{88-88}/2 = \frac{\hbar}{2}\Delta\omega. \tag{5.10}$$

The shift of ω can be estimated as

$$\omega(\mu + \Delta\mu) = \omega(\mu) + \frac{d\omega}{d\mu}\Delta\mu \tag{5.11}$$

$$\Rightarrow \frac{\Delta\omega}{\omega} = -\frac{1}{2}\frac{\Delta\mu}{\mu}, \tag{5.12}$$

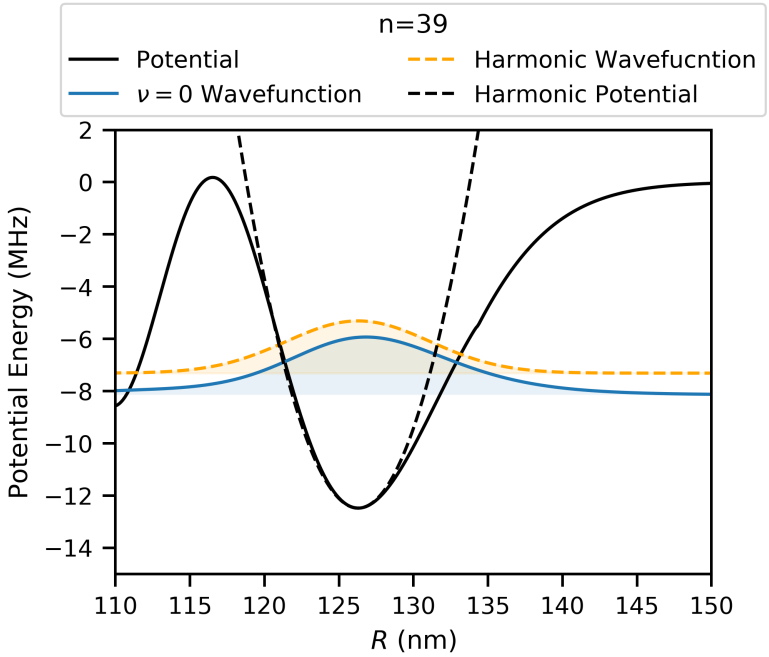

Figure 5.5 : The harmonic approximation of the RM potential for the $5s39s\,^3S_1$ state. The solid lines are the Rydberg potential and $\nu = 0$ wavefunction, and the dashed lines represent the potential and wavefunction under the harmonic approximation. Given the crude nature of the approximation, the agreement is reasonable.

which for a mass difference of $^{88}\mathrm{Sr} + {}^{88}\mathrm{Sr}$ to $^{88}\mathrm{Sr} + {}^{84}\mathrm{Sr}$ is about 1%. From Figure 5.5 we can estimate that $\omega \sim 10\,\mathrm{MHz}$ and therefore $\Delta\omega \sim 100\,\mathrm{kHz}$ for $n = 39$. Using equation 5.10 we can see that the expected isotope shift is $\sim 50\,\mathrm{kHz}$ which is consistent with the data presented in Figure 5.3.

5.3 Scaling of the isotope shift with n

We can repeat the harmonic approximation for a few values of n and extract an isotope shift. In doing this we find that the isotope shift of the $\nu = 0$ RM level scales

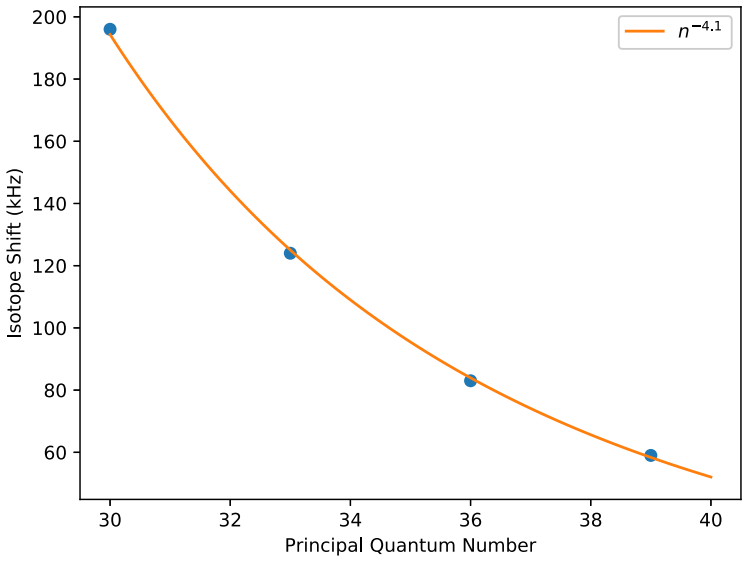

Figure 5.6 : The isotope shift $E_b^{(84-88)} - E_b^{(88-88)}$ calculated using the harmonic approximation discussed in the previous section. The calculated points are fitted to a power law that gives a scaling of $(n - \delta_\ell)^{-4.1}$.

with $n - \delta_\ell$ as $(n - \delta_\ell)^{-4.1}$ as shown in Figure 5.6.

We can use a simple argument to rationalize this observed scaling. The RM potential follows the shape of the $5sns\,^3S_1$ wavefunction, which has $N \simeq n$ nodes, and the size of the Rydberg orbital is $R_n \sim 2(n-\delta_\ell)^2$. Therefore, the width w of the outer well scales as $N/R_n \sim n$. The depth of the well is proportional to the electron density, which scales as n^{-6}. The characteristic frequency of the potential can be approximated as $\mu\omega^2 w^2 = d$, implying $\omega \sim n^{-4}$. The isotope shift is proportional to ω, so therefore the isotope shift should scale the same with n, which agrees with the harmonic approximation data in Figure 5.6 and the experimental observations in Figure 5.5.

Chapter 6

Conclusion

In this thesis we presented a study of the relationship between the excitation of RMs to the pair correlation $g^{(2)}(R)$ of cold gases and produced heteronuclear RMs. To do this we developed experimental techniques for laser cooling and trapping $^{84}\mathrm{Sr} + {}^{87}\mathrm{Sr}$ and $^{88}\mathrm{Sr} + {}^{84}\mathrm{Sr}$ mixtures and built a new optical dipole trap. We improved the UV laser system to be able to scan the UV laser frequency to any Rydberg state and create Rydberg atoms and molecules in all Sr isotopes. Spin-polarized samples of $^{87}\mathrm{Sr}$ were produced and characterized using Rydberg spectroscopy.

We showed in [70] that the RM excitation rate is directly related to the pair correlation function by measuring the ratio of $^{84}\mathrm{Sr}$ and spin-polarized $^{87}\mathrm{Sr}$ to unpolarized samples of $^{87}\mathrm{Sr}$. In this work we derived the equation for the excitation rate of RMs, and determined the dependence of the excitation rate on the cloud density, laser intensity and other experimental factors to extract $g^{(2)}(R)$ from the experimental data.

In [30] we produced some of the first observations of heteronuclear RMs. The purpose of this work was to take a step toward studying strongly interacting mixtures of $^{84}\mathrm{Sr} + {}^{88}\mathrm{Sr}$ using the methods of [70]. We observed and isotope shift of the $\nu = 0$ RM, and derived a simple scaling relationship that describes the observations reasonably. We also derived equations for the density distributions, and the scaling of the heteronuclear RM excitation rate with the densities of $^{88}\mathrm{Sr}$ and $^{84}\mathrm{Sr}$. We used these scalings to determine the fidelity of heteronuclear RM production.

Several studies expanding on the work presented here are currently underway on the Rydberg apparatus. We are measuring the RM excitation rate in a Bose-Einstein condensate of ^{84}Sr where the pair correlation function should have no structure; in this experiment the effect of Poisson statistics should play a role. We are also studying a strongly interacting gases of ^{86}Sr and $^{84}\mathrm{Sr} + {}^{88}\mathrm{Sr}$ comparing the extracted $g^{(2)}(R)$ to the weakly interacting ^{84}Sr data shown in [70]. The addition of an optical lattice is also underway. We will use the techniques in this thesis to probe strongly interacting one-dimensional gases created using the optical lattice.

Appendices

Appendix A

Calculation of $g^{(2)}(R)$

To derive the $g^{(2)}(R)$ expressions used in this work we will follow the work of Narachewski and Glauber [36]. First we consider the most general expression of the first- and second-order correlation functions in terms of the field operators $\hat{\Psi}(\mathbf{r})$ and $\hat{\Psi}^{\dagger}(\mathbf{r})$, where $\hat{\Psi}(\mathbf{r})$ destroys a particle at position $\mathbf{r}$ and $\hat{\Psi}^{\dagger}(\mathbf{r})$ creates a particle at $\mathbf{r}$. The correlation functions are then

$$G^{(1)}(\mathbf{r},\mathbf{r}') = \langle \hat{\Psi}^{\dagger}(\mathbf{r})\hat{\Psi}(\mathbf{r}')\rangle \tag{A.1}$$

$$G^{(2)}(\mathbf{r},\mathbf{r}') = \langle \hat{\Psi}^{\dagger}(\mathbf{r})\hat{\Psi}^{\dagger}(\mathbf{r}')\hat{\Psi}(\mathbf{r}')\hat{\Psi}(\mathbf{r})\rangle. \tag{A.2}$$

The field operators are, in principle, also functions of time but here we are considering correlation functions at equal time, so we need not consider time ordering in this case. The ordering of the operators is very important to ensure generality in cases where operators at different positions do not commute, such as for fermions. Further, normal ordering ensures that the expectation value of the vacuum state $|0\rangle$ is identically zero.

The general strategy for calculating these types of expectation values is to factorize them into products of number operators, i.e. $\langle \hat{\Psi}^{\dagger}(\mathbf{r})\hat{\Psi}(\mathbf{r}')\rangle$, which are easily evaluated and allow us to only do one calculation to be able to calculate any order correlation function. In the cases presented here the properties of the commutators of the field values determines the behavior of these correlations. To this end we

define a general commutator

$$\left[\hat{A},\hat{B}\right]_\eta = \hat{A}\hat{B} - \eta\hat{B}\hat{A} \tag{A.3}$$

where η is $+1$ for bosons, and -1 for fermions. The field operators obey the following commutation relations

$$\left[\hat{\Psi}(\mathbf{r}),\hat{\Psi}^\dagger(\mathbf{r}')\right]_\eta = \delta(\mathbf{r}-\mathbf{r}') \tag{A.4}$$

$$\left[\hat{\Psi}(\mathbf{r}),\hat{\Psi}(\mathbf{r}')\right]_\eta = 0 \tag{A.5}$$

We can attempt to factorize the expression for $G^{(2)}(\mathbf{r},\mathbf{r}')$ but quickly find that

$$\langle\hat{\Psi}^\dagger(\mathbf{r})\hat{\Psi}^\dagger(\mathbf{r}')\hat{\Psi}(\mathbf{r}')\hat{\Psi}(\mathbf{r})\rangle = \langle\hat{\Psi}^\dagger(\mathbf{r})\hat{\Psi}(\mathbf{r})\hat{\Psi}^\dagger(\mathbf{r}')\hat{\Psi}(\mathbf{r}')\rangle - \delta(\mathbf{r}-\mathbf{r}')\langle\hat{\Psi}^\dagger(\mathbf{r})\hat{\Psi}(\mathbf{r}')\rangle \tag{A.6}$$

which is not simply in terms of products of $G^{(1)}(\mathbf{r},\mathbf{r}')$. Instead we must consider the definition of the field operators in the momentum basis, which is appropriate for a homogeneous system. The field operators can be expressed in the momentum basis as

$$\hat{\Psi}(\mathbf{r}) = \sum_{\mathbf{k}} \mathbf{u}_{\mathbf{k}}(\mathbf{r})a_{\mathbf{k}} \tag{A.7}$$

where $\mathbf{u}_{\mathbf{k}}(\mathbf{r})$ is the spatial representation of the momentum eigenstate $|\mathbf{k}\rangle$, i.e. $\langle\mathbf{r}|\mathbf{k}\rangle$. The momentum creation and annihilation operators a and $a^\dagger$ obey the standard commutation relations

$$\left[a_{\mathbf{k}},a^\dagger_{\mathbf{k}'}\right]_\eta = \delta_{\mathbf{k},\mathbf{k}'} \tag{A.8}$$

$$\left[a_{\mathbf{k}},a_{\mathbf{k}'}\right]_\eta = 0 \tag{A.9}$$

which are consistent with the commutation relations for the field operators in the thermodynamic limit.

The expression for $G^{(2)}(\mathbf{r},\mathbf{r}')$ can be written in terms of the momentum basis as

$$\langle\hat{\Psi}^\dagger(\mathbf{r})\hat{\Psi}^\dagger(\mathbf{r}')\hat{\Psi}(\mathbf{r}')\hat{\Psi}(\mathbf{r})\rangle = \sum_{\mathbf{klmn}} \mathbf{u}^*_{\mathbf{k}}(\mathbf{r})\mathbf{u}^*_{\mathbf{l}}(\mathbf{r}')\mathbf{u}_{\mathbf{m}}(\mathbf{r}')\mathbf{u}_{\mathbf{n}}(\mathbf{r})\langle a^\dagger_{\mathbf{k}}a^\dagger_{\mathbf{l}}a_{\mathbf{m}}a_{\mathbf{n}}\rangle \tag{A.10}$$

where we can immediately see that there are only three combinations of $\mathbf{k}$, $\mathbf{l}$, $\mathbf{m}$, and $\mathbf{n}$ that give a nonzero expectation value: (1) $\mathbf{k}=\mathbf{n}$, $\mathbf{l}=\mathbf{m}$, $\mathbf{k}\neq\mathbf{l}$, (2) $\mathbf{k}=\mathbf{m}$, $\mathbf{l}=\mathbf{n}$, $\mathbf{k}\neq\mathbf{l}$ and (3) $\mathbf{k}=\mathbf{l}=\mathbf{m}=\mathbf{n}$. Using this we can rewrite the sum as

$$\begin{aligned}\langle\hat{\Psi}^\dagger(\mathbf{r})\hat{\Psi}^\dagger(\mathbf{r}')\hat{\Psi}(\mathbf{r}')\hat{\Psi}(\mathbf{r})\rangle = \\ \sum_{\mathbf{k}\neq\mathbf{l}} \mathbf{u}^*_{\mathbf{k}}(\mathbf{r})\mathbf{u}^*_{\mathbf{l}}(\mathbf{r}')\mathbf{u}_{\mathbf{m}}(\mathbf{r}')\mathbf{u}_{\mathbf{n}}(\mathbf{r})\left[\langle a^\dagger_{\mathbf{k}}a^\dagger_{\mathbf{l}}a_{\mathbf{l}}a_{\mathbf{k}}\rangle\delta_{\mathbf{k},\mathbf{n}}\delta_{\mathbf{l},\mathbf{m}} + \langle a^\dagger_{\mathbf{k}}a^\dagger_{\mathbf{l}}a_{\mathbf{k}}a_{\mathbf{l}}\rangle\delta_{\mathbf{k},\mathbf{m}}\delta_{\mathbf{l},\mathbf{n}}\right] \\ + \sum_{\mathbf{k}} |\mathbf{u}_{\mathbf{k}}(\mathbf{r})|^2|\mathbf{u}_{\mathbf{k}}(\mathbf{r}')|^2\langle a^\dagger_{\mathbf{k}}a^\dagger_{\mathbf{k}}a_{\mathbf{k}}a_{\mathbf{k}}\rangle.\end{aligned} \tag{A.11}$$

Using the commutation relations for the momentum operators we can evaluate each expectation value

$$\langle a^\dagger_{\mathbf{k}}a^\dagger_{\mathbf{l}}a_{\mathbf{l}}a_{\mathbf{k}}\rangle = \langle a^\dagger_{\mathbf{k}}a_{\mathbf{k}}\rangle\langle a^\dagger_{\mathbf{l}}a_{\mathbf{l}}\rangle - \delta_{\mathbf{k},\mathbf{l}}\langle a^\dagger_{\mathbf{k}}a_{\mathbf{l}}\rangle \tag{A.12}$$

$$\langle a^\dagger_{\mathbf{k}}a^\dagger_{\mathbf{l}}a_{\mathbf{k}}a_{\mathbf{l}}\rangle = \eta\left(\langle a^\dagger_{\mathbf{k}}a_{\mathbf{k}}\rangle\langle a^\dagger_{\mathbf{l}}a_{\mathbf{l}}\rangle - \delta_{\mathbf{k},\mathbf{l}}\langle a^\dagger_{\mathbf{k}}a_{\mathbf{l}}\rangle\right) \tag{A.13}$$

and insert them into the sums. The stipulation that $\mathbf{k}\neq\mathbf{l}$ removes the $\delta_{\mathbf{k},\mathbf{l}}$ terms.

$$\begin{aligned}\langle\hat{\Psi}^\dagger(\mathbf{r})\hat{\Psi}^\dagger(\mathbf{r}')\hat{\Psi}(\mathbf{r}')\hat{\Psi}(\mathbf{r})\rangle = \\ \sum_{\mathbf{k}\neq\mathbf{l}} |\mathbf{u}_{\mathbf{k}}(\mathbf{r})|^2|\mathbf{u}_{\mathbf{l}}(\mathbf{r}')|^2\langle a^\dagger_{\mathbf{k}}a_{\mathbf{k}}\rangle\langle a^\dagger_{\mathbf{l}}a_{\mathbf{l}}\rangle + \eta\,\mathbf{u}^*_{\mathbf{k}}(\mathbf{r})\mathbf{u}_{\mathbf{l}}(\mathbf{r}')\mathbf{u}_{\mathbf{k}}(\mathbf{r}')\mathbf{u}^*_{\mathbf{l}}(\mathbf{r})\langle a^\dagger_{\mathbf{k}}a_{\mathbf{k}}\rangle\langle a^\dagger_{\mathbf{l}}a_{\mathbf{l}}\rangle \\ + \sum_{\mathbf{k}} |\mathbf{u}_{\mathbf{k}}(\mathbf{r})|^2|\mathbf{u}_{\mathbf{k}}(\mathbf{r}')|^2\langle a^\dagger_{\mathbf{k}}a^\dagger_{\mathbf{k}}a_{\mathbf{k}}a_{\mathbf{k}}\rangle.\end{aligned} \tag{A.14}$$

Recalling that the field operators are defined as a sum over *all* $\mathbf{k}$ we add and subtract two factors of $|\mathbf{u}_{\mathbf{k}}(\mathbf{r})|^2|\mathbf{u}_{\mathbf{k}}(\mathbf{r}')|^2\langle a^\dagger_{\mathbf{k}}a_{\mathbf{k}}\rangle\langle a^\dagger_{\mathbf{k}}a_{\mathbf{k}}\rangle$, one for each term in the $\mathbf{k}\neq\mathbf{l}$ sum. With

this we can now substitute the field operators.

$$\langle\hat{\Psi}^\dagger(\mathbf{r})\hat{\Psi}^\dagger(\mathbf{r}')\hat{\Psi}(\mathbf{r}')\hat{\Psi}(\mathbf{r})\rangle = \langle\hat{\Psi}^\dagger(\mathbf{r})\hat{\Psi}(\mathbf{r})\rangle\langle\hat{\Psi}^\dagger(\mathbf{r}')\hat{\Psi}(\mathbf{r}')\rangle + \eta\left|\langle\hat{\Psi}^\dagger(\mathbf{r})\hat{\Psi}(\mathbf{r}')\rangle\right|^2 + \sum_{\mathbf{k}}|\mathbf{u}_{\mathbf{k}}(\mathbf{r})|^2|\mathbf{u}_{\mathbf{k}}(\mathbf{r}')|^2\left(\langle a^\dagger_{\mathbf{k}}a^\dagger_{\mathbf{k}}a_{\mathbf{k}}a_{\mathbf{k}}\rangle - 2\langle a^\dagger_{\mathbf{k}}a_{\mathbf{k}}\rangle\langle a^\dagger_{\mathbf{k}}a_{\mathbf{k}}\rangle\right) \quad \text{(A.15)}$$

It should be noted that the second line in the above equation only appears for bosons or classical particles because the maximum occupation number for any fermion state is limited to 1, i.e. $a_{\mathbf{k}}a_{\mathbf{k}}|k\rangle = 0$ and the case where all momentum indices are equal is forbidden. With the form we have derived we can already see the impact of particle statistics on the pair-correlation function. When $\mathbf{r} = \mathbf{r}'$ $G^{(2)}$ goes to zero for fermions ($\eta = -1$), and is enhanced for bosons as expected.

Since we have shown that we can factor $G^{(2)}$ into factors of $G^{(1)}$ we can get away with only doing a single calculation to get $G^{(2)}$. We can take the expectation value: $\langle\hat{\Psi}^\dagger(\mathbf{r})\hat{\Psi}(\mathbf{r}')\rangle$. The state we will use to take the expectation value is a thermal state $|\phi\rangle = \sum_{\mathbf{k}} n_{\mathbf{k}}|\mathbf{k}\rangle$ where $n_{\mathbf{k}}$ is the occupation number for mode $\mathbf{k}$ and $\sum_{\mathbf{k}} n_{\mathbf{k}} = N$, the total particle number. Using plane-waves as our choice of basis we have

$$\hat{\Psi}(\mathbf{r}) = \int d^3k\, \psi_{\mathbf{k}}(\mathbf{r})a_{\mathbf{k}} = \int d^3k\, e^{i\mathbf{k}\cdot\mathbf{r}}a_{\mathbf{k}}.$$

The expectation value is then

$$\langle\hat{\Psi}^\dagger(\mathbf{r})\hat{\Psi}(\mathbf{r}')\rangle = \langle\phi|\int d^3k \int d^3q\, e^{-i\mathbf{k}\cdot\mathbf{r}'}e^{i\mathbf{q}\cdot\mathbf{r}}a^\dagger_{\mathbf{k}}a_{\mathbf{q}}|\phi\rangle.$$

Using $\langle\phi|a^\dagger_{\mathbf{k}}a_{\mathbf{q}}|\phi\rangle = n_{\mathbf{k}}\delta(\mathbf{k}-\mathbf{q})$

$$\langle\hat{\Psi}^\dagger(\mathbf{r})\hat{\Psi}(\mathbf{r}')\rangle = \int d^3k\, e^{i\mathbf{k}\cdot\mathbf{R}}n_{\mathbf{k}}.$$

where $\mathbf{R} = \mathbf{r} - \mathbf{r}'$. For a thermal state

$$n_{\mathbf{k}} = \left(\frac{\hbar^2}{2\pi m k_B T}\right)^{3/2} e^{-\frac{\hbar^2k^2}{2mk_BT}}$$

Expand $e^{i\mathbf{k}\cdot\mathbf{R}}$ in partial waves

$$\langle\hat{\Psi}^\dagger(\mathbf{r})\hat{\Psi}(\mathbf{r}')\rangle = \left(\frac{\hbar^2}{2\pi m k_B T}\right)^{3/2}\int_0^\infty dk\, k^2 \int_{\Omega_k} d\Omega_k\, 4\pi \sum_L \sum_{M=-L}^{L} Y_L^M(\hat{k})^* Y_L^M(\hat{R}) i^L j_L(kR) e^{-\frac{\hbar^2 k^2}{2mk_BT}}$$

after angular integration over Ω_k only $L = 0$ is allowed ($Y_0^0 = 1/\sqrt{4\pi}$):

$$\langle\hat{\Psi}^\dagger(\mathbf{r})\hat{\Psi}(\mathbf{r}')\rangle = 4\pi\left(\frac{\hbar^2}{2\pi m k_B T}\right)^{3/2}\int_0^\infty dk\, k^2 j_0(kR) e^{-\hbar^2k^2/2mk_BT} = e^{-\pi R^2/\lambda_{dB}^2}$$

where λ_{dB} is the thermal de Broglie wavelength $\lambda_{dB} = h/\sqrt{2\pi m k_B T}$. Using the factorized expression for $g^{(2)}(R)$in Equation A.15 we can find that

$$\langle\hat{\Psi}^\dagger(\mathbf{r})\hat{\Psi}^\dagger(\mathbf{r}')\hat{\Psi}(\mathbf{r}')\hat{\Psi}(\mathbf{r}')\rangle = 1 + \eta e^{-2\pi R^2/\lambda_{dB}^2} \tag{A.16}$$

where η is 1 for identical bosons, -1 for identical fermions and 0 for distinguishable particles.

Appendix B

The effect of Poisson statistics on RM Production

In general, one must take into account the poisson statistics of partitioning N atoms into V/R_n domains when considering the excitation of rydberg molecules. In order to create a Rydberg oligomer of order p (dimer $p = 2$, trimer $p = 3$ etc) not only must there be p atoms present within the Rydberg orbital but also there must be *exclusively* p atoms within the orbital.

When a classical gas of particles with density n and volume V is partitioned in to domains of volume $V_R = (4/3)\pi R_n^3$ where $R_n = 2(n-\delta)^2$, the distribution of atom number per domain is given by Poisson statistics, i.e.

$$P_N(r) = \frac{(n(r)V_R)^N e^{-n(r)V_R}}{N!} \tag{B.1}$$

For dimers $N = 1$, and one can see clearly that as nV_R, the number of atoms per volume V_R, increases the likelihood of finding exactly one particle per V_R will decrease.

To take this into account we must consider the probability of excitation of an order p oligomer. First, an atom must be excited to the Rydberg state. The probability of this excitation is simply proportional to the density. Next, in order to excite the p-mer there must be exactly $p-1$ atoms within the volume of interest. The excitation rate is then the product of the two probabilities integrated over space

$$R_p(r) = \int d^3r\, \kappa\, n(r) \frac{(n(r)V_R)^{p-1} e^{n(r)V_R}}{(p-1)!} \tag{B.2}$$

where $V_R = 4/3\pi R_n^3$. Now we must tackle this integral to get something meaningful.

First we will use the spherical symmetry of the density distribution to reduce the integral to

$$R_p = 4\pi \int_0^\infty dr\, r^2\, \kappa\, n(r) \frac{(n(r)V_R)^{p-1}\, e^{-n(r)V_R}}{(p-1)!} \tag{B.3}$$

Then we make a substitution using

$$n(r) = n_0 \exp\left(-\frac{m\omega^2 r^2}{2k_B T}\right) \tag{B.4}$$

$$dn = -n_0 \frac{m\omega^2}{k_B T} r \exp\left(-\frac{m\omega^2 r^2}{2k_B T}\right) dr \tag{B.5}$$

and substitute r with

$$r = \sqrt{\ln\left(\frac{n_0}{n}\right) \frac{2k_B T}{m\omega^2}} \tag{B.6}$$

and rewrite dn

$$dn = \left(\frac{2m\omega^2}{k_B T}\right)^{1/2} \sqrt{\ln\left(\frac{n_0}{n}\right)}\, n\, dr \tag{B.7}$$

now the integral in Eq. B.3 can be written as

$$R_p = \left(\frac{2\pi k_B T}{m\omega^2}\right)^{3/2} \int_0^{n_0} dn\, \kappa \sqrt{\ln\left(\frac{n_0}{n}\right)} \frac{(nV_R)^{p-1} e^{-nV_R}}{(p-1)!} \tag{B.8}$$

to evaluate this integral we perform a power series expansion on the exponential in the integrand

$$R_p = \left(\frac{2\pi k_B T}{m\omega^2}\right)^{3/2} \sum_{k=0}^{\infty} \int_0^{n_0} dn\, \kappa \sqrt{\ln\left(\frac{n_0}{n}\right)} \frac{(nV_R)^{p-1}(-nV_R)^k}{(p-1)!\, k!} \tag{B.9}$$

which can be evaluated in Mathematica to find

$$R_p = \kappa\, n_0^p \left(\frac{2\pi k_B T}{m\omega^2}\right)^{3/2} \frac{V_R^{p-1}}{(p-1)!} \sum_{k=0}^{\infty} \frac{(-n_0 V_R)^k}{(k+p)^{3/2}\, k!} \tag{B.10}$$

Which gives the correct density dependence. The terms after n_0^p can be considered as an n-dependent effective volume.

$$V_p = \left(\frac{2\pi k_B T}{m\omega^2}\right)^{3/2} \frac{V_R^{p-1}}{(p-1)!} \sum_{k=0}^{\infty} \frac{(-n_0 V_R)^k}{(k+p)^{3/2}\, k!} \tag{B.11}$$

Appendix C

Optical dipole trap

C.1 Beam Profile

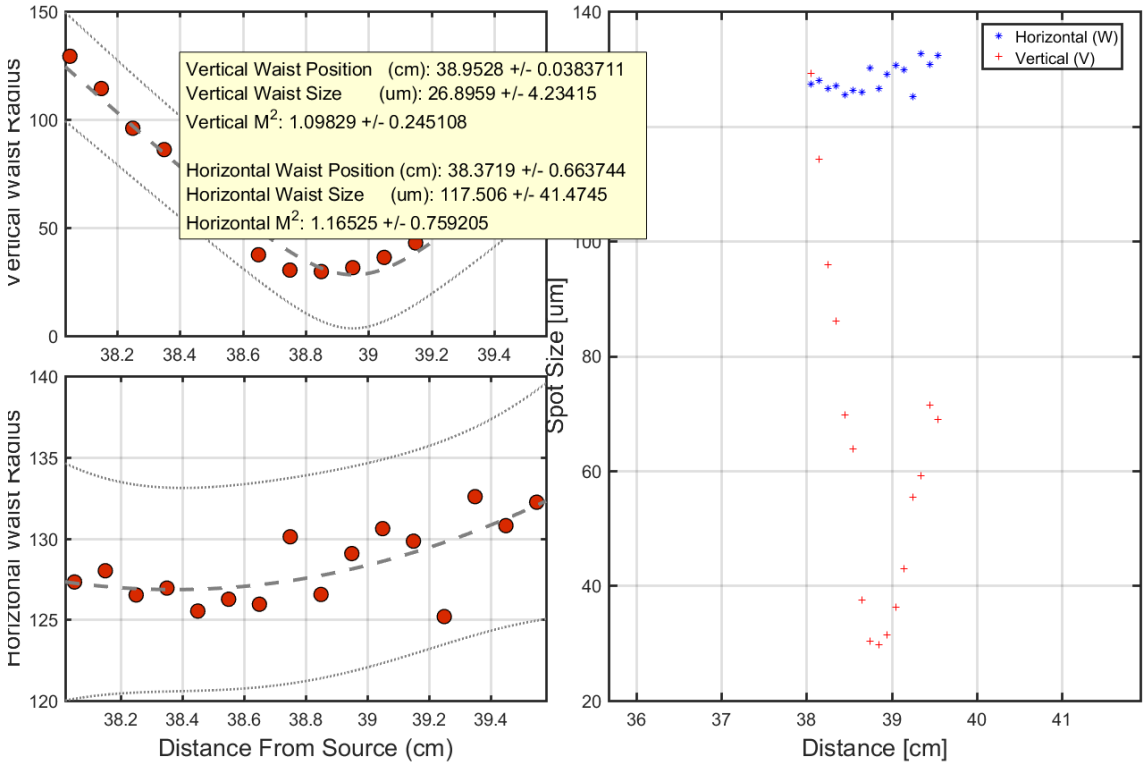

Figure C.1 : The beam profile of the second sheet trap.

C.2 Bill of materials

Table C.1 : The bill of materials for the second sheet trap assembly.

Product Number	Description
Thorlabs PT-1	Translation stage
Thorlabs CRM1L	4x rotation mounts for lenses and half-wavepalte
Thorlabs CCM1-PBS25-1064-HP/M	Mounted PBS Cube
Thorlabs KC1-T	SM1-Threaded Kinematic Mount for fiber collimator
Thorlabs CP02B	2x 30 mm cage mounting brackets
Thorlabs ER 12	4x 6 mm dia x 12” long cage rods cut into 9” and 3” sections
Thorlabs LK4349RM-C	-50 mm cylindrical lens
Thorlabs LJ4643RM-C	150 mm cylindrical lens
Thorlabs LJ4377RM-C	400 mm cylindrical lens
Thorlabs AD11F	Modified SM1 outer thread collimator holder for 11mm dia optics
OZ Optics PMJ-A3AHPCA3AHPC-1064-6/125-3-AS-3-1 S/N T2353041-01	Fiber
OZ Optics PMJ-A3AHPCA3AHPC-1064-6/125-3-AS-3-1 S/N T2353041-01	Collimator
Thorlabs RS05P8E	4x 1” dia x 0.5” long pedestal mounts
Lambda WPOM-25.4-10.0CQ-0-2-1064	Half-waveplate

C.3 Mechanical drawings

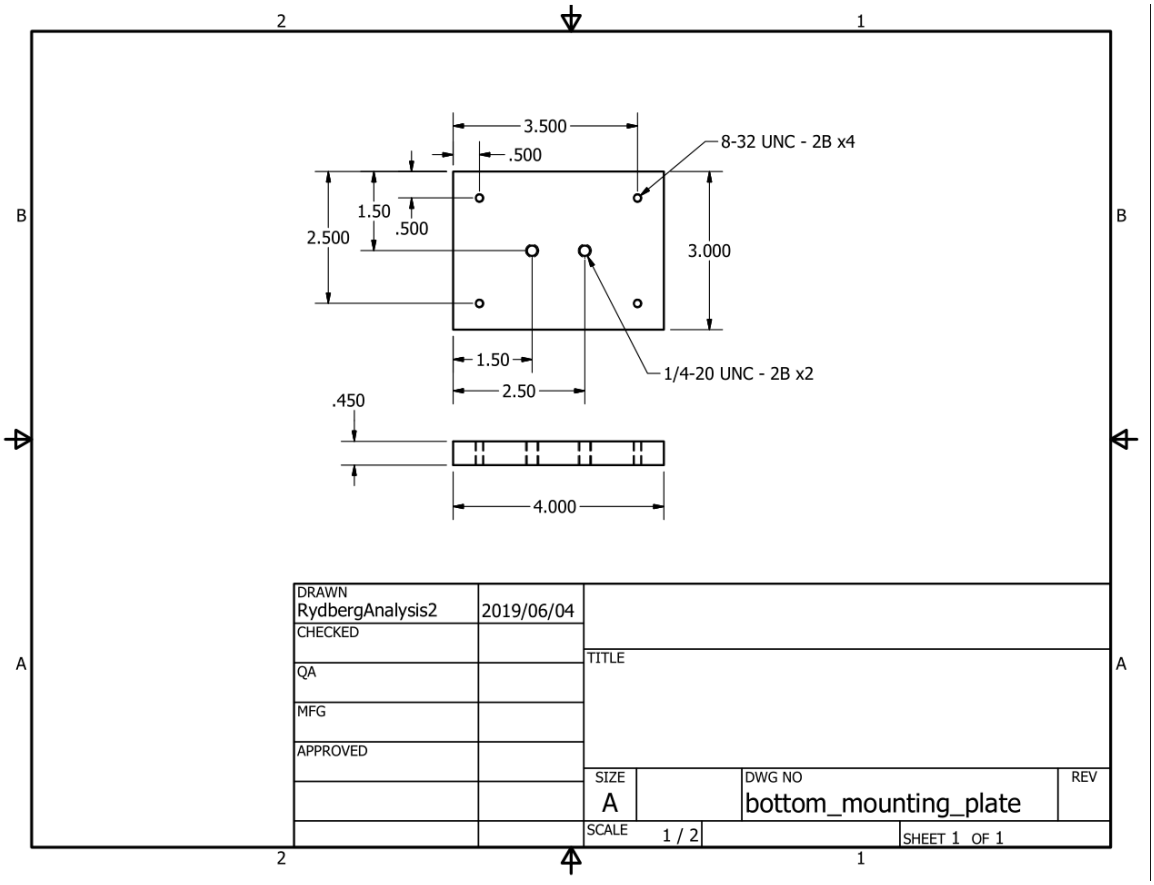

Figure C.2 : Mechanical drawing of the bottom mounting plate of the second sheet trap assembly.

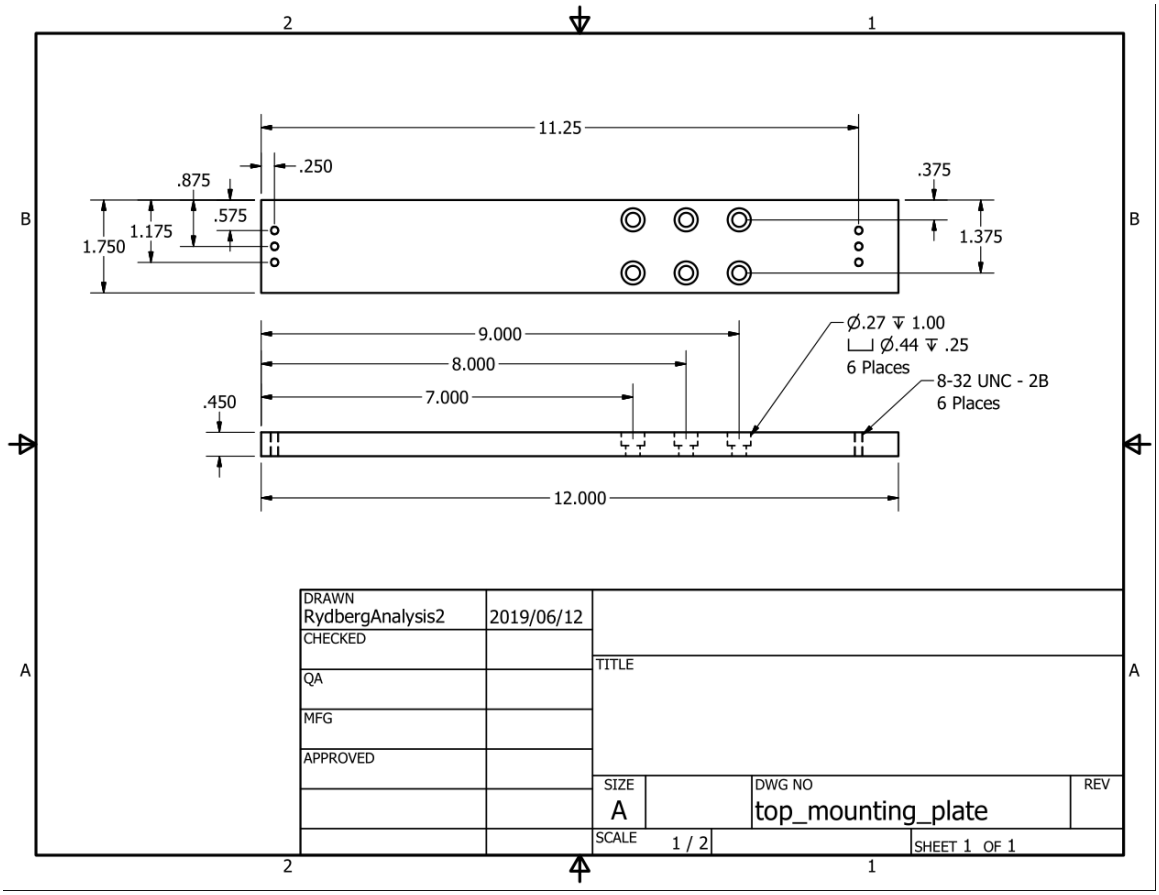

Figure C.3 : Mechanical drawing of the top mounting plate for the second sheet trap assembly.

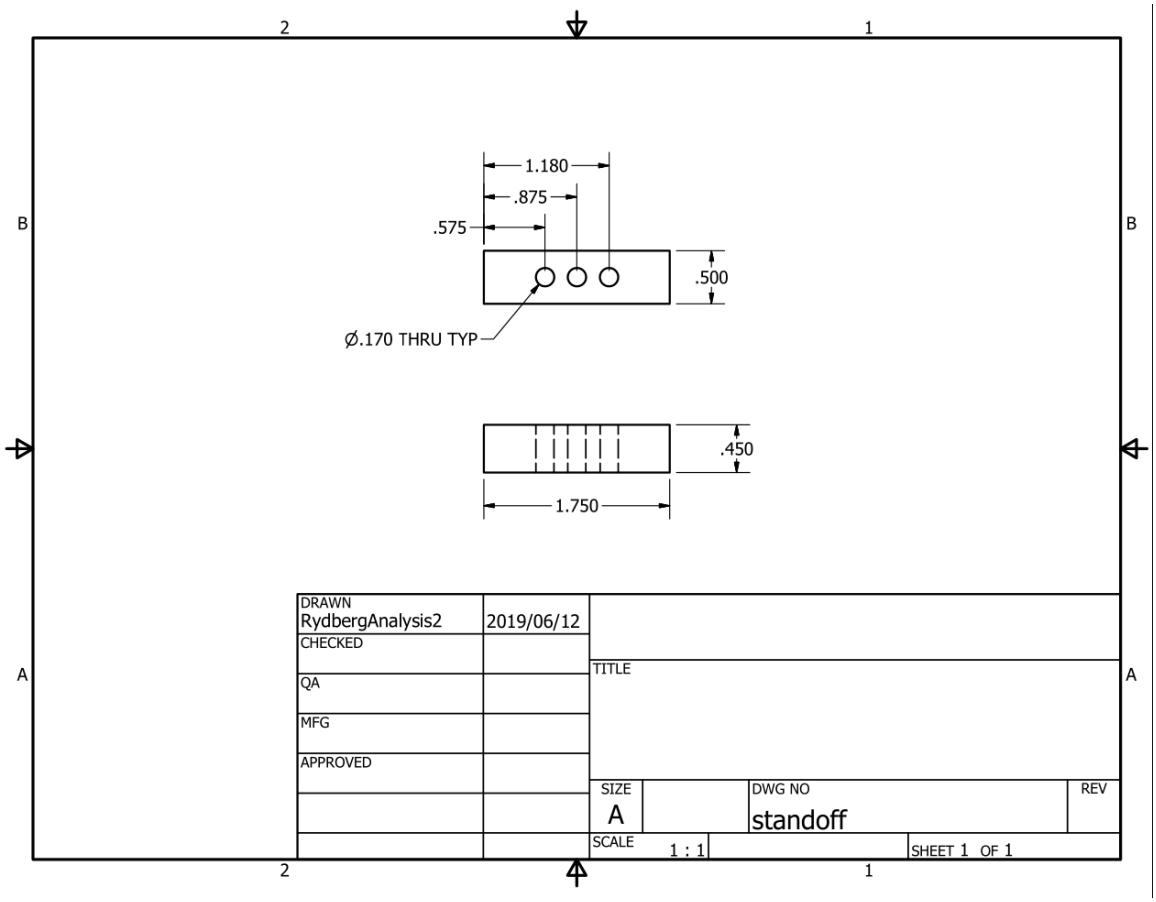

Figure C.4 : Mechanical drawing of the standoffs that support the optical cage for the second sheet trap assembly.

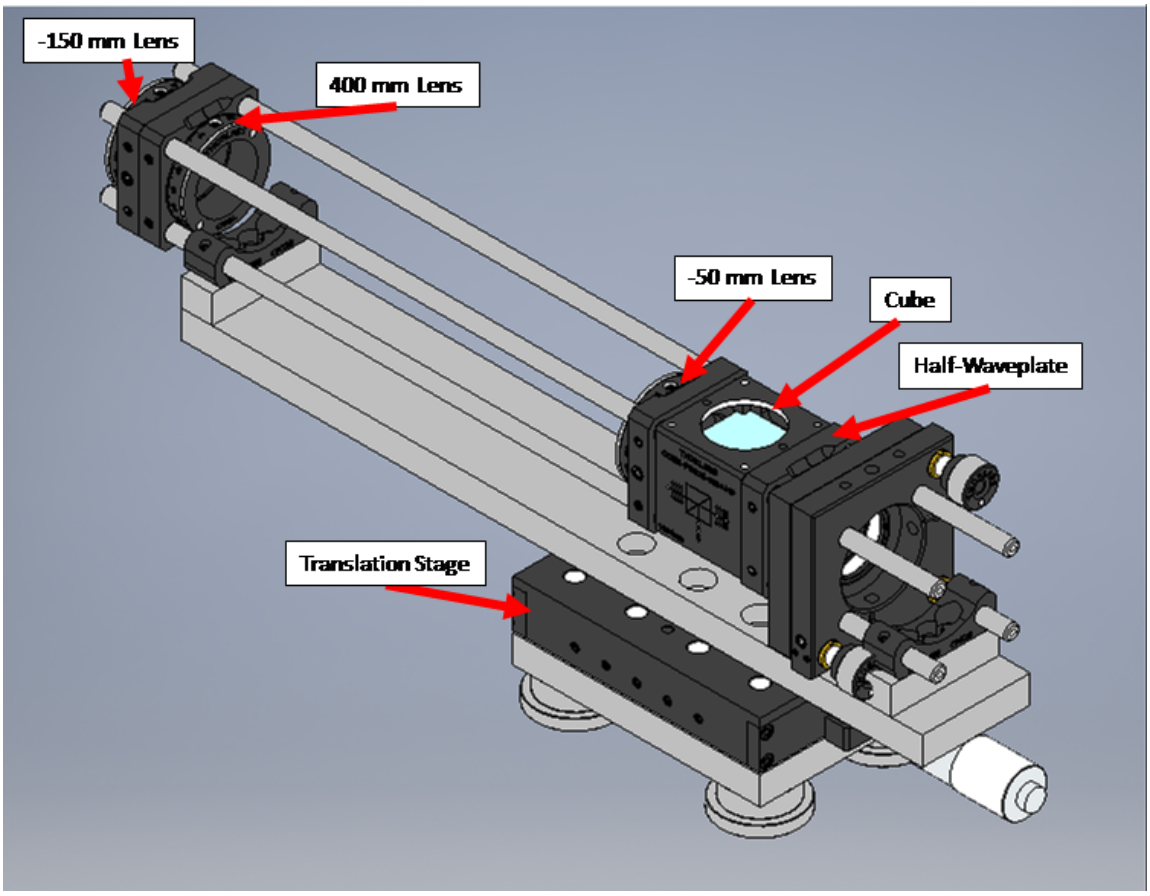

Figure C.5 : A mechanical drawing of the sheet trap optical assembly.

Appendix D

Electric field drawings and datasheets

The following pages are the resources provided about the high voltage switches we use in the ramp generation system.

MOSFET Push/Pull Switch Block Diagram

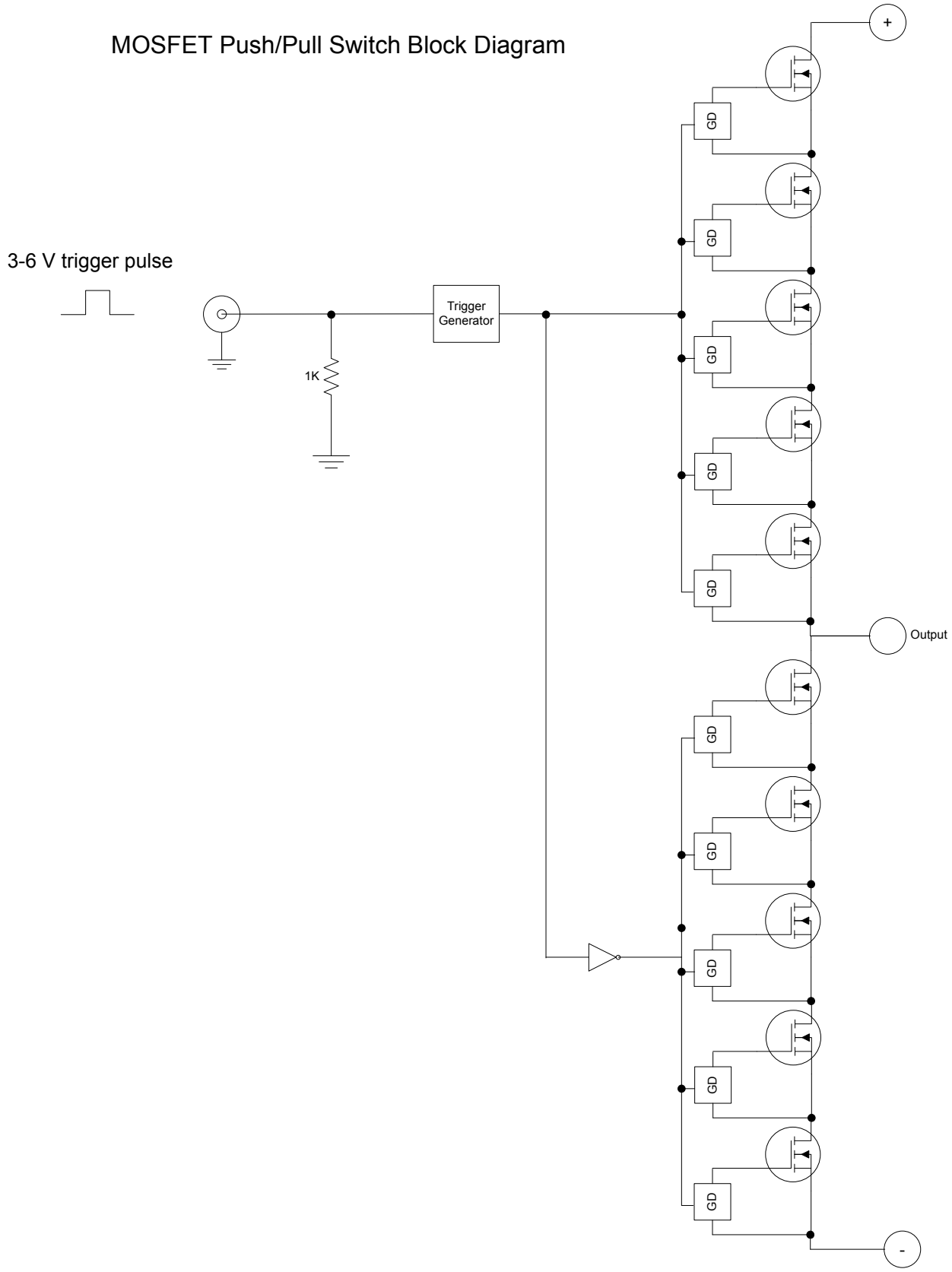

Gate Drivers are Insulated to 15kV

Willamette High Voltage Salem, OR 503-884-7047 www.HVSwitch.com

Technical Specifications for PHVSW-002V, -005V Push/Pull Configuration switches
created 12/01/2010

			-002V	-005V	Unit
Max Voltage Across Terminals	$V_{i(max)}$	Switch Off One Terminal Grounded Bipolar mode	±2000 ±1000	±5000 ±2500	Volts
Break Down Voltage	V_{bd}	Between one terminal and Output	3000	6000	Volts
Isolation Voltage	V_I	Maximum Voltage (±) from ground	>15000	>15000	Volts
Maximum Peak Current	I_{peak}	See safe operation document	15	15	Amps
Maximum Continuous Current	I_C	@ 25° C	0.79	0.56	Amps
On Resistance	R_O	@ 25° C	8.1	16.2	Ω
Turn on delay time	$t_{d(on)}$		<100	<100	ns
Turn on rise time	$t_{r(on)}$	Temperature, current and voltage dependent	10	10	ns
Turn off delay time	$t_{d(off)}$		<100	<100	ns
Turn off rise time	$t_{r(off)}$	Temperature, current and voltage dependent	10	10	ns
Minimum on Time	$t_{on(min)}$	Shorter on time can result in unpredictable switch behavior	50	50	ns
Maximum on Time	$t_{on(max)}$	Limited by maximum power dissipation	∞	∞	
Turn on jitter	$t_{j(on)}$		<400	<400	ps
Maximum Continuous Switching Frequency	$f_{(max)}$	Limited by maximum power dissipation, High burst frequencies possible. See operation notes.	30	30	kH
Maximum Continuous Power Dissipation	$P_{d(max)}$	Total power dissipation into switch We suggestion temperature monitoring for P_d > 5 Watts	15	15	Watts
Operating Temperature Range	T_O		70	-40	° C
Switch Capacitance	C_s		15.6	7.8	pF
Coupling Capacitance	C_c				pF
Supply Voltage	V_{sup}	±0.25 volts	5	5	Volts
Supply Current	C_{sup}	@ $f_{(max)}$ (preliminary)	0.5	0.5	Amps
Trigger Signal	V_{trig}	74LVC input, 1kΩ pull-down resistor. See operation notes.	3.5		Volts
Fault Signal	V_{fault}	Push-Pull Output, 0.25 Amp max Low = Fault	L = 0.1	H = 4.9	Volts
Dimensions		89 x 64 x 27			mm^3

Figure 4. Safe operating area for TO-220

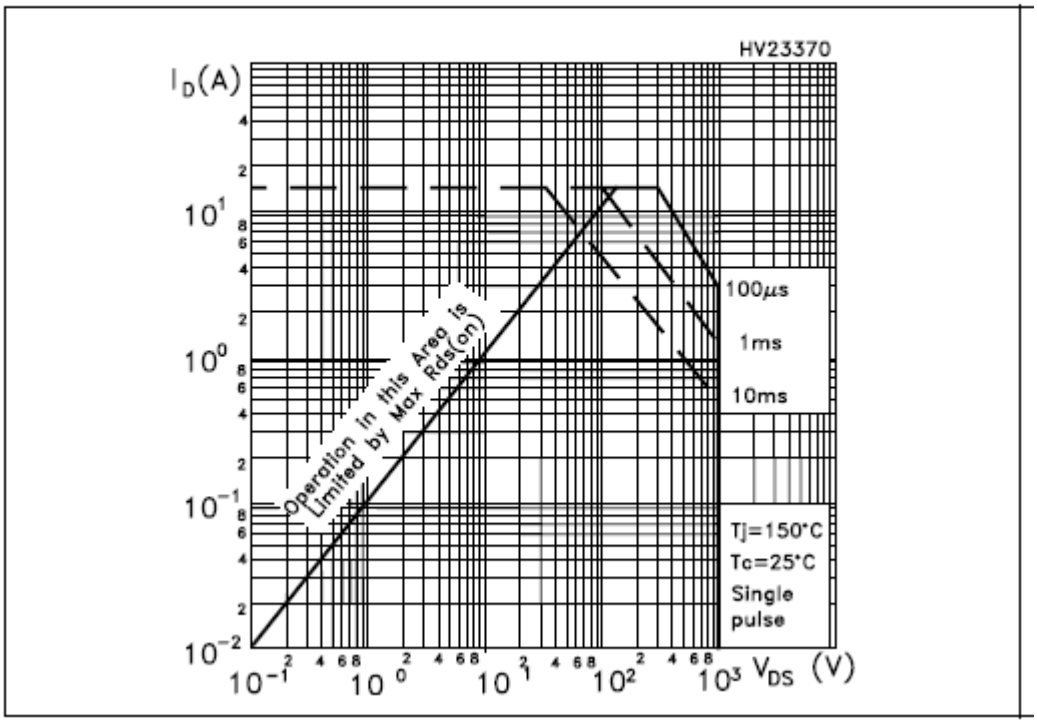

Safe operation for a single MOSFET. Switches are made from a stack of MOSFETS as follows:

MHVSW-002V:	3 MOSFETs
MHVSW-005V:	6 MOSFETs
MHVSW-008V:	9 MOSFETs
MHVSW-011V:	12 MOSFETs

Each MOSFET has an ON resistance of approximately 2.7 Ω (3.7 Ω max).

Here are the drawings that outline the modifications made to the heat sinks for the chassis mounted resistors.

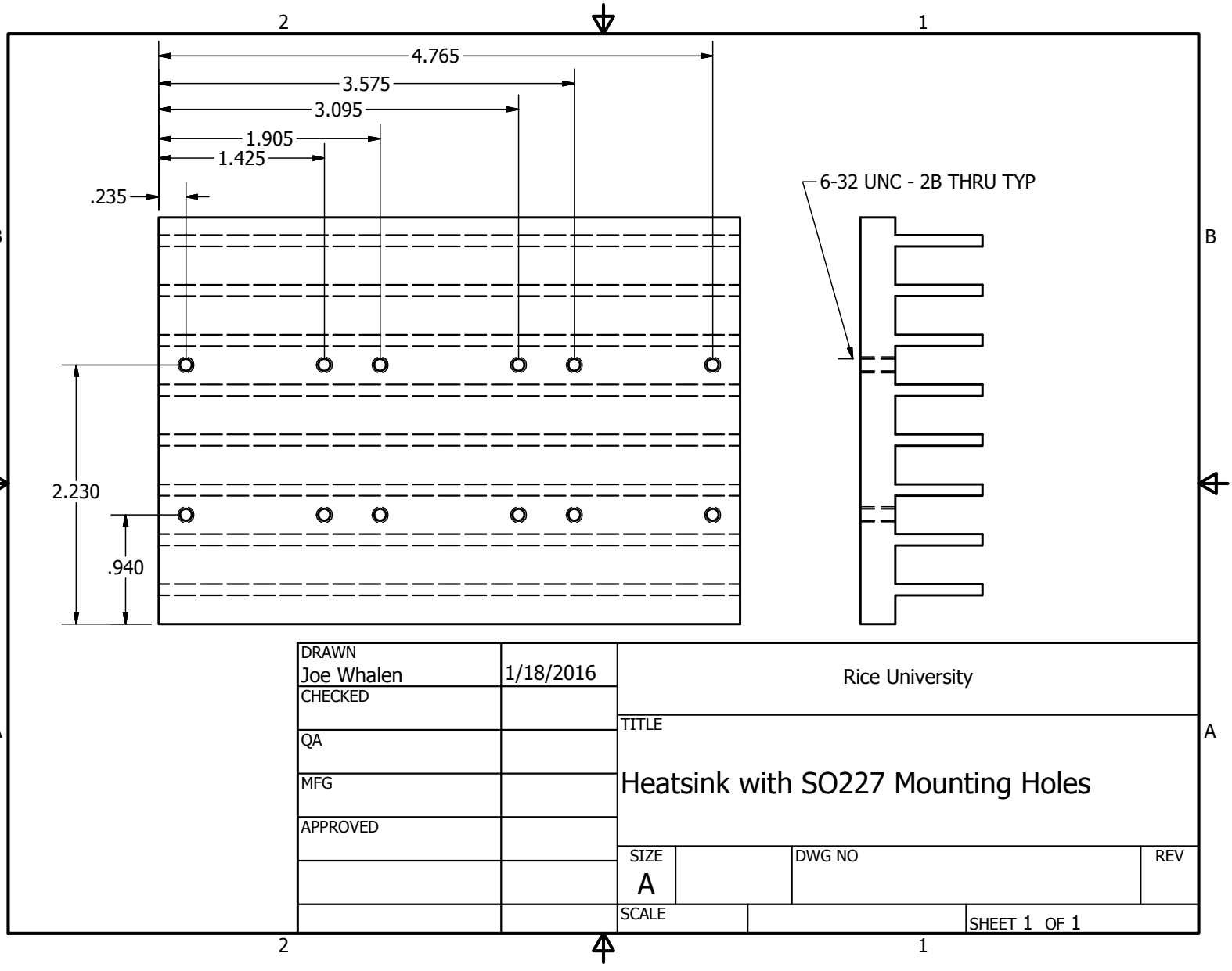

DRAWN Joe Whalen	1/18/2016	Rice University
CHECKED		TITLE: Heatsink with SO227 Mounting Holes
QA		
MFG		
APPROVED		
		SIZE A | DWG NO | REV
		SCALE | SHEET 1 OF 1

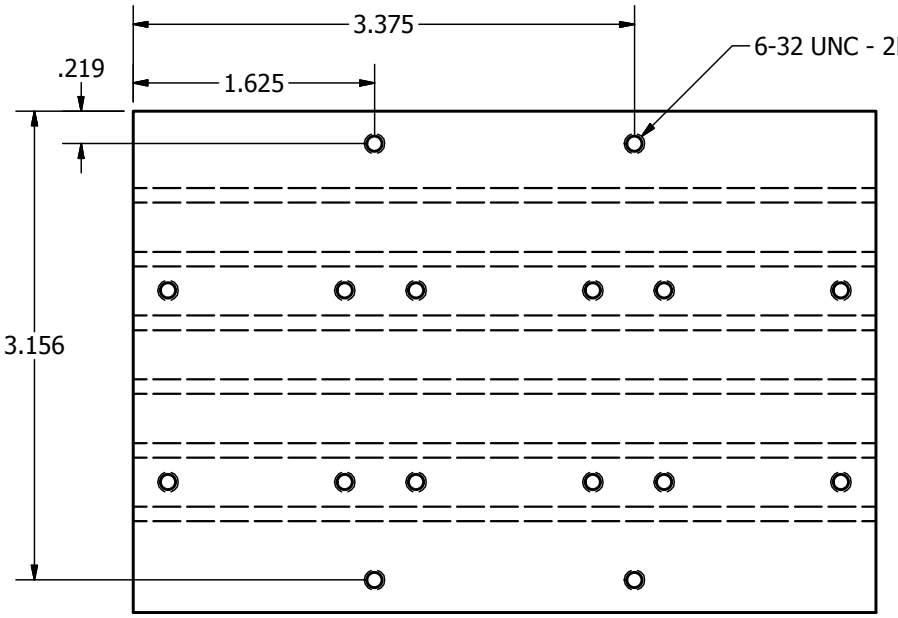

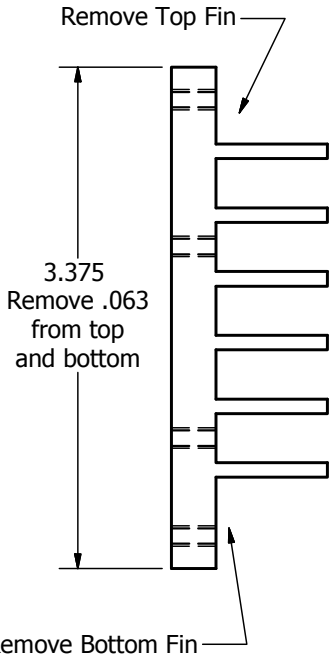

DRAWN jdw9	1/19/2016	
CHECKED		TITLE
QA		
MFG		
APPROVED		
		SIZE A / DWG NO heatsink_with_mounting_holes_trim / REV
		SCALE / SHEET 1 OF 1

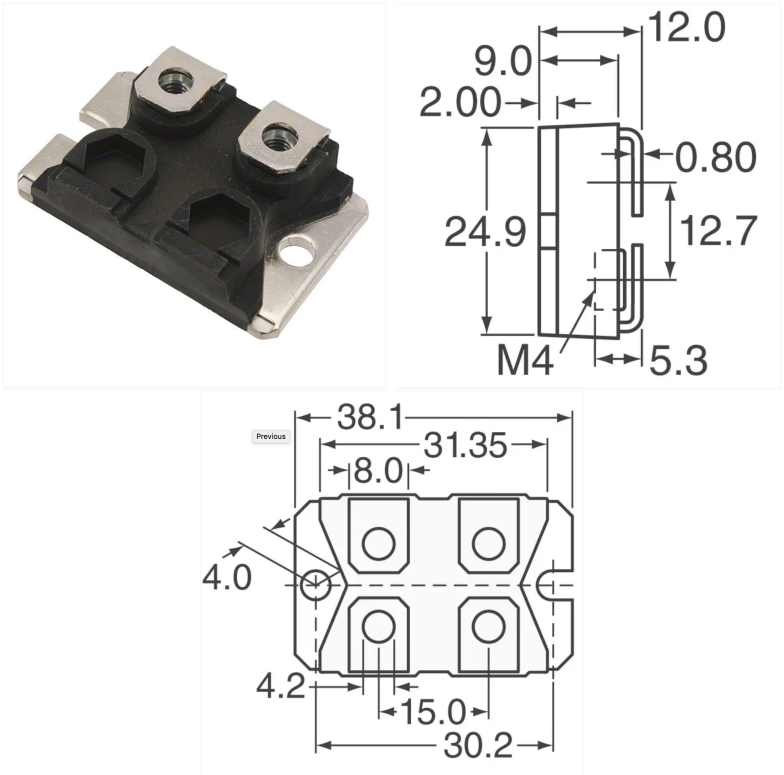

Figure D.1 : An image and the dimensions of the chassis mount resistors used to create the variable resistance for the field ramps.

Bibliography

[1] Martin M. Boyd, *High Precision Spectroscopy of Strontium in an Optical Lattice: Towards a New Standard for Frequency and Time*, Ph.D. thesis, University of Colorado (2007).

[2] Thomas H. Loftus, Tetsuya Ido, Martin M. Boyd, Andrew D. Ludlow, and Jun Ye, Phys. Rev. A **70**, 063413 (2004), arXiv:0407021 [physics] .

[3] Takashi Mukaiyama, Hidetoshi Katori, Tetsuya Ido, Ying Li, and Makoto Kuwata-Gonokami, Phys. Rev. Lett. **90**, 4 (2003).

[4] M. Chalony, A. Kastberg, B. Klappauf, and D. Wilkowski, Phys. Rev. Lett. **107**, 1 (2011).

[5] Tobias Bothwell, Dhruv Kedar, Eric Oelker, John M. Robinson, Sarah L. Bromley, Weston L. Tew, Jun Ye, and Colin J. Kennedy, Metrologia **56**, 065004 (2019).

[6] Rudolf Grimm, Matthias Weidemüller, and Yurii B. Ovchinnikov, in *Adv. At. Mol. Opt. Phys.*, Vol. 42 (2000) pp. 95–170.

[7] Cheng Chin, Rudolf Grimm, Paul Julienne, and Eite Tiesinga, Rev. Mod. Phys. **82**, 1225 (2010), arXiv:0812.1496 .

[8] J. Werner, A. Griesmaier, S. Hensler, J. Stuhler, T. Pfau, A. Simoni, and E. Tiesinga, Phys. Rev. Lett. **94**, 183201 (2005).

[9] T. Maier, H. Kadau, M. Schmitt, M. Wenzel, I. Ferrier-Barbut, T. Pfau, A. Frisch, S. Baier, K. Aikawa, L. Chomaz, M. J. Mark, F. Ferlaino, C. Makrides, E. Tiesinga, A. Petrov, and S. Kotochigova, Phys. Rev. X **5**, 1 (2015), arXiv:1506.05221 .

[10] Simon Stellmer, *Degernate quantum gases of strontium*, Ph.D. thesis (2013).

[11] J A Aman, J C Hill, R Ding, Kaden R A Hazzard, and T C Killian, **053441**, 1 (2018).

[12] C. L. Vaillant, M. P.A. Jones, and R. M. Potvliege, J. Phys. B At. Mol. Opt. Phys. **45** (2012), 10.1088/0953-4075/45/13/135004, arXiv:1203.3736 .

[13] R Ding, J D Whalen, S K Kanungo, T C Killian, F B Dunning, S. Yoshida, and J. Burgdörfer, Phys. Rev. A **98**, 042505 (2018).

[14] F. Camargo, J. D. Whalen, R. Ding, H. R. Sadeghpour, S. Yoshida, J. Burgdörfer, F. B. Dunning, and T. C. Killian, Phys. Rev. A **93**, 1 (2016).

[15] B. J. DeSalvo, J. A. Aman, F. B. Dunning, T. C. Killian, H. R. Sadeghpour, S. Yoshida, and J. Burgdörfer, Phys. Rev. A **92**, 031403 (2015).

[16] E. Amaldi and E. Segrè, Nuovo Cim. **11**, 145 (1934).

[17] E. Amaldi and E. Segrè, Nature **133**, 141 (1934).

[18] Enrico Fermi, Nuovo Cim. **11**, 157 (1934).

[19] Harold J. Metcalf and Peter van der Straten, *Laser Cooling and Trapping*, Graduate Texts in Contemporary Physics (Springer New York, New York, NY, 1999).

[20] Wenlan Chen, Kristin M. Beck, Robert Bücker, Michael Gullans, Mikhail D. Lukin, Haruka Tanji-Suzuki, and Vladan Vuletić, Science (80-.). **341**, 768 (2013).

[21] E. Urban, T. A. Johnson, T. Henage, L. Isenhower, D. D. Yavuz, T. G. Walker, and M. Saffman, Nat. Phys. **5**, 110 (2009), arXiv:0805.0758 .

[22] L. I.R. Gil, R. Mukherjee, E. M. Bridge, M. P.A. Jones, and T. Pohl, Phys. Rev. Lett. **112**, 1 (2014), arXiv:1306.6240 .

[23] Mireille Aymar, Chris H. Greene, and Eliane Luc-Koenig, Rev. Mod. Phys. **68**, 1015 (1996).

[24] C L Vaillant, M P A Jones, and R M Potvliege, J. Phys. B At. Mol. Opt. Phys. **47**, 155001 (2014).

[25] A. Omont, J. Phys. **38**, 1343 (1977).

[26] Vera Bendkowsky, Björn Butscher, Johannes Nipper, James P. Shaffer, Robert Löw, and Tilman Pfau, Nature **458**, 1005 (2009).

[27] D. Booth, S. T. Rittenhouse, J. Yang, H. R. Sadeghpour, and J. P. Shaffer, Science (80-.). **348**, 99 (2015), arXiv:1411.5291 .

[28] Michael Peper and Johannes Deiglmayr, Phys. Rev. Lett. **126**, 13001 (2021), arXiv:2005.12672 .

[29] Thomas Niederprüm, Oliver Thomas, Tanita Eichert, Carsten Lippe, Jesús Pérez-Ríos, Chris H. Greene, and Herwig Ott, Nat. Commun. **7**, 1 (2016), arXiv:1602.08400 .

[30] J. D. Whalen, S. K. Kanungo, Y. Lu, S. Yoshida, J. Burgdörfer, F. B. Dunning, and T. C. Killian, Phys. Rev. A **101**, 1 (2020).

[31] Michael Schlagmüller, Tara Cubel Liebisch, Huan Nguyen, Graham Lochead, Felix Engel, Fabian Böttcher, Karl M. Westphal, Kathrin S. Kleinbach, Robert Löw, Sebastian Hofferberth, Tilman Pfau, Jesús Pérez-Ríos, and Chris H. Greene, Phys. Rev. Lett. **116**, 1 (2016).

[32] Thomas Niederprüm, Oliver Thomas, Tanita Eichert, and Herwig Ott, Phys. Rev. Lett. **117**, 1 (2016).

[33] K. S. Kleinbach, F. Meinert, F. Engel, W. J. Kwon, R. Löw, T. Pfau, and G. Raithel, Phys. Rev. Lett. **118**, 223001 (2017), arXiv:1703.01096 .

[34] R. Côté, "Private Communication," .

[35] F. Camargo, R. Schmidt, J. D. Whalen, R. Ding, G. Woehl, S. Yoshida, J. Burgdörfer, F. B. Dunning, H. R. Sadeghpour, E. Demler, and T. C. Killian, Phys. Rev. Lett. **120**, 83401 (2018), arXiv:1706.03717 .

[36] M. Naraschewski and R. J. Glauber, Phys. Rev. A **59**, 4595 (1999).

[37] E. A. Burt, R. W. Ghrist, C. J. Myatt, M. J. Holland, E. A. Cornell, and C. E. Wieman, Phys. Rev. Lett. **79**, 337 (1997).

[38] Wolfgang Ketterle and Hans-Joachim Miesner, Phys. Rev. A **56**, 3291 (1997).

[39] Martin W. Zwierlein, Zoran Hadzibabic, Subhadeep Gupta, and Wolfgang Ketterle, Phys. Rev. Lett. **91**, 250404 (2003).

[40] Ahmed Omran, Martin Boll, Timon A. Hilker, Katharina Kleinlein, Guillaume Salomon, Immanuel Bloch, and Christian Gross, Phys. Rev. Lett. **115**, 263001 (2015), arXiv:1510.04599 .

[41] Russell A. Hart, Pedro M. Duarte, Tsung Lin Yang, Xinxing Liu, Thereza Paiva, Ehsan Khatami, Richard T. Scalettar, Nandini Trivedi, David A. Huse, and Randall G. Hulet, Nature **519**, 211 (2015), arXiv:1407.5932 .

[42] Paul Niklas Jepsen, Jesse Amato-Grill, Ivana Dimitrova, Wen Wei Ho, Eugene Demler, and Wolfgang Ketterle, Nature **588**, 403 (2020), arXiv:2005.09549 .

[43] Immanuel Bloch, Jean Dalibard, and Wilhelm Zwerger, Rev. Mod. Phys. **80**, 885 (2008), arXiv:0704.3011 .

[44] B. Tolra, K. O'Hara, J. Huckans, W. Phillips, S. Rolston, and J. Porto, Phys. Rev. Lett. **92**, 190401 (2004).

[45] W. S. Bakr, A. Peng, M. E. Tai, R. Ma, J. Simon, J. I. Gillen, S. Fölling, L. Pollet, and M. Greiner, Science (80-.). **329**, 547 (2010), arXiv:1006.0754 .

[46] Anton Mazurenko, Christie S. Chiu, Geoffrey Ji, Maxwell F. Parsons, Márton Kanász-Nagy, Richard Schmidt, Fabian Grusdt, Eugene Demler, Daniel Greif, and Markus Greiner, Nature **545**, 462 (2017).

[47] Reginaldo Napolitano, John Weiner, Carl J. Williams, and Paul S. Julienne, Phys. Rev. Lett. **73**, 1352 (1994).

[48] E. R. I. Abraham, W. I. McAlexander, J. M. Gerton, R. G. Hulet, R. Côté, and A. Dalgarno, Phys. Rev. A **53**, R3713 (1996).

[49] Eite Tiesinga, C.J. Williams, P.S. Julienne, K.M. Jones, P.D. Lett, and W.D. Phillips, J. Res. Natl. Inst. Stand. Technol. **101**, 505 (1996).

[50] C. Boisseau, E. Audouard, J. Vigué, and P. S. Julienne, Phys. Rev. A **62**, 052705 (2000).

[51] Kevin M. Jones, Eite Tiesinga, Paul D. Lett, and Paul S. Julienne, Rev. Mod. Phys. **78**, 483 (2006).

[52] J. J. Sakurai and Jim Napolitano, *Modern Quantum Mechanics* (Cambridge University Press, 1985).

[53] F. Camargo, *Rydberg molecules and polarons in ultracold strontium gases*, Ph.D. thesis, Rice University (2017).

[54] Roger Ding, *Spectroscopy of* ^{87}*Sr Rydberg Atoms and Molecules*, Ph.D. thesis, Rice University (2019).

[55] Alexandre Cooper, Jacob P. Covey, Ivaylo S. Madjarov, Sergey G. Porsev, Marianna S. Safronova, and Manuel Endres, Phys. Rev. X **8**, 41055 (2018).

[56] S. B. Nagel, C. E. Simien, S. Laha, P. Gupta, V. S. Ashoka, and T. C. Killian, Phys. Rev. A **67**, 011401 (2003).

[57] Fachao Hu, Ingo Nosske, Luc Couturier, Canzhu Tan, Chang Qiao, Peng Chen, Y. H. Jiang, Bing Zhu, and Matthias Weidemüller, Phys. Rev. A **99**, 4 (2019), arXiv:1812.01258 .

[58] Roger Ding, *Narrow Line Cooling of* ^{84}*Sr*, Master's thesis, Rice University (2016).

[59] K. M. O'Hara, M. E. Gehm, S. R. Granade, and J. E. Thomas, Phys. Rev. A - At. Mol. Opt. Phys. **64**, 4 (2001).

[60] J E Sansonetti and G Nave, J. Phys. Chem. Ref. Data **39**, 033103 (2010).

[61] S. Subhankar, A. Restelli, Y. Wang, S. L. Rolston, and J. V. Porto, Rev. Sci. Instrum. **90** (2019), 10.1063/1.5067266, arXiv:1810.07256 .

[62] B. G. Lindsay, K. A. Smith, and F. B. Dunning, Rev. Sci. Instrum. **62**, 1656 (1991).

[63] Thomas F. Gallagher, *Rydberg Atoms* (Cambridge University Press, 1994).

[64] Hans A. Bethe and Edwin E. Salpeter, *Quantum Mechanics of One- and Two-Electron Atoms* (Springer US, Boston, MA, 1977).

[65] S. K. Kanungo, J. D. Whalen, Y. Lu, T. C. Killian, F. B. Dunning, S. Yoshida, and J. Burgdörfer, Phys. Rev. A **102**, 063317 (2020).

[66] S. K. Kanungo, J. D. Whalen, Y. Lu, M. Yuan, S. Dasgupta, F. B. Dunning, K. R. A. Hazzard, and T. C. Killian, arXiv (2021), arXiv:2101.02871 .

[67] Simon Stellmer, Rudolf Grimm, and Florian Schreck, Phys. Rev. A - At. Mol. Opt. Phys. **84**, 1 (2011), arXiv:1108.2807 .

[68] R. Ding, S. K. Kanungo, J. D. Whalen, T. C. Killian, F. B. Dunning, S. Yoshida, and J. Burgdörfer, J. Phys. B At. Mol. Opt. Phys. **53**, 014002 (2020).

[69] Andrew N. Vavreck and William Thompson, Q. Appl. Math. **42**, 321 (1984).

[70] J. D. Whalen, S. K. Kanungo, R. Ding, M. Wagner, R. Schmidt, H. R. Sadeghpour, S. Yoshida, J. Burgdörfer, F. B. Dunning, and T. C. Killian, Phys. Rev. A **100**, 011402 (2019).

[71] Toshiya Kinoshita, Trevor Wenger, and David S. Weiss, Science (80-.). **305**, 1125 (2004).

[72] Thorsten Köhler, Krzysztof Góral, and Paul S. Julienne, Rev. Mod. Phys. **78**, 1311 (2006), arXiv:0601420 [cond-mat] .

[73] Ehud Altman, Eugene Demler, and Mikhail D. Lukin, Phys. Rev. A **70**, 013603 (2004), arXiv:0306226 [cond-mat] .

[74] Stefano Giorgini, Lev P. Pitaevskii, and Sandro Stringari, Rev. Mod. Phys. **80**, 1215 (2008).

[75] Chris H. Greene, A. S. Dickinson, and H. R. Sadeghpour, Phys. Rev. Lett. **85**, 2458 (2000).

[76] M. Schellekens, R. Hoppeler, A. Perrin, J. Viana Gomes, D. Boiron, A. Aspect, and C. I. Westbrook, Science (80-.). **310**, 648 (2005).

[77] T. Jeltes, J. M. McNamara, W. Hogervorst, W. Vassen, V. Krachmalnicoff, M. Schellekens, A. Perrin, H. Chang, D. Boiron, A. Aspect, and C. I. Westbrook, Nature **445**, 402 (2007).

[78] Masami Yasuda and Fujio Shimizu, Phys. Rev. Lett. **77**, 3090 (1996).

[79] T. Rom, Th Best, D. Van Oosten, U. Schneider, S. Fölling, B. Paredes, and I. Bloch, Nature **444**, 733 (2006).

[80] T. Manthey, T. Niederprüm, O. Thomas, and H. Ott, New J. Phys. **17**, 103024 (2015).

[81] C. Bahrim, U. Thumm, and I. I. Fabrikant, J. Phys. B At. Mol. Opt. Phys. **34** (2001), 10.1088/0953-4075/34/6/107.

[82] Matthew T. Eiles, Phys. Rev. A **98**, 042706 (2018).

[83] J. D. Whalen, R. Ding, S. K. Kanungo, T. C. Killian, S. Yoshida, J. Burgdörfer, and F. B. Dunning, Mol. Phys. **117**, 3088 (2019).

[84] Simon Stellmer and Florian Schreck, Phys. Rev. A - At. Mol. Opt. Phys. **90**, 1 (2014).

[85] David S. Dean, Pierre Le Doussal, Satya N. Majumdar, and Grégory Schehr, Phys. Rev. A **97**, 1 (2018).

[86] J. D. Whalen, F. Camargo, R. Ding, T. C. Killian, F. B. Dunning, J. Pérez-Ríos, S. Yoshida, and J. Burgdörfer, Phys. Rev. A **96**, 1 (2017).

[87] Michael Schlagmüller, Tara Cubel Liebisch, Felix Engel, Kathrin S. Kleinbach, Fabian Böttcher, Udo Hermann, Karl M. Westphal, Anita Gaj, Robert Löw, Sebastian Hofferberth, Tilman Pfau, Jesús Pérez-Ríos, and Chris H. Greene, Phys. Rev. X **6**, 031020 (2016), arXiv:1605.04883 .

[88] T. Schmid, C. Veit, N. Zuber, R. Löw, T. Pfau, M. Tarana, and M. Tomza, Phys. Rev. Lett. **120**, 153401 (2018), arXiv:1709.10488 .

[89] A. Stein, H. Knöckel, and E. Tiemann, Phys. Rev. A **78**, 042508 (2008), arXiv:0807.4664 .

[90] Y. N. Martinez de Escobar, P. G. Mickelson, P. Pellegrini, S. B. Nagel, A. Traverso, M. Yan, R. Côté, and T. C. Killian, Phys. Rev. A **78**, 062708 (2008).

[91] A. Stein, H. Knöckel, and E. Tiemann, Eur. Phys. J. D **57**, 171 (2010), arXiv:1001.2741 .

[92] Philip M. Morse and Herman Feshbach, *Methods of theoretical physics* (McGraw-Hill, New York, NY, 1953).

[93] Araceli Venegas-Gomez, Johannes Schachenmayer, Anton S. Buyskikh, Wolfgang Ketterle, Maria Luisa Chiofalo, and Andrew J. Daley, arXiv , 1 (2020), arXiv:2003.10905 .

[94] F. Scazza, G. Valtolina, A. Amico, P. E. S. Tavares, M. Inguscio, W. Ketterle, G. Roati, and M. Zaccanti, Phys. Rev. A **101** (2019), 10.1103/PhysRevA.101.013603, arXiv:1910.14279 .

[95] Shina Tan, Ann. Phys. (N. Y). **323**, 2952 (2008), arXiv:0505200 [cond-mat] .

[96] Félix Werner and Yvan Castin, Phys. Rev. A **86**, 053633 (2012), arXiv:1210.1784 .

[97] John Sous, H. R. Sadeghpour, T. C. Killian, Eugene Demler, and Richard Schmidt, Phys. Rev. Res. **2**, 023021 (2020), arXiv:1907.07685 .